Single Impurity Anderson Model and Dynamical Mean Field Theory

A Functional Renormalization Group Study

Von der Fakultät für Mathematik, Informatik und Naturwissenschaften der RWTH Aachen University zur Erlangung des akademischen Grades eines Doktors der Naturwissenschaften genehmigte Dissertation

vorgelegt von
Michael Wolfgang Kinza
aus
Düsseldorf

Berichter: Universitätsprofessor Dr. Carsten Honerkamp
Assistant Professor Dr. Alessandro Toschi

Tag der mündlichen Prüfung: 17. Dezember 2013

Diese Dissertation ist auf den Internetseiten der Hochschulbibliothek online verfügbar.

Abstract

An essential role for the description of correlated quantum many-particle systems is played by impurity problems. These consist of a small number of localized orbitals, where the electrons are subject to a Coulomb-interaction, coupled to noninteracting bath degrees of freedom. Impurity models are used for the description of magnetic impurities in metals, of quantum points in nanostructures, and in the context of the dynamical mean field theory (DMFT). For their solution a large number of numerical methods exists. We mention here quantum Monte Carlo methods, the numerical renormalization group, or the exact diagonalization method.

In this thesis we introduce a new approach to impurity problems, which is based on the functional renormalization group (fRG). In contrast to the methods mentioned above this approach is only approximative, but it can be applied with comparatively lower numerical effort. The aim of this thesis is to examine the advantages and limits of this method. An important role in this connection is played by the single impurity Anderson model, which is already understood very well with other methods and is seen as a prototype for models with strong local correlations. The spin fluctuations of this model are governed by the so-called Kondo energy scale and a central question of this thesis is whether this scale can be reproduced with our approach.

We begin with a short introduction to the Green's function formalism for correlated quantum many particle systems. Then the fRG flow equations for the one-particle irreducible vertex functions are deduced, and several approximation schemes are discussed. In connection with this, we give a short summary of renormalization group methods in the context of quantum impurity problems.

In chapter 4 we introduce the fRG scheme used in this thesis. At first the Anderson model is mapped to a semi-infinite chain, in which the interacting orbital is given by the first site of this chain. The system is then subdivided into two parts. The first part, which is called "core", consists of the interacting orbital and the first L bath sites. The remaining bath sites form the second part. At the beginning both parts are decoupled from each other such that the core can be solved exactly. Starting with this exact solution the coupling between the core and the remaining bath sites is switched on slowly in a renormalization group flow. This way it is possible to calculate the one-particle and two-particle correlation functions on the correlated site. We call this flow scheme "hybridization flow". The flow equations are formulated in an effective theory on the first bath site outside the core, which turnes out to be advantageous compared to other implementations of the hybridization flow.

In chapter 5 this hybridization flow method is applied to the single impurity Anderson model with semi-elliptic bath density of states. We discuss the differences which arise for different core-sizes ($L = 0, 1, 2, 3$) and for different truncations of the renormalization group flow equations. In the cases $L = 0$ and $L = 2$ the local Fermi liquid properties of

the Anderson model and particularly the associated Kondo scale can not be reproduced in both approximation schemes. For the core sizes $L = 1$ and $L = 3$ the ground state of the core is already a spin singlet state in the beginning of the flow and the Fermi liquid properties are succesfully reproduced. The Kondo energy scale, which determines the width of the central quasi-particle peak and the size of the local spin-susceptibility, is however not accurately resolved. This is partly due to the finite temperature used in our implementation such that for larger interaction strength the temperature is above the Kondo energy scale.

The application of the hybridization flow method to quantum impurity problems in the context of the dynamical mean field theory is discussed in chapter 6. In this approach lattice models with a local interaction, like the Hubbard model, are mapped to an effective impurity problem for a single lattice site embedded in a dynamical mean field representing the influence of the other electrons. This scheme is exact in infinitely many dimensions and a nonperturbative approximation method for finite-dimensional systems. In particular the Mott metal-insulator transition in the Hubbard model is succesfully described by this method. One class of quantities, which is easily accessible from the hybridization flow scheme, is given by the local two-particle correlation functions. These play an essential role in non-local extensions of the DMFT. Therefore we mainly focus on these quantities. At first we apply our flow scheme to the Hubbard model on the Bethe lattice in infinite dimensions and calculate the local one-particle irreducible vertex functions in the insulating and the metallic phase in good agreement with previous calculations, which use the exact diagonalization method as impurity solver. After this we extend our flow scheme to a two-site cluster DMFT method, which includes short-range antiferromagnetic correlations and calculate again the local and non-local vertex functions for the two-dimensional Hubbard model. We compare these to the results of the single-site DMFT.

Zusammenfassung

Bei der Beschreibung korrelierter Quanten-Vielteilchensysteme spielen Störstellenprobleme eine wesentliche Rolle. In diesen sind wenige lokalisierte Orbitale, auf denen die Elektronen einer Coulomb-Wechselwirkung unterliegen, an ein wechselwirkungsfreies elektronisches Bad gekoppelt. Diese Modelle werden beispielsweise für die Beschreibung magnetischer Störstellen in Metallen, von Quantenpunkten in Nanostrukturen oder im Kontext der dynamischen Mean-Field-Theorie (DMFT) eingesetzt. Zur Behandlung von Störstellenproblemen existiert eine große Zahl numerischer Verfahren, beispielsweise Quanten-Monte-Carlo Methoden, die numerische Renormierungsgruppe oder die exakte Diagonalisierungsmethode.
In dieser Arbeit wird ein neuer Ansatz zur Beschreibung von Störstellenproblemen eingeführt, der auf der funktionalen Renormierungsgruppe (fRG) beruht. Im Unterschied zu den oben genannten Verfahren ist dieser Ansatz approximativ, seine Anwendung ist dafür mit geringerem numerischem Aufwand verbunden. Das Ziel dieser Arbeit ist, die Vorteile und Grenzen dieses Verfahrens zu untersuchen. Hierbei spielt das Anderson-Modell für eine einzelne Störstelle eine wesentliche Rolle, da es bereits mit anderen Methoden sehr gut verstanden ist und als Prototyp eines Modells für starke lokale Korrelationen angesehen wird. Die Spin-Fluktuationen dieses Modells sind durch die sogenannte Kondo-Energieskala bestimmt und eine zentrale Fragestellung dieser Arbeit ist, ob diese Skala durch unseren Ansatz reproduziert werden kann.
Die Arbeit beginnt mit einer kurzen Einführung in den Formalismus Greenscher Funktionen zur Beschreibung korrelierter Quanten-Vielteilchensysteme. Daran anschließend leiten wir die fRG-Flussgleichungen für die Einteilchen-Irreduziblen Vertex-Funktionen her und diskutieren verschiedene Approximationsverfahren dieser Gleichungen. In diesem Zusammenhang geben wir einen kurzen Überblick über die Verwendung von Renormierungsgruppenmethoden im Kontext von Störstellenproblemen.
In Kapitel 4 führen wir das in dieser Arbeit verwendete fRG-Schema ein. Hierbei wird das Anderson-Modell zunächst auf eine semi-unendliche Kette abgebildet, wobei das wechselwirkende Orbital den ersten Platz dieser Kette einnimmt. Das System wird dann in zwei Bereiche unterteilt. Der erste Bereich, der sogenannte „core“, besteht hierbei aus dem wechselwirkenden Orbital und den ersten L Badplätzen. Die verbleibenden Badplätze bilden den zweiten Bereich. Zu Beginn sind beide Bereiche voneinander entkoppelt, so dass der core exakt gelöst werden kann. Ausgehend von dieser exakten Lösung wird dann die Kopplung zwischen dem core und den verbleibenden Badplätzen im Renormierungsgruppenfluss langsam eingeschaltet. Auf diese Weise ist es möglich die Einteilchen- und Zweiteilchen-Korrelationsfunktionen auf dem korrelierten Platz zu berechnen. Dieses Fluss-Schema bezeichnen wir im Folgenden als „Hybridisierungsfluss“. Die Flussgleichungen sind in einer effektiven Theorie auf dem ersten Badplatz außerhalb des cores formuliert, was sich als vorteilhaft gegenüber anderen Implementierungen des Hybridisierungsflusses erweist.

In Kapitel 5 wird dieses Hybridisierungsfluss-Verfahren auf das Anderson-Modell für eine einzelne Störstelle mit semi-elliptischer Bad-Zustandsdichte angewendet. Hierbei diskutieren wir die Unterschiede, die sich bei verschiedener Größe des cores ($L = 0, 1, 2, 3$) und in den unterschiedlichen Approximationsverfahren der fRG-Flussgleichungen ergeben. In den Fällen $L = 0$ und $L = 2$ gelingt es in beiden Approximationsschemata nicht die lokalen Fermi-Flüssigkeitseigenschaften des Anderson-Modells und insbesondere die damit assoziierte Kondo-Skala zu reproduzieren. Für die core-Größen $L = 1$ und $L = 3$, bei denen sich das System bereits zu Beginn des Flusses in einem Spin-Singlet Grundzustand befindet, kann das Fermi-Flüssigkeitsverhalten reproduziert werden. Die Kondo-Energieskala, welche die Breite des zentralen Quasiteilchenpeaks und auch die Größe der lokalen Spin-Suszeptibilität bestimmt, kann allerdings nicht akurat aufgelöst werden. Dies ist zum Teil darauf zurückzuführen, dass die Methode bei endlichen Temperaturen implementiert ist, welche für große Wechselwirkungsstärken höher als die entsprechende Kondo-Energieskala liegen.

Die Anwendung der Hybridisierungsfluss-Methode zur Lösung des Störstellenproblems in der dynamischen Mean-Field-Theorie wird in Kapitel 6 diskutiert. In dieser Theorie werden Gitter-Modelle mit lokaler Wechselwirkung, wie beispielsweise das Hubbard-Modell, auf ein effektives Störstellenproblem abgebildet. Dieses beschreibt einen einzelnen Gitterplatz, welcher in ein dynamisches mittleres Feld eingebettet ist, das den Einfluss der übrigen Elektronen repräsentiert. Dieses Schema ist in unendlich vielen Dimensionen exakt und stellt eine nichtperturbative Näherungsmethode für endlich-dimensionale Systeme dar. Insbesondere der Mott Metall-Isolator Übergang im Hubbard-Modell kann mit dieser Methode verstanden werden. Die Anwendung des Hybridisierungsfluss-Schemas ermöglicht die Berechnung von Zwei-Teilchen-Korrelationsfunktionen mit geringerem numerischem Aufwand als bei anderen Verfahren, so dass wir uns auf diesen Aspekt schwerpunktmäßig konzentriert haben. Diese Korrelationsfunktionen spielen eine wesentliche Rolle für nichtlokale Erweiterungen der DMFT. Zunächst wenden wir unser Fluss-Schema auf das Hubbard-Modell auf dem unendlichdimensionalen Bethe-Gitter an und berechnen die lokalen Einteilchen-Irreduziblen Vertex-Funktionen in der isolierenden und in der metallischen Phase in guter Übereinstimmung mit bisherigen Berechnungen, bei denen das Störstellenproblem mit Hilfe der exakten Diagonalisierungsmethode gelöst wurde. Hiernach erweitern wir unser Fluss-Schema zu einem Zwei-Platz Cluster-DMFT Verfahren, bei dem kurzreichweitige antiferromagnetische Korrelationen mitberücksichtigt werden und berechnen die lokalen und nichtlokalen Vertex-Funktionen für das zweidimensionale Hubbard-Modell. Diese vergleichen wir mit den Ergebnissen aus der Ein-Platz DMFT.

List of Publications

A large part of this thesis is already published in the following journal articles.
Parts of chapter 4 and 5 can be found in

- M. Kinza, J. Ortloff, J. Bauer, and C. Honerkamp. Alternative functional renormalization group approach to the single impurity Anderson model. *Phys. Rev. B*, 87:035111, Jan 2013

Parts of chapter 6 are presented in

- Michael Kinza and Carsten Honerkamp. Two-particle correlations in a functional renormalization group scheme using a dynamical mean-field theory approach. *Phys. Rev. B*, 88:195136, Nov 2013

The introduction (chapter 1) and the summary (chapter 7) of this thesis resort to sections of both publications.

Another publication, which partially bases on work done during my doctoral studies, but is, however, not part of this thesis, can be found in

- M. Kinza, J. Ortloff, and C. Honerkamp. Effective low-energy Hamiltonians for interacting nanostructures. *Phys. Rev. B*, 82:155430, Oct 2010

Acknowledgements

An dieser Stelle möchte ich mich bei allen bedanken, die zum Gelingen dieser Arbeit beigetragen und mich während meiner Promotion unterstützt haben.
An erster Stelle danke ich Carsten Honerkamp, dass ich bei ihm über dieses interessante Thema promovieren durfte. Diskussionen mit ihm waren immer sehr lehrreich und haben mein physikalisches Weltbild bereichert. Durch seine guten Ideen und Ratschläge hat er wesentlich zum Erfolg dieser Arbeit beigetragen.
Alessandro Toschi danke ich für die Übernahme des Koreferates. Ihm, Sabine Andergassen und Ciro Taranto danke ich ausserdem für die Einladung nach Wien. Die zahlreichen Diskussionen, die wir an der dortigen Universität und an der TU geführt haben waren sehr bereichernd. Ciro danke ich für die DMFT-Daten zum Vertex.
Johannes Bauer danke ich für für lehrreichen Diskussionen zum Anderson Impurity model und für die Bereitstellung seiner NRG-Daten für Kapitel 5 dieser Arbeit.
Außerdem danke ich Jutta Ortloff, David Joerg und Manuel Schmidt, die mit wesentlichen Anregungen und Ideen zu dieser Arbeit beigetragen haben.
Des weiteren danke ich den Mitgliedern des Instituts für Theoretische Festkörperphysik für die angenehme Arbeitsathmosphäre und für zahlreiche Diskussionen über politische, philosophische und (auch) physikalische Themen, die mich menschlich bereichert haben. Unsere Kaffeerunde wird mir ewig unvergesslich bleiben! Dank an Stefan Uebelacker, Michael Scherer, Stefan Maier, Guido Klingschat, Julian Lichtenstein, David Sánchez de la Peña, Michael Golor, Maximilian Lohoefer, Laura Classen, Cornelie Koop und Stefan Wessel.
Zuletzt möchte ich mich bei meinen Freunden und meiner Familie bedanken, die mich in den letzten Jahren auf vielen Ebenen unterstützt haben.

Contents

Chapter 1

Introduction

Since the development of quantum mechanics in the first half of the twentieth century we know the underlying laws to which all phenomena of condensed matter physics and chemistry can be reduced to. Even though this was a great success for the reductionist viewpoint, it turned out that physical systems consisting of many interacting components, although their interaction can be described by very simple laws, show new and unexpected many body phenomena, which are not visible on the level of the fundamental description [And72]. Regarding electrical and magnetic properties of solids these emergent phenomena are often due to strong correlations appearing for example in materials with incomplete d- or f-electron shells. Here interaction effects become important, and the electrons cannot be understood in an effective single-electron picture. Prominent examples for this complex behaviour are the Kondo effect in metals [Hew93], the heavy fermion materials [Ste84], the high-temperature superconductivity in doped cuprates [LNW06], or the Mott Hubbard metal-insulator transition [Mot68, Geb97].

The theoretical description of strongly correlated systems is very challenging and analytical solutions are only available for special models or points in the parameter space. Exact statements can often be obtained by numerical methods, as for example the exact diagonalization method [Lan50], Quantum Monte Carlo (QMC) methods [FMNR01, GML$^+$11], or the Density Matrix Renormalization Group (DMRG) [Sch05]. However, these are still limited to restricted parameter sets due to numerical limitations (like CPU-time or memory) or methodical constraints (like the sign problem in QMC). Therefore, the theoretical challenge remains to develop approximative, but versatile and numerically inexpensive methods, wich can describe a large class of models appearing in this field. In this connection an important role is played by so-called impurity models, in which a small set of interacting orbitals is coupled to noninteracting bath degrees of freedom. Such models appear for example in the description of nanoscale devices, in which quantum dots are coupled to metallic leads [AMS$^+$10], and in the context of the dynamical mean field theory (DMFT) [GKKR96].

As a minimal impurity model we consider in this thesis the single impurity Anderson model (SIAM), where the interacting region consists only of a single impurity site. Through decades of theoretical research since its first proposal in the 1960s [And61] it has been thoroughly investigated. Exact results for thermodynamic properties are available from the Bethe ansatz technique [AFL83, Hew93], and an accurate method to describe static and dynamic properties is Wilson's numerical renormalization group (NRG) [Wil75, BCP08]. Another approach to tackle impurity problems that has been developed is the functional renormalization group (fRG) [Wet93, SH01, MSH$^+$12]. Even though the fundamental equation of this framework is exact most methods based on the fRG are perturbative. Hence, so far it has been difficult to accurately resolve the nonperturbative Kondo physics. However, the transparency and flexibility of the fRG can lead to useful applications in more complex contexts, where, for instance, the NRG is difficult to apply. fRG approaches to the Anderson model come already in some variety, for example, there are variants based on a frequency cutoff [KEM06, HMPS04, KHP$^+$08, AEKM08], on Hubbard-Stratonovich fields representing spin fluctuations [BFCK09, IRB$^+$10, SIK13], and on a flowing level broadening [JPS10]. In addition, nonequilibrium situations are subject to current research [GPM07, JMS07, KPBM10].

Until now all fRG approaches to the SIAM aimed at the development of an efficient and reliable description of nanoelectronic and molecular systems, and fRG was never used as impurity solver in the dynamical mean field theory. This method provides an exact description of the Mott Hubbard metal-insulator transition (MIT) in the infinite-dimensional Hubbard model. In this limit all correlation effects are purely local [MV89], and the Hubbard model can be mapped to an efficient impurity problem coupled to a dynamical Weiss field, which represents the influence of the other lattice electrons. It turned out that this scheme can also be used as controlled approximation scheme for finite-dimensional models, and in combination with ab initio methods (LDA+DMFT) real materials has been successfully described [KSH$^+$06, Hel07]. There have been forceful and physically insightful attempts to include non-local correlations in the DMFT setup, as for example cluster extensions [MJPH05, KSPB01, LK00] and diagrammatic expansions around the local DMFT solution like the dynamical vertex approximation [TKH07, HKT08, RTKH11], the dual fermion method [RKL08, RKLG09], the one-particle irreducible functional approach [RTH$^+$13], or multi-scale methods [SJMD09]. An important ingredient for the diagrammatic methods are the local two-particle correlation functions calculated from DMFT [RVT12], and in order to treat these approaches well, some insights about the frequency structure of these functions will be helpful. Calculating two-particle correlation functions with established impurity solvers like exact diagonalization or quantum Monte Carlo represents a formidable growth of the numerical effort. Hence, it appears worthwile to apply a fRG scheme as a numerically relatively inexpensive impurity solver, since the fRG flow equations explicitly involve the one-particle irreducible vertex function. A better

understanding of the frequency structure of the two-particle vertex is also important for improvements of the fRG scheme applied to lattice models. Here, the frequency dependence of the vertex constitutes a severe complication when it has to be combined with a wavevector or space dependence. For the latter part rather well working approximations have been found [MSH$^+$12, HS09, XWWL12, WLXW13], but on the frequency part, not much is known beyond direct studies with rather large numerical effort [UH12] or boson exchange parametrizations [GS12, KHP$^+$08].

In this thesis we introduce and test a new fRG approach to the SIAM, and show that it can serve as efficient and flexible impurity solver for the dynamical mean field theory. In contrast to the previous approaches, our method starts with the exact solution of a small system of a few sites, which is termed the core. The fRG flow then couples the core adiabatically to a bath of noninteracting fermions in a "hybridization flow". The main motivation for this approach is the following. For practical purposes the hierarchy of the fRG equations for the vertex functions has to be truncated by neglecting the higher-order vertex functions, typically after the two-particle vertex. In the usual context without bare higher-order interactions and in standard perturbation theory these higher-order vertices would appear in higher orders in the bare interactions. Hence, the expectation is that the truncation can only be good at weaker interactions. For a normal many fermion system with a full Fermi surface, in the beginning of the fRG flow, the higher-order terms are suppressed by these higher orders of the bare interactions, while at low scales, near the Fermi surface, additional phase space arguments may limit their impact [SH01]. For strong initial interactions no argument can be given that the impact of these neglected vertex functions is negligible. Another expectation is, however, that these higher-order terms are mainly determined by local physics and by degrees of freedom over a larger energy range in terms of the free Hamiltonian. Therefore one may hope to arrive at a satisfactory description also for stronger interaction by incorporating the higher-order vertices of only a small system and by neglecting their change when the low energy physics is altered during the fRG flow. Hence, in the present approach, we use the exact two-particle vertex and self-energy of a small system as starting point for the hybridization flow. These quantities have built in the effect of all orders in the interaction at least for this small system. Now, performing the truncated fRG flow, the hybridization-induced change of the back effect of the higher-order interactions on the two-particle and ultimately on the self-energy will be missing, but this may still be better than ignoring the higher-order physics completely.

Note that this strategy, which we are testing here for an impurity problem, could also be extended to a lattice problem. One could imagine using the cluster self-energy and two-particle vertices as initial condition for a flow in the band width or hopping amplitude of a lattice dispersion. Similar strategies have already been pursued for bosonic problems [RmcD11a, RmcD11b]. In this context, the present study can be seen as a first step in

the exploration of such a procedure for fermions, with the benefit that in impurity models quantitative benchmarking is possible. Another interesting approach in this context is the recently introduced DMF^{2}RG method [TAB$^+$13], where, starting with the local DMFT solution of the Hubbard model, non-local correlations are included via the functional renormalization group.
The application of RG flow equations usually requires a controlled starting point in the parameter space of the theory, where the vertices are well known. Then one can follow the flow toward a nontrivial physical point of the theory. In our case the flow takes place in the effective theory of the first bath site next to the impurity or correlated core system. Initially, the bath is decoupled, and hence the bath site is noninteracting, providing a well defined starting point. Then, in the RG flow, the coupling to the correlated core is switched on and increased to the desired value. Thereby the bath theory becomes interacting and the spectrum of the bath sites is modified. Employing exact relations between the self-energy and the vertices of the effective theory to the corresponding quantities on the dot site, we can study the signatures of Kondo physics in the Anderson model and, using our scheme as DMFT solver, of Mott physics in the Hubbard model.

1.1 Structure of the thesis

This thesis is organized as follows: In chapter 2 we introduce the Green's function formalism, which is used througout the following chapters. Especially symmetry properties of the two-particle Green's function and the Lehmann representation are discussed in more detail. Chapter 3 contains a brief introduction to the renormalization group in the context of quantum impurity models. The functional renormalization group equations for the generating functional of the one-particle irreducible vertex functions are derived, and different truncation schemes are discussed. In chapter 4 the hybridization flow method for Anderson impurity models is introduced and the hybridization flow equations are derived. The latter are applied to the Anderson model with semi-elliptic density of states in chapter 5, where we concentrate on single-particle properties. We discuss and compare different core sizes and approximations to the hybridization flow equations and investigate if we can reproduce the nonperturbative Kondo scale with this setup. In chapter 6 we show that the hybridization flow method can be used as reliable impurity solver in a DMFT setup. Here we concentrate on two-particle quantities and derive the density and magnetic part of the one-particle irreducible vertex within single-site DMFT for the insulating and the metallic phase. Then we consider a two-site cluster DMFT scheme and again calculate the two-particle vertices. These are compared to the result of the single-site DMFT. In the last chapter 7 we summarize our results and discuss possible ideas for future projects.

Chapter 2

Formalism

For the description of correlated many body systems one needs quantum field theoretical methods, especially the Green's function formalism. These are presented extensively in numerous textbooks on the subject [NO88, AS06], and we refer to these for a more extensive introduction. The reader will find below a summary of the most important properties of n-particle Green's functions and their generating functionals. In particular, symmetry properties and the so-called Lehmann representation are discussed in more detail.

2.1 The partition function as a path integral

We consider a fermionic many particle system, described by the normal-ordered Hamiltonian $\hat{H}$, which contains a free part $\hat{H}_0$ and an interaction part $\hat{V}$.

$$\begin{aligned}\hat{H} &= \hat{H}_0 + \hat{V} \\ &= \sum_{i,j} a_i^\dagger \left(T_{ij} - \mu\delta_{ij}\right) a_j + \frac{1}{4}\sum_{i,j,k,l} a_i^\dagger a_j^\dagger V_{ijkl} a_l a_k \end{aligned} \tag{2.1}$$

The $a_i^{(\dagger)}$ denote fermionic annihilation and creation operators, which are characterized by the multi-index i containing all quantum numbers (e.g. position, spin) of a single-particle basis. The chemical potential μ is included in the free part of the Hamiltonian. The interaction matrix element V_{ijkl} is antisymmetrized, i.e. we have $V_{ijkl} = -V_{jikl} = -V_{ijlk}$. The grand canonical partition function $Z = \mathrm{Tr}\left[\exp\left[-\beta\hat{H}\right]\right]$ can be written as a functional integral over Grassmann fields $\bar{\psi}, \psi$ in the form

$$Z = \int \mathcal{D}[\bar{\psi}, \psi] \exp\left[-S[\bar{\psi}, \psi]\right] \tag{2.2}$$

with the action $S[\bar{\psi}, \psi]$ given by

$$S[\bar{\psi}, \psi] = \int_0^\beta \mathrm{d}\tau \left[\sum_i \bar{\psi}_i(\tau + 0^+)\frac{\mathrm{d}\psi_i(\tau)}{\mathrm{d}\tau} + \mathcal{H}(\bar{\psi}, \psi)\right], \tag{2.3}$$

where $\mathcal{H}$ is related to $\hat{H}$ by the replacement

$$\mathcal{H}(\bar{\psi},\psi) = \hat{H}(a_i^\dagger \to \bar{\psi}_i(\tau+0^+), a_i \to \psi_i(\tau)). \tag{2.4}$$

The Grassmann fields obey the boundary conditions $\psi_i(\beta) = -\psi_i(0)$ and $\bar{\psi}_i(\beta) = -\bar{\psi}_i(0)$. Therefore we can simplify the expression (2.3) by a Fourier transform defined as

$$\psi_i(\tau) = \frac{1}{\beta}\sum_{i\omega_n} \mathrm{e}^{-i\omega_n\tau}\psi_i(i\omega_n), \tag{2.5}$$

$$\bar{\psi}_i(\tau) = \frac{1}{\beta}\sum_{i\omega_n} \mathrm{e}^{i\omega_n\tau}\bar{\psi}_i(i\omega_n). \tag{2.6}$$

The $i\omega_n$ denote fermionic Matsubara frequencies $i\omega_n = i(2n+1)\frac{\pi}{\beta}$. In frequency space the action reads

$$\begin{aligned} S[\bar{\psi},\psi] = &-\frac{1}{\beta}\sum_{i\omega_n}\sum_{i,j}\bar{\psi}_i(i\omega_n)Q_{ij}(i\omega_n)\psi_j(i\omega_n) \\ &+\frac{1}{\beta^3}\sum_{\substack{i\omega_m,i\omega_n \\ i\omega_{m'},i\omega_{n'}}}\sum_{i,j,k,l}\bar{\psi}_i(i\omega_{m'})\bar{\psi}_j(i\omega_{n'})V_{ijkl}\psi_l(i\omega_m)\psi_k(i\omega_n)\delta_{\omega_{m'}+\omega_{n'},\omega_m+\omega_n}, \end{aligned} \tag{2.7}$$

with the matrix Q given by

$$Q_{ij}(i\omega_n) = (i\omega_n+\mu)\delta_{ij} - T_{ij}. \tag{2.8}$$

2.2 Green's functions and generating functionals

The n-particle Green's functions in imaginary time are defined as time ordered [1] expectation values by

$$\begin{aligned} &\mathcal{G}^{(n)}(\alpha_1,\tau_1;...;\alpha_n,\tau_n|\alpha_{1'},\tau_{1'};...;\alpha_{n'}\tau_{n'}) \\ =&(-1)^n\langle T_\tau a_{\alpha_1}(\tau_1)...a_{\alpha_n}(\tau_n)a^\dagger_{\alpha_{n'}}(\tau_{n'})...a^\dagger_{\alpha_{1'}}(\tau_{1'})\rangle \\ =&\frac{(-1)^n}{Z}\mathrm{Tr}\left[\exp\left(-\beta\hat{H}\right)T_\tau a_{\alpha_1}(\tau_1)...a_{\alpha_n}(\tau_n)a^\dagger_{\alpha_{n'}}(\tau_{n'})...a^\dagger_{\alpha_{1'}}(\tau_{1'})\right] \end{aligned} \tag{2.10}$$

with the time dependent Heisenberg operators

$$a_i^{(\dagger)}(\tau) = \exp\left(\tau\hat{H}\right)a_i^{(\dagger)}\exp\left(-\tau\hat{H}\right). \tag{2.11}$$

[1] The time ordering T_τ of a product of fermionic time dependent operators is defined as

$$T_\tau\left[\mathcal{O}_{\alpha_1}(\tau_1)\mathcal{O}_{\alpha_2}(\tau_2)...\mathcal{O}_{\alpha_n}(\tau_n)\right] = (-1)^P\mathcal{O}_{\alpha_{P_1}}(\tau_{P_1})\mathcal{O}_{\alpha_{P_2}}(\tau_{P_2})...\mathcal{O}_{\alpha_{P_n}}(\tau_{P_n}), \tag{2.9}$$

where P is the permutation that orders the times in chronological order with the latest time to the left and creation operators to the left of annihilation operators at equal time.

The Green's functions can be transformed to imaginary Matsubara frequencies by the Fourier transform

$$\begin{aligned}\mathcal{G}^{(n)}(\alpha_1,\tau_1;...;\alpha_n,\tau_n|\alpha_{1'},\tau_{1'};...;\alpha_{n'},\tau_{n'}) =&\frac{1}{\beta^{2n}}\sum_{\substack{i\omega_1,...,i\omega_n\\ i\omega_{1'},...,i\omega_{n'}}} \mathrm{e}^{-\sum_j\left(i\omega_j\tau_j - i\omega_{j'}\tau_{j'}\right)}\\ &\times\mathcal{G}^{(n)}(\alpha_1,i\omega_1;...;\alpha_n,i\omega_n|\alpha_{1'},i\omega_{1'};...;\alpha_{n'},i\omega_{n'}),\end{aligned} \tag{2.12}$$

$$\begin{aligned}\mathcal{G}^{(n)}(\alpha_1,i\omega_1;...;\alpha_n,i\omega_n|\alpha_{1'},i\omega_{1'};...;\alpha_{n'},i\omega_{n'}) =&\int_0^\beta \mathrm{d}\tau_1...\mathrm{d}\tau_n\mathrm{d}\tau_{1'}...\mathrm{d}\tau_{n'}\mathrm{e}^{\sum_j\left(i\omega_j\tau_j - i\omega_{j'}\tau_{j'}\right)}\\ &\times\mathcal{G}^{(n)}(\alpha_1,\tau_1;...;\alpha_n,\tau_n|\alpha_{1'},\tau_{1'};...;\alpha_{n'},\tau_{n'}).\end{aligned} \tag{2.13}$$

Due to the cyclic invariance of the trace, one can eliminate the dependence of the Green's function (2.10) on the last time argument

$$\mathcal{G}^{(n)}(\alpha_1,\tau_1;...;\alpha_n,\tau_n|\alpha_{1'},\tau_{1'};...;\alpha_{n'},\tau_{n'}) = \mathcal{G}^{(n)}(\alpha_1,\tau_1-\tau_{n'};...;\alpha_n,\tau_n-\tau_{n'}|\alpha_{1'},\tau_{1'}-\tau_{n'};...;\alpha_{n'}). \tag{2.14}$$

This results in energy conservation

$$\begin{aligned}\mathcal{G}^{(n)}(\alpha_1,i\omega_1;...;\alpha_n,i\omega_n|\alpha_{1'},i\omega_{1'};...;\alpha_{n'},i\omega_{n'}) =&\beta\delta_{\sum_j(i\omega_j - i\omega_{j'}),0}\\ &\times\mathcal{G}^{(n)}(\alpha_1,i\omega_1;...;\alpha_n,i\omega_n|\alpha_{1'},i\omega_{1'};...;\alpha_{n'})\end{aligned} \tag{2.15}$$

with

$$\begin{aligned}\mathcal{G}^{(n)}(\alpha_1,i\omega_1;...;\alpha_n,i\omega_n|\alpha_{1'},i\omega_{1'};...;\alpha_{n'}) =&\int_0^\beta \mathrm{d}\tau_1...\mathrm{d}\tau_n\mathrm{d}\tau_{1'}...\mathrm{d}\tau_{n-1'}\mathrm{e}^{\sum_{j=1}^n i\omega_j\tau_j}\mathrm{e}^{-\sum_{j=1}^{n-1} i\omega_{j'}\tau_{j'}}\\ &\times\mathcal{G}^{(n)}(\alpha_1,\tau_1;...;\alpha_n,\tau_n|\alpha_{1'},\tau_{1'};...;\alpha_{n'}).\end{aligned} \tag{2.16}$$

In the following, if not stated otherwise, the multi-index α_i stands for either (α_i,τ_i) or $(\alpha_i,i\omega_i)$. Written as a path integral, $\mathcal{G}^{(n)}$ is given by

$$\mathcal{G}^{(n)}(\alpha_1,...,\alpha_n|\alpha_{1'},...,\alpha_{n'}) = \frac{(-1)^n}{Z}\int\mathcal{D}[\bar\psi,\psi]\psi_{\alpha_1}...\psi_{\alpha_n}\bar\psi_{\alpha_{n'}}...\bar\psi_{\alpha_{1'}}\exp\left[-S[\bar\psi,\psi]\right]. \tag{2.17}$$

In this form the Green's functions are obtained from the generating functional

$$\mathcal{Z}\left[\bar\eta,\eta\right] = \frac{1}{Z}\int\mathcal{D}[\bar\psi,\psi]\exp\left[-S[\bar\psi,\psi] - (\bar\psi,\eta) - (\bar\eta,\psi)\right] \tag{2.18}$$

as derivatives with respect to the Grassmann source fields η and $\bar\eta$

$$\mathcal{G}^{(n)}(\alpha_1,...,\alpha_n|\alpha_{1'},...,\alpha_{n'}) = \frac{\delta^n}{\delta\bar\eta_{\alpha_1}...\delta\bar\eta_{\alpha_n}}\frac{\delta^n}{\delta\eta_{\alpha_{n'}}...\delta\eta_{\alpha_{1'}}}\mathcal{Z}\left[\bar\eta,\eta\right]\Big|_{\eta=\bar\eta=0}, \tag{2.19}$$

such that

$$\mathcal{Z}\left[\bar{\eta},\eta\right]=\sum_{n=0}^{\infty}\frac{(-1)^n}{n!^2}\sum_{\substack{\alpha_1,\ldots,\alpha_n\\ \alpha_{1'},\ldots,\alpha_{n'}}}\mathcal{G}^{(n)}\left(\alpha_1,...,\alpha_n|\alpha_{1'},...,\alpha_{n'}\right)\bar{\eta}_{\alpha_1}...\bar{\eta}_{\alpha_n}\eta_{\alpha_{n'}}...\eta_{\alpha_{1'}}. \tag{2.20}$$

In (2.18) we introduced the scalar product

$$\left(\bar{\psi},\phi\right)=\int_0^\beta \mathrm{d}\tau\sum_j\bar{\psi}_j(\tau)\phi_j(\tau)=\frac{1}{\beta}\sum_{i\omega_n}\sum_j\bar{\psi}_j(i\omega_n)\phi_j(i\omega_n). \tag{2.21}$$

In the noninteracting case the functional (2.18) reduces to a Gaussian integral, which can be evaluated exactly,

$$\begin{aligned}\mathcal{Z}_0\left[\bar{\eta},\eta\right]=&\frac{1}{Z_0}\int\mathcal{D}[\bar{\psi},\psi]\exp\left[(\bar{\psi},Q\psi)-(\bar{\psi},\eta)-(\bar{\eta},\psi)\right]\\ =&\exp\left[-\left(\bar{\eta},Q^{-1}\eta\right)\right].\end{aligned} \tag{2.22}$$

From Eq. (2.19) we can derive the noninteracting one-particle Green's function, which turns out to be equal to the inverse of the matrix (2.8),

$$\mathcal{G}_0\left(\alpha_1,\alpha_{1'}\right)=\frac{\delta^2\mathcal{Z}_0\left[\bar{\eta},\eta\right]}{\delta\bar{\eta}_{\alpha_1}\delta\eta_{\alpha_{1'}}}=\frac{\delta^2}{\delta\bar{\eta}_{\alpha_1}\delta\eta_{\alpha_{1'}}}\exp\left[-\left(\bar{\eta},Q^{-1}\eta\right)\right]=\left[Q^{-1}\right]_{\alpha_1,\alpha_{1'}}. \tag{2.23}$$

Similarly, the *connected* Green's functions are generated from the functional

$$\mathcal{W}\left[\bar{\eta},\eta\right]=\ln\left[\mathcal{Z}\left[\bar{\eta},\eta\right]\right] \tag{2.24}$$

as

$$\mathcal{G}^{c,(n)}(\alpha_1,...,\alpha_n|\alpha_{1'},...,\alpha_{n'})=\frac{\delta^n}{\delta\bar{\eta}_{\alpha_1}...\delta\bar{\eta}_{\alpha_n}}\frac{\delta^n}{\delta\eta_{\alpha_{n'}}...\delta\eta_{\alpha_{1'}}}\mathcal{W}\left[\bar{\eta},\eta\right]\Bigg|_{\eta=\bar{\eta}=0}. \tag{2.25}$$

A straightforward calculation yields

$$\mathcal{G}^{c,(1)}(\alpha_1|\alpha_{1'})=\mathcal{G}^{(1)}(\alpha_1|\alpha_{1'}), \tag{2.26}$$

and for $n=2$ one gets

$$\begin{aligned}\mathcal{G}^{c,(2)}(\alpha_1,\alpha_2|\alpha_{1'},\alpha_{2'})=&\mathcal{G}^{(2)}(\alpha_1,\alpha_2|\alpha_{1'},\alpha_{2'})-\mathcal{G}^{(1)}(\alpha_1|\alpha_{1'})\mathcal{G}^{(1)}(\alpha_2|\alpha_{2'})\\ &+\mathcal{G}^{(1)}(\alpha_1|\alpha_{2'})\mathcal{G}^{(1)}(\alpha_2|\alpha_{1'}).\end{aligned} \tag{2.27}$$

Another class of correlation functions, which play a central role in the fRG formalism, are the one-particle irreducible (1PI) vertex functions. They consist of those diagrams that cannot be disconnected by removing a single internal propagator. Their generating functional depends on the Grassmann fields

$$\phi_k(\bar{\eta},\eta)=-\frac{\delta}{\delta\bar{\eta}_k}\mathcal{W}\left[\bar{\eta},\eta\right], \tag{2.28}$$

$$\bar{\phi}_k(\bar{\eta},\eta)=\frac{\delta}{\delta\eta_k}\mathcal{W}\left[\bar{\eta},\eta\right] \tag{2.29}$$

and is defined as the Legendre transform of $\mathcal{W}[\bar{\eta},\eta]$

$$\Gamma\left[\bar{\phi},\phi\right] = -\mathcal{W}[\bar{\eta},\eta] - \left(\bar{\phi},\eta\right) - \left(\bar{\eta},\phi\right) + \left(\bar{\phi},\mathcal{G}_0^{-1}\phi\right). \tag{2.30}$$

The n-particle vertex functions are derivatives with respect to ϕ and $\bar{\phi}$,

$$\gamma^{(n)}(\alpha_1,...,\alpha_n|\alpha_{1'},...,\alpha_{n'}) = \frac{\delta^n}{\delta\bar{\phi}_{\alpha_1}...\delta\bar{\phi}_{\alpha_n}}\frac{\delta^n}{\delta\phi_{\alpha_{n'}}...\delta\phi_{\alpha_{1'}}}\Gamma\left[\bar{\phi},\phi\right]\Big|_{\phi=\bar{\phi}=0}. \tag{2.31}$$

To get relations between the 1PI vertex functions and the connected Green's functions, we derivate Γ with respect to ϕ and $\bar{\phi}$:

$$\frac{\delta}{\delta\phi_k}\Gamma\left[\bar{\phi},\phi\right] = \bar{\eta}_k - \sum_q \bar{\phi}_q\left[\mathcal{G}_0^{-1}\right]_{qk} \tag{2.32}$$

$$\frac{\delta}{\delta\bar{\phi}_k}\Gamma\left[\bar{\phi},\phi\right] = -\eta_k + \sum_q \left[\mathcal{G}_0^{-1}\right]_{kq}\phi_q \tag{2.33}$$

Using these derivatives one can show

$$\begin{pmatrix} \frac{\delta^2\Gamma}{\delta\bar{\phi}\delta\phi} + \mathcal{G}_0^{-1} & \frac{\delta^2\Gamma}{\delta\bar{\phi}\delta\bar{\phi}} \\ \frac{\delta^2\Gamma}{\delta\phi\delta\phi} & \frac{\delta^2\Gamma}{\delta\phi\delta\bar{\phi}} - \left[\mathcal{G}_0^{-1}\right]^T \end{pmatrix}\begin{pmatrix} \frac{\delta^2\mathcal{W}}{\delta\bar{\eta}\delta\eta} & -\frac{\delta^2\mathcal{W}}{\delta\bar{\eta}\delta\bar{\eta}} \\ -\frac{\delta^2\mathcal{W}}{\delta\eta\delta\eta} & \frac{\delta^2\mathcal{W}}{\delta\eta\delta\bar{\eta}} \end{pmatrix} = \mathbf{1}$$

$$\Rightarrow \quad \begin{pmatrix} \frac{\delta^2\mathcal{W}}{\delta\bar{\eta}\delta\eta} & -\frac{\delta^2\mathcal{W}}{\delta\bar{\eta}\delta\bar{\eta}} \\ -\frac{\delta^2\mathcal{W}}{\delta\eta\delta\eta} & \frac{\delta^2\mathcal{W}}{\delta\eta\delta\bar{\eta}} \end{pmatrix} = \begin{pmatrix} \frac{\delta^2\Gamma}{\delta\bar{\phi}\delta\phi} + \mathcal{G}_0^{-1} & \frac{\delta^2\Gamma}{\delta\bar{\phi}\delta\bar{\phi}} \\ \frac{\delta^2\Gamma}{\delta\phi\delta\phi} & \frac{\delta^2\Gamma}{\delta\phi\delta\bar{\phi}} - \left[\mathcal{G}_0^{-1}\right]^T \end{pmatrix}^{-1}. \tag{2.34}$$

If the Hamiltonian (2.1) is U(1) symmetric and no spontaneous symmetry breaking occurs, we have $\frac{\delta^2\mathcal{W}}{\delta\eta\delta\eta}\Big|_{\eta=\bar{\eta}=0} = \frac{\delta^2\mathcal{W}}{\delta\bar{\eta}\delta\bar{\eta}}\Big|_{\eta=\bar{\eta}=0} = 0$ and $\frac{\delta^2\Gamma}{\delta\phi\delta\phi}\Big|_{\phi=\bar{\phi}=0} = \frac{\delta^2\Gamma}{\delta\bar{\phi}\delta\bar{\phi}}\Big|_{\phi=\bar{\phi}=0} = 0$. It follows

$$\mathcal{G}^{c,(1)}(\alpha_1|\alpha_{1'}) = \frac{\delta^2\mathcal{W}[\bar{\eta},\eta]}{\delta\bar{\eta}_{\alpha_1}\delta\eta_{\alpha_{1'}}}\Big|_{\eta=\bar{\eta}=0} = \left[\gamma^{(1)} + \mathcal{G}_0^{-1}\right]^{-1}_{\alpha_1,\alpha_{1'}}.$$

The one-particle vertex function defines the so-called self-energy

$$\Sigma = -\gamma^{(1)} \tag{2.35}$$

and with Eqs. (2.26) and (2.35) one gets the Dyson equation

$$\Sigma = \mathcal{G}_0^{-1} - \left[\mathcal{G}^{(1)}\right]^{-1}. \tag{2.36}$$

The relation between the two-particle 1PI vertex function and the connected two-particle Green's function is given by

$$\gamma^{(2)}(\alpha_1,\alpha_2|\alpha_{1'},\alpha_{2'}) = -\sum_{\substack{\beta_1,\beta_2\\ \beta_{1'}\beta_{2'}}}\left[\mathcal{G}^{(1)}\right]^{-1}_{\alpha_1,\beta_1}\left[\mathcal{G}^{(1)}\right]^{-1}_{\alpha_2,\beta_2}\mathcal{G}^{c,(2)}(\beta_1,\beta_2|\beta_{1'},\beta_{2'})\left[\mathcal{G}^{(1)}\right]^{-1}_{\beta_{1'},\alpha_{1'}}\left[\mathcal{G}^{(1)}\right]^{-1}_{\beta_{2'},\alpha_{2'}}. \tag{2.37}$$

2.3 Symmetries

In this section we discuss the most important symmetry properties of one- and two-particle Green's functions, i.e. the time reversal symmetry, the particle-hole symmetry, and the spin rotation invariance. We will keep the discussion short and refer to textbooks (e.g. [Mes79]) or the detailed discussion in [Saa11] for further details.

2.3.1 Complex conjugation

The complex conjugate of the one- and two-particle Green's functions obey the following relations, which follow from (2.10) and (2.13).

$$\mathcal{G}^{(1)}(\alpha_1, i\omega|\alpha_{1'})^* = \mathcal{G}^{(1)}(\alpha_{1'}, -i\omega|\alpha_1) \tag{2.38}$$

$$\mathcal{G}^{(2)}(\alpha_1, i\omega_1; \alpha_2, i\omega_2|\alpha_{1'}, i\omega_{1'}; \alpha_{2'}, i\omega_{2'})^* = \mathcal{G}^{(2)}(\alpha_{1'}, -i\omega_{1'}; \alpha_{2'}, -i\omega_{2'}|\alpha_1, -i\omega_1; \alpha_2, -i\omega_2) \tag{2.39}$$

Although these are not symmetry properties in the proper sense, these relations will be important for the following considerations.

2.3.2 Time reversal symmetry

In the absence of spin-orbit coupling the Hamiltonian (2.1) is invariant under time reversal. The time reversal symmetry is described by an antiunitary operator Θ with

$$\langle \Theta^{-1}\phi|\psi\rangle = \langle \phi|\Theta\phi\rangle^* \tag{2.40}$$

for any two Hilbert space vectors $|\phi\rangle$ and $|\psi\rangle$. The complex conjugation arises from the antilinearity of Θ.
The transformation of creation and annihilation operators under time reversal is given by [Mes79]

$$\Theta a^\dagger_{\alpha_i,\sigma}\Theta^{-1} = \mathrm{e}^{i\pi\sigma/2} a^\dagger_{\alpha_i,\bar{\sigma}} \tag{2.41}$$

$$\Theta a_{\alpha_i,\sigma}\Theta^{-1} = \mathrm{e}^{-i\pi\sigma/2} a_{\alpha_i,\bar{\sigma}}, \tag{2.42}$$

with $\sigma \pm 1$ and $\bar{\sigma} = -\sigma$.
If the Hamiltonian is time reversal invariant, $\hat{H} = \Theta\hat{H}\Theta^{-1}$, the following relation for the one-particle Green's functions can be derived (see Ref. [Saa11] for details):

$$\mathcal{G}^{(1)}\left(\alpha_1, \sigma_1, i\omega|\alpha_{1'}, \sigma_{1'}\right) = \mathrm{e}^{i\pi(\sigma_1-\sigma_{1'})/2}\mathcal{G}^{(1)}\left(\alpha_1, \bar{\sigma}_1, -i\omega|\alpha_{1'}, \bar{\sigma}_{1'}\right)^*. \tag{2.43}$$

The two-particle Green's function obeys

$$\begin{aligned}&\mathcal{G}^{(2)}\left(\alpha_1, \sigma_1, i\omega_1; \alpha_2, \sigma_2, i\omega_2|\alpha_{1'}, \sigma_{1'}, i\omega_{1'}; \alpha_{2'}, \sigma_{2'}, i\omega_{2'}\right)\\ &= \mathrm{e}^{i\pi(\sigma_1+\sigma_2-\sigma_{1'}-\sigma_{2'})/2}\mathcal{G}^{(2)}\left(\alpha_1, \bar{\sigma}_1, -i\omega_1; \alpha_2, \bar{\sigma}_2, -i\omega_2|\alpha_{1'}, \bar{\sigma}_{1'}, -i\omega_{1'}; \alpha_{2'}, \bar{\sigma}_{2'}, -i\omega_{2'}\right)^*.\end{aligned} \tag{2.44}$$

From relation (2.39) one gets in addition

$$\begin{aligned}&\mathcal{G}^{(2)}\left(\alpha_1,\sigma_1,i\omega_1;\alpha_2,\sigma_2,i\omega_2|\alpha_{1'},\sigma_{1'},i\omega_{1'};\alpha_{2'},\sigma_{2'},i\omega_{2'}\right)\\&=\mathrm{e}^{i\pi(\sigma_1+\sigma_2-\sigma_{1'}-\sigma_{2'})/2}\mathcal{G}^{(2)}\left(\alpha_{1'},\bar{\sigma}_{1'},i\omega_{1'};\alpha_{2'},\bar{\sigma}_{2'},i\omega_{2'}|\alpha_1,\bar{\sigma}_1,i\omega_1;\alpha_2,\bar{\sigma}_2,i\omega_2\right).\end{aligned}\tag{2.45}$$

2.3.3 Particle-hole symmetry

In this section we assume, that the Hamiltonian (2.1) is defined on a bipartite lattice (like e.g. the square or the honeycomb lattice), which can be divided into two sublattices A and B so that neighbouring sites belong to different sublattices. The lattice sites are denoted by α_i. Then we can define a particle-hole transformation, accompanied by a sign change on one of the two sublattices, by

$$Ca_{\alpha_i,\sigma}C^{-1}=\varsigma_{\alpha_i}a^\dagger_{\alpha_i,\sigma}\tag{2.46}$$

$$Ca^\dagger_{\alpha_i,\sigma}C^{-1}=\varsigma_{\alpha_i}a_{\alpha_i,\sigma},\tag{2.47}$$

with $\varsigma_{\alpha_i}=+1(-1)$ if $\alpha_i\in A(B)$.
If the Hamiltonian (2.1) is symmetric with respect to this transformation, the one-particle Green's function obeys (see Ref. [Saa11] for details):

$$\mathcal{G}^{(1)}(\alpha_1,\sigma_1,i\omega|\alpha_{1'},\sigma_{1'})=-\varsigma_{\alpha_1,\alpha_{1'}}\mathcal{G}^{(1)}(\alpha_{1'},\sigma_{1'},-i\omega|\alpha_1,\sigma_1).\tag{2.48}$$

with $\varsigma_{\alpha_1,\alpha_{1'}}=\varsigma_{\alpha_1}\varsigma_{\alpha_{1'}}$. For the two-particle Green's function one finds

$$\begin{aligned}&\mathcal{G}^{(2)}\left(\alpha_1,\sigma_1,i\omega_1;\alpha_2,\sigma_2,i\omega_2|\alpha_{1'},\sigma_{1'},i\omega_{1'};\alpha_{2'},\sigma_{2'},i\omega_{2'}\right)\\&=\varsigma_{\alpha_1,\alpha_2,\alpha_{1'},\alpha_{2'}}\mathcal{G}^{(2)}\left(\alpha_{1'},\sigma_{1'},-i\omega_{1'};\alpha_{2'},\sigma_{2'},-i\omega_{2'}|\alpha_1,\sigma_1,-i\omega_1;\alpha_2,\sigma_2,-i\omega_2\right).\end{aligned}\tag{2.49}$$

with $\varsigma_{\alpha_1,\alpha_2,\alpha_{1'},\alpha_{2'}}=\varsigma_{\alpha_1}\varsigma_{\alpha_2}\varsigma_{\alpha_{1'}}\varsigma_{\alpha_{2'}}$.

2.3.4 Spin rotation invariance

If we assume that the Hamiltonian (2.1) is spin rotation invariant, the one-particle Green's function $\mathcal{G}^{(1)}$ and the self-energy Σ are diagonal in spin space,

$$\mathcal{G}^{(1)}\left(\alpha_1,\sigma_1,i\omega_1|\alpha_{1'},\sigma_{1'}\right)=\mathcal{G}^{(1)}\left(\alpha_1,i\omega_1|\alpha_{1'}\right)\delta_{\sigma_1,\sigma_{1'}}.\tag{2.50}$$

A general two-particle Green's function can be parameterized in the following way:

$$\begin{aligned}\mathcal{G}^{(2)}\left(\alpha_1,\sigma_1;\alpha_2,\sigma_2|\alpha_{1'},\sigma_{1'};\alpha_{2'},\sigma_{2'}\right)&=\mathcal{A}\left(\alpha_1,\alpha_2|\alpha_{1'},\alpha_{2'}\right)\delta_{\sigma_1,\sigma_{1'}}\delta_{\sigma_2,\sigma_{2'}}\\&\quad+\mathcal{B}\left(\alpha_1,\alpha_2|\alpha_{1'},\alpha_{2'}\right)\delta_{\sigma_1,\sigma_{2'}}\delta_{\sigma_2,\sigma_{1'}}.\end{aligned}\tag{2.51}$$

Since $\mathcal{G}^{(2)}(1,2|1',2')$ is antisymmetric under the permutations $1\leftrightarrow 2$ and $1'\leftrightarrow 2'$ the functions $\mathcal{A}$ and $\mathcal{B}$ obey the relation

$$\mathcal{A}\left(\alpha_1,\alpha_2|\alpha_{1'},\alpha_{2'}\right)=-\mathcal{B}\left(\alpha_1,\alpha_2|\alpha_{2'},\alpha_{1'}\right)=-\mathcal{B}\left(\alpha_2,\alpha_1|\alpha_{1'},\alpha_{2'}\right).\tag{2.52}$$

Using the identity

$$2\delta_{\sigma_1,\sigma_{2'}}\delta_{\sigma_2,\sigma_{1'}} = \delta_{\sigma_1,\sigma_{1'}}\delta_{\sigma_2,\sigma_{2'}} + \vec{\sigma}_{\sigma_1,\sigma_{1'}}\vec{\sigma}_{\sigma_2,\sigma_{2'}}, \tag{2.53}$$

we write the two-particle Green's function as

$$\begin{aligned}\mathcal{G}^{(2)}\left(\alpha_1,\sigma_1;\alpha_2,\sigma_2|\alpha_{1'},\sigma_{1'};\alpha_{2'},\sigma_{2'}\right) &= \mathcal{G}_d^{(2)}\left(\alpha_1,\alpha_2|\alpha_{1'},\alpha_{2'}\right)\delta_{\sigma_1,\sigma_{1'}}\delta_{\sigma_2,\sigma_{2'}} \\ &\quad + \mathcal{G}_m^{(2)}\left(\alpha_1,\alpha_2|\alpha_{1'},\alpha_{2'}\right)\vec{\sigma}_{\sigma_1,\sigma_{1'}}\vec{\sigma}_{\sigma_2,\sigma_{2'}},\end{aligned} \tag{2.54}$$

with the density part $\mathcal{G}_d^{(2)}$ and the magnetic part $\mathcal{G}_m^{(2)}$ given by

$$\begin{aligned}\mathcal{G}_d^{(2)}\left(\alpha_1,\alpha_2|\alpha_{1'},\alpha_{2'}\right) &= \mathcal{A}\left(\alpha_1,\alpha_2|\alpha_{1'},\alpha_{2'}\right) + \frac{1}{2}\mathcal{B}\left(\alpha_1,\alpha_2|\alpha_{1'},\alpha_{2'}\right) \\ &= \frac{1}{2}\big[\mathcal{G}^{(2)}\left(\alpha_1,\uparrow;\alpha_2,\uparrow|\alpha_{1'},\uparrow;\alpha_{2'},\uparrow\right) + \mathcal{G}^{(2)}\left(\alpha_1,\uparrow;\alpha_2,\downarrow|\alpha_{1'},\uparrow;\alpha_{2'},\downarrow\right)\big],\end{aligned} \tag{2.55}$$

$$\begin{aligned}\mathcal{G}_m^{(2)}\left(\alpha_1,\alpha_2|\alpha_{1'},\alpha_{2'}\right) &= \frac{1}{2}\mathcal{B}\left(\alpha_1,\alpha_2|\alpha_{1'},\alpha_{2'}\right) \\ &= \frac{1}{2}\big[\mathcal{G}^{(2)}\left(\alpha_1,\uparrow;\alpha_2,\uparrow|\alpha_{1'},\uparrow;\alpha_{2'},\uparrow\right) - \mathcal{G}^{(2)}\left(\alpha_1,\uparrow;\alpha_2,\downarrow|\alpha_{1'},\uparrow;\alpha_{2'},\downarrow\right)\big].\end{aligned} \tag{2.56}$$

In an analogue way one can define a density and magnetic part of the connected Green's function $\mathcal{G}_{d/m}^{c,(2)}$ and of the 1PI vertex function $\gamma_{d/m}^{(2)}$.

2.3.5 Consequences

Let us assume that the Hamiltonian (2.1) is spin rotation and time reversal invariant. Then, Eqs. (2.43) and (2.50) lead to

$$\mathcal{G}^{(1)}\left(\alpha_1,i\omega|\alpha_{1'}\right) = \mathcal{G}^{(1)}\left(\alpha_1,-i\omega|\alpha_{1'}\right)^*. \tag{2.57}$$

If an additional particle-hole symmetry holds, one gets from (2.48)

$$\begin{aligned}\mathcal{G}^{(1)}\left(\alpha_1,i\omega|\alpha_{1'}\right) &= -\varsigma_{\alpha_1,\alpha_{1'}}\mathcal{G}^{(1)}\left(\alpha_{1'},-i\omega|\alpha_1\right) \\ &= -\varsigma_{\alpha_1,\alpha_{1'}}\mathcal{G}^{(1)}\left(\alpha_1,i\omega|\alpha_{1'}\right)^*.\end{aligned} \tag{2.58}$$

The same relations hold for the self-energy Σ.
If we assume that spin rotation invariance and particle-hole symmetry hold, we can deduce the following relation for the two-particle Green's function:

$$\begin{aligned}&\mathcal{G}_{d/m}^{(2)}\left(\alpha_1,i\omega_1;\alpha_2,i\omega_2|\alpha_{1'},i\omega_{1'};\alpha_{2'},i\omega_{2'}\right) \\ &\overset{(2.49)}{=} \varsigma_{\alpha_1,\alpha_2,\alpha_{1'},\alpha_{2'}}\mathcal{G}_{d/m}^{(2)}\left(\alpha_{1'},-i\omega_{1'};\alpha_{2'},-i\omega_{2'}|\alpha_1,-i\omega_1;\alpha_2,-i\omega_2\right) \\ &\overset{(2.39)}{=} \varsigma_{\alpha_1,\alpha_2,\alpha_{1'},\alpha_{2'}}\mathcal{G}_{d/m}^{(2)}\left(\alpha_1,i\omega_1;\alpha_2,i\omega_2|\alpha_{1'},i\omega_{1'};\alpha_{2'},i\omega_{2'}\right)^*.\end{aligned} \tag{2.59}$$

2.4 Lehmann Representation of Green's functions

If the exact eigenstates $|m\rangle$ and energies E_m of the Hamiltonian (2.1) are known, the Green's functions $\mathcal{G}^{(n)}$ can be calculated using the so-called Lehmann representation.

For the one-particle Green's function it is given by

$$\begin{aligned}\mathcal{G}^{(1)}\left(\alpha_1,\tau_1|\alpha_{1'}\right) &= -\frac{1}{Z}\mathrm{Tr}\left[\mathrm{e}^{-\beta\hat{H}}T_\tau a_{\alpha_1}(\tau_1)a^\dagger_{\alpha_{1'}}\right] \\ &= \begin{cases} -\frac{1}{Z}\sum_{m,n}\mathrm{e}^{-\beta E_m}\mathrm{e}^{\tau_1(E_m-E_n)}\left\langle m\right|a_{\alpha_1}\left|n\right\rangle\left\langle n\right|a^\dagger_{\alpha_{1'}}\left|m\right\rangle & \text{for } \tau_1>0 \\ \frac{1}{Z}\sum_{m,n}\mathrm{e}^{-\beta E_m}\mathrm{e}^{-\tau_1(E_m-E_n)}\left\langle m\right|a^\dagger_{\alpha_{1'}}\left|n\right\rangle\left\langle n\right|a_{\alpha_1}\left|m\right\rangle & \text{for } \tau_1<0 \end{cases}.\end{aligned} \tag{2.60}$$

Here we evaluated the trace in the eigenbasis of the Hamiltonian and inserted an unity operator $\mathbf{1}=\sum_n|n\rangle\langle n|$ between a_{α_1} and $a^\dagger_{\alpha_{1'}}$. The expression (2.60) contains now only the eigenenergies of the system and matrix elements of the creation and annihilation operators in the corresponding eigenbasis. The Fourier transform is given by

$$\begin{aligned}\mathcal{G}^{(1)}\left(\alpha_1,i\omega_1|\alpha_{1'}\right) &= \int_0^\beta \mathrm{d}\tau_1\mathrm{e}^{i\omega_1\tau_1}\mathcal{G}^{(1)}\left(\alpha_1,\tau_1|\alpha_{1'}\right) \\ &= \frac{1}{Z}\sum_{m,n}\frac{\mathrm{e}^{-\beta E_m}+\mathrm{e}^{-\beta E_n}}{i\omega_1-(E_n-E_m)}\left\langle m\right|a_{\alpha_1}\left|n\right\rangle\left\langle n\right|a^\dagger_{\alpha_{1'}}\left|m\right\rangle.\end{aligned} \tag{2.61}$$

In a similar way one can derive a Lehmann representation of the two-particle Green's function [HJB+09]. It is given by

$$\begin{aligned}\mathcal{G}^{(2)}\left(\alpha_1,i\omega_1;\alpha_2,i\omega_2|\alpha_{1'},i\omega_{1'};\alpha_{2'}\right) &= \int_0^\beta \mathrm{d}\tau_1\mathrm{d}\tau_2\mathrm{d}\tau_{1'}\mathrm{e}^{i\omega_1\tau_1+i\omega_2\tau_2+i\omega_{1'}\tau_{1'}} \\ &\quad\times\mathcal{G}^{(2)}\left(\alpha_1,\tau_1;\alpha_2,\tau_2|\alpha_{1'},\tau_{1'};\alpha_{2'}\right) \\ &= \frac{1}{Z}\sum_{i,j,k,l}\sum_{\Pi}\phi\left(E_i,E_j,E_k,E_l,i\omega_{\Pi_1},i\omega_{\Pi_2},i\omega_{\Pi_3}\right) \\ &\quad\times\mathrm{sgn}\left(\Pi\right)\left\langle i\right|\mathcal{O}_{\Pi_1}\left|j\right\rangle\left\langle j\right|\mathcal{O}_{\Pi_2}\left|k\right\rangle\left\langle k\right|\mathcal{O}_{\Pi_3}\left|l\right\rangle\left\langle l\right|a^\dagger_{\alpha_{2'}}\left|i\right\rangle.\end{aligned} \tag{2.62}$$

Here, unlike in definition (2.16), the frequencies corresponding to annihilation and creation operators have the same sign, which makes the expression more compact. The operators $\mathcal{O}_i$ are defined by $\mathcal{O}_1=a_{\alpha_1}$, $\mathcal{O}_2=a_{\alpha_2}$ and $\mathcal{O}_3=a^\dagger_{\alpha_{1'}}$. Π denotes the permutation

(Π_1, Π_2, Π_3) of $(1, 2, 3)$. The function ϕ is given by

$$\begin{aligned}
&\phi(E_i, E_j, E_k, E_l, \omega_1, \omega_2, \omega_3) = \frac{1}{i\omega_3 + E_k - E_l} \\
&\times \Bigg[\begin{cases} \left(\frac{\mathcal{E}_{ij}}{(i\omega_1 + E_i - E_j)^2} - \beta \frac{e^{-\beta E_j}}{i\omega_1 + E_i - E_j}\right) & \text{for } \omega_2 = -\omega_3 \text{ and } E_j = E_l \\ \frac{1}{i\omega_2 + i\omega_3 + E_j - E_l}\left(\frac{\mathcal{E}_{ij}}{i\omega_1 + E_i - E_j} - \frac{\mathcal{E}_{il}}{i(\omega_1 + \omega_2 + \omega_3) + E_i - E_l}\right) & \text{else} \end{cases} \\
&- \frac{1}{i\omega_2 + E_j - E_k}\Bigg(\frac{\mathcal{E}_{ij}}{i\omega_1 + E_i - E_j} \\
&- \begin{cases} \beta e^{-\beta E_i} & \text{for } \omega_1 = -\omega_2 \text{ and } E_i = E_k \\ \frac{\mathcal{O}_{ik}}{i\omega_1 + i\omega_2 + E_i - E_k} & \text{else} \end{cases} \Bigg) \Bigg]
\end{aligned} \tag{2.63}$$

with

$$\mathcal{E}_{ij} = \exp(-\beta E_i) + \exp(-\beta E_j), \tag{2.64}$$

$$\mathcal{O}_{ij} = \exp(-\beta E_i) - \exp(-\beta E_j). \tag{2.65}$$

Due to the exponential growth of the Hilbert space, a large numerical effort is required to calculate the multidimensional sum in (2.62), which can be reduced by using particle number and spin conservation and also by calculating the exponential factors (2.64) and (2.65) in advance. But nevertheless, calculating this quantity within a reasonable time can only be performed for a small number of orbitals. In this thesis the largest system included 4 orbitals.

2.5 Real frequency quantities

Up to now all quantities were defined in imaginary time or imaginary Matsubara frequency respectively. This has the advantage that calculating these quantities is much easier than doing the calculations directly in real time or on the real frequency axis. However, experiments are done in real time and to describe them one eventually needs the real time/ real frequency quantities.

As can be seen from the Lehmann representation of the one-particle Green's function (2.61), its poles lie on the real frequency axis and it is fully analytic in the upper and the lower half of the complex plane. Let us denote the analytic continuation of the Matsubara Green's function as $\mathcal{G}^{(1)}(z), z \in \mathbb{C}\backslash\mathbb{R}$.

The analytic continuation of the one-particle Green's function to the upper half of the complex plane evaluated at $z = \omega + i0^+$ is the retarded one-particle Green's function,

$$\begin{aligned}
\mathcal{G}^{(1)}_{\text{ret}}(\alpha_1, \alpha_{1'}, \omega) &= \mathcal{G}^{(1)}\left(\alpha_1, z = \omega + i0^+ | \alpha_{1'}\right) \\
&\overset{(2.61)}{=} \frac{1}{Z} \sum_{m,n} \frac{\mathrm{e}^{-\beta E_m} + \mathrm{e}^{-\beta E_n}}{\omega + i0^+ - (E_n - E_m)} \langle m | a_{\alpha_1} | n \rangle \langle n | a^\dagger_{\alpha_{1'}} | m \rangle .
\end{aligned} \tag{2.66}$$

In the following we choose the single-particle basis in such a way that $\mathcal{G}^{(1)}_{\mathrm{ret}}$ is diagonal, i.e. we have $\mathcal{G}^{(1)}_{\mathrm{ret}}(\alpha_1, \alpha_{1'}, \omega) = \mathcal{G}^{(1)}_{\mathrm{ret}}(\alpha_1, \omega)\,\delta_{\alpha_1,\alpha_{1'}}$. The imaginary part of $\mathcal{G}^{(1)}_{\mathrm{ret}}(\alpha_1, \omega)$ defines the so-called spectral density $A(\alpha_1, \omega)$. From the relation $\frac{1}{\omega - a + i0^+} = \mathcal{P}\frac{1}{\omega - a} - i\pi\delta(\omega - a)$ one gets

$$\begin{aligned} A(\alpha_1, \omega) =& -\frac{1}{\pi}\mathrm{Im}\ \mathcal{G}^{(1)}_{\mathrm{ret}}(\alpha_1, \omega) \\ =& \frac{1}{Z}\sum_{m,n}\left(\mathrm{e}^{-\beta E_m} + \mathrm{e}^{-\beta E_n}\right)\langle m|\, a_{\alpha_1}\,|n\rangle\,\langle n|\, a^\dagger_{\alpha_1}\,|m\rangle\,\delta(\omega - (E_n - E_m))\,. \end{aligned} \tag{2.67}$$

The spectral density is normalized to unity, which follows from

$$\int d\omega A(\alpha_1, \omega) = \langle\{a_{\alpha_1}, a^\dagger_{\alpha_1}\}\rangle = \delta_{\alpha_1,\alpha_1} = 1. \tag{2.68}$$

Together with the positivity $A(\alpha_1, \omega) \geq 0$, which is obvious from the definition (2.67), the normalization property allows the interpretation of $A(\alpha_1, \omega)$ as a propability distribution, describing the spread of the spectral weight associated with the state $a^\dagger_{\alpha_1}|m\rangle$ over the many body states $|n\rangle$. As the spectral density is related to the inelastic scattering cross-section, it is useful for the interpretation of a large class of experiments, like for example scattering experiments in solids or transport measurements in nanoscale devices [AS06]. If the Matsubara Green's function $\mathcal{G}^{(1)}(i\omega_n)$ is only known numerically, the analytic continuation, which is required to calculate the retarded Green's function, becomes mathematically an ill-defined problem. One possible (however criticizable [BGM00]) approach to this problem is the so-called Padé approximation method, where the data is fitted by ratios of polynomials. The analytic continuation is then applied to the fitted functions. In this thesis, we use a Padé scheme, introduced by Vidberg and Serene [VS77]. Applying this scheme one has to be very careful, since the results often depend on the used frequency grid and for many parameter sets unphysical artifacts like negative spectral weights are obtained. To test the reliability of our results, we checked if the shape of the spectral density changes significantly by including more frequencies in the frequency grid. In most cases we obtained only stable results for the spectral density at small frequencies, and the high frequency behaviour could only resolved on a qualitative level.

Chapter 3

Functional Renormalization Group

Renormalization group (RG) methods are a powerful tool for the description of quantum many particle systems. Based on the pioneering works of Wilson, who used RG ideas to understand the universality of critical phenomena [Wil71, WK74], the so-called functional renormalization group (fRG) [Pol84, Wet93, SH01] has become a widely used scheme for the investigation of interacting Fermi and Bose systems. The term "functional" indicates that it is based on an exact flow equation for a generating functional. A recent review of this method can be found in Ref. [MSH$^+$12] and a detailed introduction is given in [KBS10].

In the context of impurity models RG methods are used since the early seventies. To explain the spin screening physics of the Kondo model, Anderson developed a "poor man's scaling" procedure [And70], which corresponds to a RG approach where the conduction electron bandwidth W is systematically reduced. When W approaches the Kondo scale T_K, the antiferromagnetic coupling strength J diverges, which marks the crossover to a strong coupling fixed point in the RG flow, associated with a spin compensated ground state. However Anderson's argument relies on a perturbational description, and can not describe this low energy state directly. In 1975, Wilson developed his numerical RG method (NRG), which allows for a non-perturbative description of the Kondo problem on all energy scales. Initially it was applied to the Kondo model [Wil75] and later also extended to the Anderson Impurity model [KmWW80a, KmWW80b]. A review of the NRG method is given in Ref. [BCP08] and in the book of Hewson [Hew93].

Although more complex impurity setups can be described by the NRG as well, this requires a significant increase of the computational effort. This motivated several groups in the last decade to develop fRG approaches, which can be applied to a large class of impurity problems with a reasonable level of numerical expense. These approaches [KEM06, BFCK09, JPS10], although they differ in the used cutoff or regularization scheme, base on the same fRG flow equation for the generating functional of the 1PI vertex functions. In this chapter we derive this equation without specifiying the used

cutoff and dicuss possible approximation schemes. Our derivation mainly follows Ref. [Med06].

3.1 General fRG formalism

The fRG flow equation for the generating functional of the 1PI vertex functions is a differential equation with respect to a flow parameter Λ, that is introduced in the free propagator

$$\mathcal{G}_0 \to \mathcal{G}_0^\Lambda, \tag{3.1}$$

in such a way that $\mathcal{G}_0^{\Lambda_0} \equiv 0$ and $\mathcal{G}_0^{\Lambda_{\text{end}}} \equiv \mathcal{G}_0$. This condition leads to a simple initial condition of the fRG flow equations.
The generating functional (2.18) becomes then Λ-dependent,

$$\mathcal{Z}^\Lambda[\bar{\eta},\eta] = \frac{1}{\mathcal{Z}_0^\Lambda}\int \mathcal{D}[\bar{\psi},\psi]\exp\left[(\bar{\psi},Q^\Lambda\psi) - \mathcal{V}(\bar{\psi},\psi) - (\bar{\psi},\eta) - (\bar{\eta},\psi)\right], \tag{3.2}$$

where $\mathcal{V}$ is the interaction part of $\mathcal{H}$. In comparison to (2.18) the functional integral in (3.2) is normalized with the free partition function $\mathcal{Z}_0^\Lambda = \det(-Q^\Lambda)$. This change leads only to an additional term $\ln(\mathcal{Z}_0)$ in the generating functionals $\mathcal{W}$ and Γ, and does not influence the definition of the n-particle vertex functions.
The generating functional for the Λ-dependent connected Green's functions $\mathcal{W}^\Lambda$ is obtained as

$$\mathrm{e}^{\mathcal{W}^\Lambda[\bar{\eta},\eta]} = \mathcal{Z}^\Lambda[\bar{\eta},\eta] \tag{3.3}$$

After differentiating (3.3) with respect to Λ we get

$$\begin{aligned}\frac{d\mathcal{W}^\Lambda[\bar{\eta},\eta]}{d\Lambda}\mathrm{e}^{\mathcal{W}^\Lambda[\bar{\eta},\eta]} &= -\operatorname{Tr}\left[\dot{Q}^\Lambda\mathcal{G}_0^\Lambda\right]\mathrm{e}^{\mathcal{W}^\Lambda[\bar{\eta},\eta]} \\ &\quad + \frac{1}{\mathcal{Z}_0^\Lambda}\int\mathcal{D}[\bar{\psi},\psi](\bar{\psi},\dot{Q}^\Lambda\psi)\exp\left[(\bar{\psi},Q^\Lambda\psi) - \mathcal{V}(\bar{\psi},\psi) - (\bar{\psi},\eta) - (\bar{\eta},\psi)\right] \\ &= -\left[\operatorname{Tr}\left(\mathcal{G}_0^\Lambda\dot{Q}^\Lambda\right) + \Delta_{\dot{Q}^\Lambda}\right]\mathrm{e}^{\mathcal{W}^\Lambda[\bar{\eta},\eta]},\end{aligned} \tag{3.4}$$

with the Laplace operator Δ_Q defined by

$$\Delta_Q = \left(\frac{\delta}{\delta\eta}, Q\frac{\delta}{\delta\bar{\eta}}\right). \tag{3.5}$$

We finally arrive at a flow equation for the functional $\mathcal{W}^\Lambda[\bar{\eta},\eta]$

$$\frac{d\mathcal{W}^\Lambda[\bar{\eta},\eta]}{d\Lambda} = -\operatorname{Tr}\left(\mathcal{G}_0^\Lambda\dot{Q}^\Lambda\right) + \operatorname{Tr}\left(\dot{Q}^\Lambda\frac{\delta^2\mathcal{W}^\Lambda[\bar{\eta},\eta]}{\delta\eta\delta\bar{\eta}}\right) - \left(\frac{\delta\mathcal{W}^\Lambda[\bar{\eta},\eta]}{\delta\eta}, \dot{Q}^\Lambda\frac{\delta\mathcal{W}^\Lambda[\bar{\eta},\eta]}{\delta\bar{\eta}}\right). \tag{3.6}$$

As discussed in Ref. [Med06] this equation is no well-defined initial value problem and can only be used as intermediate step in the derivation of a more convenient flow equation. Using Eq. (2.30) we obtain

$$\begin{aligned}\frac{d\Gamma^{\Lambda}\left[\bar{\phi},\phi\right]}{d\Lambda} &= -\frac{d\mathcal{W}^{\Lambda}\left[\bar{\eta},\eta\right]}{d\Lambda} + \left(\bar{\phi},\dot{Q}^{\Lambda}\phi\right) \\ &= \mathrm{Tr}\left[\dot{Q}^{\Lambda}\left(\frac{\delta^2\mathcal{W}^{\Lambda}\left[\bar{\eta},\eta\right]}{\delta\eta\delta\bar{\eta}} + \mathcal{G}_0^{\Lambda}\right)\right] \\ &= \mathrm{Tr}\left[\dot{Q}^{\Lambda}\left[\left(\frac{\delta^2\Gamma^{\Lambda}\left[\bar{\phi},\phi\right]}{\delta\bar{\phi}\delta\phi} + Q^{\Lambda}\right)^{-1} + \mathcal{G}_0^{\Lambda}\right]\right]. \end{aligned} \tag{3.7}$$

Eq. (3.7) is an exact flow equation for the generating functional of the 1PI vertices at scale Λ. Being formally exact, it depends on all orders of the fields and an exact solution is far out of reach. Therefore truncations are unavoidable. In the next section we will expand the generating functional Γ^{Λ} with respect to the fields, and derive flow equations for the 1PI vertex functions, which can be systematically truncated.

3.2 Flow equations for the 1PI vertices

In analogy to Eq. (2.31), we define the Λ-dependent 1PI vertex functions

$$\Gamma^{\Lambda}\left[\bar{\phi},\phi\right] = \sum_{n=0}^{\infty}\frac{(-1)^n}{n!^2}\sum_{\substack{\alpha_1,\ldots,\alpha_n\\ \alpha_{1'},\ldots,\alpha_{n'}}}\gamma^{(n),\Lambda}\left(\alpha_1,\ldots,\alpha_n|\alpha_{1'},\ldots,\alpha_{n'}\right)\bar{\phi}_{\alpha_1}\ldots\bar{\phi}_{\alpha_n}\phi_{\alpha_{n'}}\ldots\phi_{\alpha_{1'}}. \tag{3.8}$$

Inserting this expansion into Eq. (3.7) leads to an infinite set of flow equations for the Λ-dependent vertex functions $\gamma^{(n),\Lambda}$. The flow equations for the self-energy $\Sigma^{\Lambda} \equiv -\gamma^{(1),\Lambda}$ and the two-particle vertex $\gamma^{(2),\Lambda}$ are

$$\frac{d}{d\Lambda}\Sigma^{\Lambda}(\alpha_1|\alpha_{1'}) = -\,\mathrm{Tr}\left[S^{\Lambda}\gamma^{(2),\Lambda}(\alpha_1,.|\alpha_{1'},.)\right], \tag{3.9}$$

$$\begin{aligned}\frac{d}{d\Lambda}\gamma^{(2),\Lambda}(\alpha_1,\alpha_2|\alpha_{1'},\alpha_{2'}) =& \mathrm{Tr}\left[S^{\Lambda}\gamma^{(3),\Lambda}(\alpha_1,\alpha_2,.|\alpha_{1'},\alpha_{2'},.)\right] \\ &- \mathrm{Tr}\left[S^{\Lambda}\gamma^{(2),\Lambda}(.,.|\alpha_{1'},\alpha_{2'})[\mathcal{G}^{\Lambda}]^T\gamma^{(2),\Lambda}(\alpha_1,\alpha_2|.,.)\right] \\ &- \mathrm{Tr}\left[S^{\Lambda}\gamma^{(2),\Lambda}(\alpha_1,.|\alpha_{1'},.)\mathcal{G}^{\Lambda}\gamma^{(2),\Lambda}(\alpha_2,.|\alpha_{2'},.)\right] \\ &- [\alpha_1 \leftrightarrow \alpha_2] - [\alpha_{1'} \leftrightarrow \alpha_{2'}] + [\alpha_1 \leftrightarrow \alpha_2, \alpha_{1'} \leftrightarrow \alpha_{2'}], \end{aligned} \tag{3.10}$$

where S^{Λ} is the so-called single scale propagator defined as

$$S^{\Lambda} = \mathcal{G}^{\Lambda}\frac{d}{d\Lambda}\left[Q^{\Lambda}\right]\mathcal{G}^{\Lambda}, \tag{3.11}$$

and $\mathcal{G}^{\Lambda} = \left[Q^{\Lambda} - \Sigma^{\Lambda}\right]^{-1}$ is the full Λ-dependent Green's function.

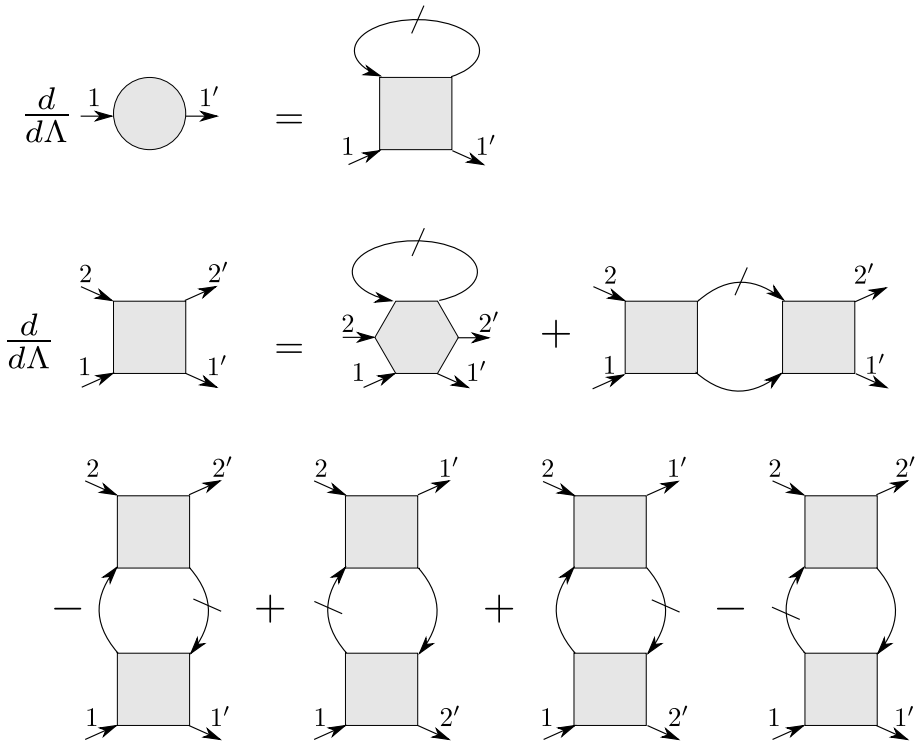

Figure 3.1: Diagrammatic representation of the flow equations (3.9) and (3.10). The line with a slash denotes the single scale propagator S^Λ and the other line represents the full Λ-dependent Green's function $\mathcal{G}^\Lambda$.

In Fig. 3.1 we show a diagrammatic representation of the flow equations (3.9) and (3.10). The terms on the right hand side of the flow equation for $\gamma^{(2),\Lambda}$ appear in the same order as in equation (3.10). The first term includes the three-particle vertex $\gamma^{(3),\Lambda}$, while the other terms (so-called one-loop diagrams) only depend on $\gamma^{(1),\Lambda}$ and $\gamma^{(2),\Lambda}$. The second term is called particle-particle graph and the terms in the second line are particle-hole graphs. The terms 3 and 6 are called direct particle-hole graphs and the terms 4 and 5 crossed particle-hole graphs.

At the initial scale Λ_0 the free propagator of the theory (3.1) vanishes, such that only the bare vertices remain. For the Hamiltonian (2.1) this leads to the initial conditions

$$\Sigma^{\Lambda_0}(\alpha_1, \alpha_{1'}) = 0, \tag{3.12}$$

$$\gamma^{(2),\Lambda_0}(\alpha_1, \alpha_2 | \alpha_{1'}, \alpha_{2'}) = V_{\alpha_1\alpha_2\alpha_{1'}\alpha_{2'}}, \tag{3.13}$$

$$\gamma^{(n\geq 3),\Lambda_0}(\alpha_1, ..., \alpha_n | \alpha_{1'}, ..., \alpha_{n'}) = 0. \tag{3.14}$$

In each integration step more and more degrees of freedom are included until for $\Lambda = \Lambda_{\text{end}}$ the original theory is recovered.

3.3 Truncations

Although the infinite set of flow equations for the 1PI vertices is formally exact, it is practically impossible to solve it due to the infinite number of involved degrees of freedom. Therefore one has to apply a truncation procedure leading to a finite set of equations, which can be solved at least numerically. In this section we discuss two such truncation schemes, which we call approximation 1 and approximation 2 respectively.
In the flow equations (3.9) and (3.10) the flow of $\gamma^{(1),\Lambda}$ depends only on $\gamma^{(1),\Lambda}$ and $\gamma^{(2),\Lambda}$, while the flow of $\gamma^{(2),\Lambda}$ is determined by $\gamma^{(1),\Lambda}$, $\gamma^{(2),\Lambda}$ and $\gamma^{(3),\Lambda}$. This structure continues in the flow equations for the higher vertices $\gamma^{(n),\Lambda}$ with $n \geq 3$ in which the right hand side only depends on vertices $\gamma^{(i),\Lambda}$ with $i \leq n+1$.
This observation motivates the following truncation scheme: Neglecting the flow of $\gamma^{(n+1),\Lambda}$ and all higher vertex functions leads to a closed system of differential equations for the vertex functions $\gamma^{(1),\Lambda}, ..., \gamma^{(n),\Lambda}$. As the neglected higher vertex functions depend on higher orders of the bare interaction, this truncation scheme can be justified by perturbational arguments. However, we want to emphasize that integrating the reduced set of flow equations involves contributions from arbitrary high orders and the final result will in general be much better than simple perturbation theory.
In the case $n = 1$ (in the following called approximation 1) one is left with Eq. (3.9), where $\gamma^{(2),\Lambda}$ is set to the initial interaction

$$\frac{d}{d\Lambda}\Sigma^{\Lambda}(\alpha_1|\alpha_{1'}) = -\sum_{\alpha_2,\alpha_{2'}} S^{\Lambda}(\alpha_2|\alpha_{2'})V(\alpha_1,\alpha_2|\alpha_{1'},\alpha_{2'}). \tag{3.15}$$

If one neglects the feedback of Σ^{Λ} on the right hand side of the flow equation, the single scale propagator S^{Λ} is given by $S^{\Lambda} = -\frac{d}{d\Lambda}\mathcal{G}_0^{\Lambda}$. Integrating this equation corresponds then to first order perturbation theory. From this consideration one explicitly sees that the solution of the full equation (3.15) includes diagrams beyond the lowest order perturbation theory, although no vertex corrections are considered at this level of the approximation.
The latter come into play in the case $n = 2$ (which we call approximation 2 or one-loop approximation). Here one considers the equations (3.9) and (3.10), whereat we neglect the flow of the three-particle vertex $\gamma^{(3),\Lambda}$. Since it vanishes in the beginning for $\Lambda = \Lambda_0$ the first term of Eq. (3.10) then remains zero during the whole flow. Motivated by the fulfillment of Ward identities in the fRG flow, the following replacement in Eq. (3.10) was proposed [Kat04],

$$S^{\Lambda} \to -\frac{d\mathcal{G}^{\Lambda}}{d\Lambda} = S^{\Lambda} - \mathcal{G}^{\Lambda}\frac{d\Sigma^{\Lambda}}{d\Lambda}\mathcal{G}^{\Lambda}\,. \tag{3.16}$$

Using this replacement, additional diagrams contribute to the flow of the two-particle vertex. As an example we show in Fig. 3.2 the particle-particle diagram, where the single scale propagator is replaced by the term $\mathcal{G}^{\Lambda}\frac{d\Sigma^{\Lambda}}{d\Lambda}\mathcal{G}^{\Lambda}$. The latter can be expressed by the

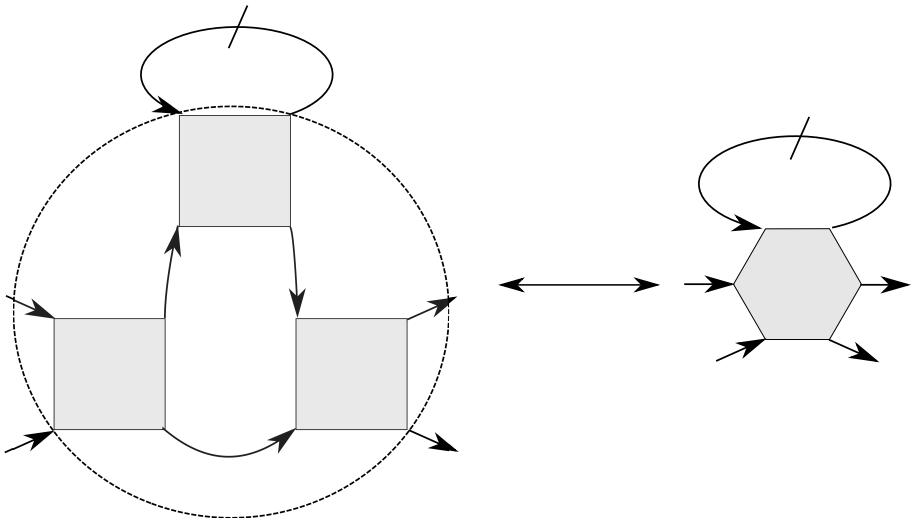

Figure 3.2: Using the replacement (3.16) in the flow equation (3.10), additional diagrams, which originate from the flow of the three-particle vertex, and would be neglected on this approximation level otherwise, are included in the flow of the two-particle vertex. In the figure we show one such diagram, which is generated from the particle-particle diagram with the replacement (3.16).

right hand side of the flow equation for the self-energy (3.9), leading to a diagram that is of third order in the two-particle vertex. Similar diagrams are also generated in the particle-hole channels. In the original flow scheme they appear on the right hand side of the flow equation of $\gamma^{(3),\Lambda}$, such that using the replacement (3.16), contributions from the three-particle vertex are included on the level of the one-loop approximation.

Chapter 4

Hybridization flow

In this chapter we introduce the hybridization flow concept, which is applied in the following chapters. We begin with a brief introduction to the Anderson impurity model, and show, how a general bath can be mapped onto a semi-infinite chain. In the next step this chain is then divided into two parts: The core contains the correlated site and the first L bath sites and the bath includes the remaining bath sites. Both parts are coupled by a flow parameter Λ. The idea of the hybridization flow is now, to turn on the coupling between core and bath slowly, starting from the exactly solvable core. Our scheme is implemented in an effective bath theory on the first bath site next to the core. The fRG flow equations for this effective bath theory are derived and compared with other implementations of the hybridization flow. A generalization of the hybridization flow scheme to multi-impurity problems, which appear in the context of cluster DMFT (cf. chapter 6), can be found in appendix D.

Parts of this chapter are already published in

M. Kinza, J. Ortloff, J. Bauer, and C. Honerkamp. Alternative functional renormalization group approach to the single impurity Anderson model. *Phys. Rev. B*, 87:035111, Jan 2013

4.1 Anderson Impurity model

The single impurity Anderson model [And61] is a minimal model to describe the interplay of charge and spin fluctuations of a localized interacting impurity in a metallic environment. This impurity could be for example the d- or f-level of a transition metal atom such as Fe embedded in a nonmagnetic metal. In such systems one observes an anomalous minimum in the electrical resisitivity at very low temperatures, which is caused by the interaction of the conduction electrons with the impurities [dHdBvdB34]. It was first

explained by Jun Kondo in 1964 [Kon64], based on the so-called Kondo model, which describes a local magnetic moment associated with a spin S, coupled by an antiferromagnetic exchange interaction J to the conduction electrons. In a certain parameter regime it can be deduced from the Anderson model. Another experimental sitation that can be described by the Anderson model is found in nanoscale devices, in which quantum dots are coupled to metallic leads. In certain cases they can be described by the Anderson model and the Kondo effect was observed [GGSM+97]. Finally, the Anderson model is an important ingredient of the dynamical mean field theory for correlated lattice models, which will be further discussed in chapter 6.
The Hamiltonian of the SIAM consists of three parts

$$\hat{H} = \hat{H}_{\text{dot}} + \hat{H}_{\text{bath}} + \hat{H}_{\text{hybridization}} \,. \tag{4.1}$$

$\hat{H}_{\text{dot}}$ describes the interacting electron level and is given by

$$\hat{H}_{\text{dot}} = \sum_{\sigma} \left(\epsilon_{d,\sigma} - \mu\right) d_{\sigma}^{\dagger} d_{\sigma} + U \; n_{d,\uparrow} n_{d,\downarrow} \,. \tag{4.2}$$

The operators $d_{\sigma}^{\dagger}$ and d_{σ} create and annihilate electrons on the dot level with spin component $\sigma = \pm 1$ and $n_{d,\sigma} = d_{\sigma}^{\dagger} d_{\sigma}$ is the particle number operator. Occupying the dot level with two electrons costs a repulsive interaction energy $U > 0$ caused by the Coulomb Interaction. The onsite energy is given by

$$\epsilon_{d,\sigma} - \mu = -\frac{U}{2} + V_g + B\sigma \,. \tag{4.3}$$

including a magnetic field B and a gate voltage V_g. The term $-\frac{U}{2}$ is choosen such that $V_g = 0$ corresponds to the particle-hole symmetric point.
The bath is modeled as a noninteracting electron gas

$$\hat{H}_{\text{bath}} = \sum_{s=L,R} \sum_{\vec{k},\sigma} \left(\epsilon_{\vec{k},\sigma} - \mu\right) b_{\vec{k},\sigma,s}^{\dagger} b_{\vec{k},\sigma,s}. \tag{4.4}$$

Here the index s distinguishes between different channels "left" (L) and "right" (R), which is the typical situation in a quantum dot setup. The operators $b_{\vec{k},\sigma,s}^{\dagger}$ and $b_{\vec{k},\sigma,s}$ create and annihilate electrons with wave vector $\vec{k}$ and spin component σ in channel s.
The coupling of the dot and the bath levels due to hybridization is described by the Hamiltonian

$$\hat{H}_{\text{hybridization}} = -\sum_{s=L,R} \sum_{\vec{k},\sigma} \left(V_{\vec{k},s} \; d_{\sigma}^{\dagger} b_{\vec{k},\sigma,s} + V_{\vec{k},s}^{*} \; b_{\vec{k},\sigma,s}^{\dagger} d_{\sigma} \right). \tag{4.5}$$

We can do an unitary transformation

$$\begin{pmatrix} b_{\vec{k},\sigma,\text{even}} \\ b_{\vec{k},\sigma,\text{odd}} \end{pmatrix} = \frac{1}{\sqrt{|V_{\vec{k},L}|^2 + |V_{\vec{k},R}|^2}} \begin{pmatrix} V_{\vec{k},L} & V_{\vec{k},R} \\ V_{\vec{k},R}^{*} & -V_{\vec{k},L}^{*} \end{pmatrix} \begin{pmatrix} b_{\vec{k},\sigma,L} \\ b_{\vec{k},\sigma,R} \end{pmatrix}, \tag{4.6}$$

such that only the even combination couples to the dot site, since the left and right part of the chain possess the same chemical potential

$$\hat{H}_{\text{hybridization}} = -\sum_{\vec{k},\sigma} v_{\vec{k}} \left(d_\sigma^\dagger b_{\vec{k},\sigma,\text{even}} + b_{\vec{k},\sigma,\text{even}}^\dagger d_\sigma \right) \tag{4.7}$$

where $v_{\vec{k}} = \sqrt{|V_{\vec{k},L}|^2 + |V_{\vec{k},R}|^2}$. $\hat{H}_{\text{bath}}$ remains formally unchanged. In the following we ignore the decoupled odd bath, and skip the index "even" on the remaining even bath. Although the Hamiltonian (4.1) looks very simple, it turns out to be a non-trivial many body problem, whose physical behaviour emerges from the competition of the bare energy scales, i.e. the onsite interaction U, the dot level position $\epsilon_{d,\sigma}$, the bandwidth of the bath W, and the hybridization strength Δ, which is quantified by the hybridization function

$$\Delta(i\omega) = \sum_{\vec{k}} \frac{v_{\vec{k}}^2}{i\omega - \epsilon_k}. \tag{4.8}$$

This hybridization function enters the local noninteracting ($U = 0$) Green's function on the dot site via[1]

$$\mathcal{G}_0\left(i\omega, d, d\right) = \frac{1}{i\omega - \epsilon_d - \Delta(i\omega)} \tag{4.9}$$

For a particle-hole symmetric bath dispersion the hybridization function is purely imaginary, and we assume that it is nearly constant at small frequencies, i.e. we have $\Delta(i\omega) \approx -i\Delta_0 \,\text{sign}(\omega)$. This leads to a Lorentz-shaped central resonance in the spectral density, given by

$$\begin{aligned} A_{\text{dot},0}(\omega) &= -\frac{1}{\pi} \text{Im}\ \mathcal{G}_0(\omega + i0^+, d, d) \\ &\approx \frac{1}{\pi} \frac{\Delta_0}{(\omega - \epsilon_d)^2 + \Delta_0^2} \quad \text{for small } \omega. \end{aligned} \tag{4.10}$$

Its width is determined by the hybridization strength Δ_0. For large interactions $U \gg \Delta_0$ the spectrum exhibits a three-peak structure. Beside a central resonance at $\omega = 0$ (the so-called Kondo resonance), one finds additional peaks at ϵ_d and $\epsilon_d + U$ that are due to charge fluctuations, the so-called Hubbard bands. If $\epsilon_d \ll 0$, $\epsilon_d + U \gg 0$ and $|\epsilon_d + U|, |\epsilon_d| \gg \Delta_0$ these charge fluctuations are negligable and the Anderson model can be mapped to the Kondo model [SW66], which describes a single localized spin coupled by an antiferromagnetic exchange coupling J to the conduction electrons. At low enough temperatures the spin fluctuations are governed by a new energy scale, which is exponentially small in the bare interaction strength U, the so-called Kondo scale [Hew93]

$$T_K = W \sqrt{\frac{2\Delta_0}{\pi U}} \exp\left(-\frac{\pi U}{8\Delta_0} \right). \tag{4.11}$$

[1] Here and in the rest of the section we set $B = 0$ and skip the spin index.

In the Kondo regime the SIAM is described by a local Fermi liquid [Noz74], with quasi-particle weight Z defined as

$$Z^{-1} = 1 - \left.\frac{\mathrm{dIm}\Sigma_{\mathrm{dot}}\left(i\omega\right)}{\mathrm{d}\omega}\right|_{\omega=0^+}. \tag{4.12}$$

$\Sigma_{\mathrm{dot}}\left(i\omega\right)$ is the dot self-energy. The width of the central Kondo resonance is determined by the quasi-particle weight Z as $Z\Delta_0$ and Z is proportional to the Kondo scale $Z \propto T_K$. The spectral density at $\omega = 0$ is pinned to the value

$$A_{\mathrm{dot}}\left(\omega = 0\right) = \frac{\sin^2\left(\eta(\omega = 0)\right)}{\pi\Delta_0} \tag{4.13}$$

with the phase-shift $\eta(\omega = 0)$, which is determined by Friedel's sum rule $\eta(\omega = 0) = \pi\langle n_{d,\sigma}\rangle$ [Lan66]. At particle-hole symmetry we have $\langle n_{d,\sigma}\rangle = 1/2$, such that $A_{\mathrm{dot}}\left(\omega = 0\right) = \frac{1}{\pi\Delta_0}$, independent of the interaction U.

4.1.1 Mapping to a linear chain

In order to apply our hybridization flow scheme, we have to map the SIAM to a semi-infinite tight binding chain. This can be achieved by the Lanczos algorithm, described for example in chapter 4.2 of Ref. [Hew93].
We write the hybridization matrix-element in the form $v_{\vec{k}} = v\alpha_{\vec{k}}$, such that $\sum_{\vec{k}} \alpha_{\vec{k}}^2 = 1$. With this we introduce the state $|b_1\rangle$ with the creation operator

$$b_{1,\sigma}^\dagger = \sum_k \alpha_k b_{\vec{k},\sigma}^\dagger. \tag{4.14}$$

The part of the Hamiltonian, that describes the hybridization between the bath and the dot (4.7) is then given by

$$\hat{H}_{\mathrm{hybridization}} = -v\sum_\sigma \left(d_\sigma^\dagger b_{1,\sigma} + b_{1,\sigma}^\dagger d_\sigma\right), \tag{4.15}$$

i.e. the dot site couples directly to the localized state $|b_1\rangle$. Starting from $|b_1\rangle$ we construct a new basis for the bath from the states $|b_1\rangle, \hat{H}_{\mathrm{bath}}|b_1\rangle, \hat{H}_{\mathrm{bath}}^2|b_1\rangle, \hat{H}_{\mathrm{bath}}^3|b_1\rangle, ...$ by Schmidt orthogonalization. In this new basis $\hat{H}_{\mathrm{bath}}$ is tridiagonal and corresponds to a semi-infinite tight binding chain with nearest neighbour hopping only. The new basis is given by the states

$$\begin{aligned}
|b_2\rangle &= \frac{1}{t_1}\left(\hat{H}_{\mathrm{bath}}|b_1\rangle - |b_1\rangle\langle b_1|\hat{H}_{\mathrm{bath}}|b_1\rangle\right),\\
|b_3\rangle &= \frac{1}{t_2}\left(\hat{H}_{\mathrm{bath}}|b_2\rangle - |b_2\rangle\langle b_2|\hat{H}_{\mathrm{bath}}|b_2\rangle - |b_1\rangle\langle b_1|\hat{H}_{\mathrm{bath}}|b_2\rangle\right),\\
&...,\\
|b_{n+1}\rangle &= \frac{1}{t_n}\left(\hat{H}_{\mathrm{bath}}|b_n\rangle - |b_n\rangle\langle b_n|\hat{H}_{\mathrm{bath}}|b_n\rangle - |b_{n-1}\rangle\langle b_{n-1}|\hat{H}_{\mathrm{bath}}|b_n\rangle\right),
\end{aligned}$$

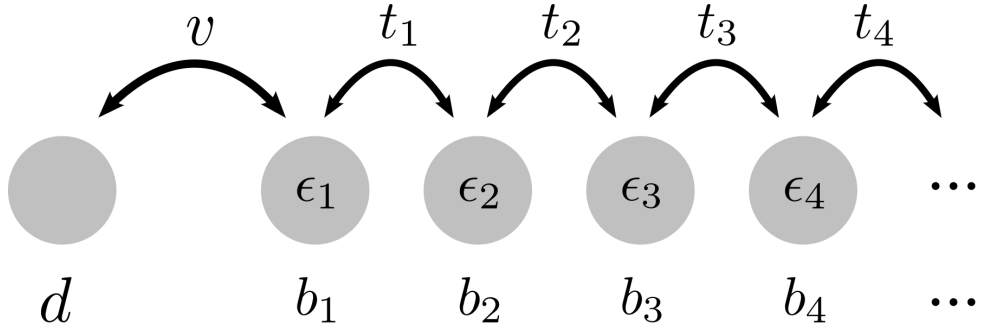

Figure 4.1: The single impurity Anderson model in the form of a semi-infinite tight binding chain, corresponding to Hamiltonian (4.16). The first site (d) is the correlated impurity site and the other sites (b_i) are the bath sites.

with $t_n = \langle b_{n+1}| \hat{H}_{\text{bath}} |b_n\rangle$. If we define $\epsilon_n = \langle b_n| \hat{H}_{\text{bath}} |b_n\rangle$, we can write $\hat{H}_{\text{bath}}$ in the form

$$\hat{H}_{\text{bath}} = \sum_{n,\sigma} \epsilon_n b^\dagger_{n,\sigma} b_{n,\sigma} + \sum_{n,\sigma} \left(t_n b^\dagger_{n,\sigma} b_{n+1,\sigma} + t^*_n b^\dagger_{n+1,\sigma} b_{n,\sigma} \right), \tag{4.16}$$

which is illustrated in Fig. 4.1.

4.1.2 Green's function of the SIAM

The inverse free Green's function $Q(i\omega) = \mathcal{G}_0(i\omega)^{-1}$ on the imaginary frequency axis is given by $Q(i\omega) = i\omega \mathbf{1} - \hat{H}_0$, where $\hat{H}_0$ is the noninteracting part of the Hamiltonian (4.1), ignoring the odd bath (cf. Eq. (2.8)). Written as a matrix it is given by

$$Q(i\omega) = \left[\begin{array}{c|c} Q_\uparrow(i\omega) & 0 \\ \hline 0 & Q_\downarrow(i\omega) \end{array}\right] \tag{4.17}$$

$$Q_\sigma(i\omega) = \left[\begin{array}{c|ccccc} & d & b_1 & b_2 & b_3 & \cdots \\ \hline d & i\omega + \mu - \epsilon_{d,\sigma} & v & & & \\ b_1 & v & i\omega + \mu - \epsilon_1 & t_1 & & \\ b_2 & & t_1^* & i\omega + \mu - \epsilon_2 & t_2 & \\ b_3 & & & t_2^* & i\omega + \mu - \epsilon_3 & \cdots \\ \cdots & & & & \cdots & \cdots \end{array}\right]. \tag{4.18}$$

The inverse of $Q_\sigma(i\omega)$ can be calculated by using the identity

$$\left[\begin{array}{c|c} A & B \\ \hline C & D \end{array}\right]^{-1} = \left[\begin{array}{c|c} (A - BD^{-1}C)^{-1} & -(A - BD^{-1}C)^{-1} BD^{-1} \\ \hline -D^{-1}C(A - BD^{-1}C)^{-1} & (D - CA^{-1}B)^{-1} \end{array}\right], \tag{4.19}$$

which is valid for arbitrary invertible matrices A, B, C and D. If we introduce the bath Green's function $g_{b_1,b_2,\ldots}(i\omega)$ by

$$g^{-1}_{b_1,b_2,\ldots}(i\omega) = \left[\begin{array}{c|cccc} & b_1 & b_2 & b_3 & \cdots \\ \hline b_1 & i\omega+\mu-\epsilon_1 & t_1 & & \\ b_2 & t_1^* & i\omega+\mu-\epsilon_2 & t_2 & \\ b_3 & & t_2^* & i\omega+\mu-\epsilon_3 & \cdots \\ \cdots & & & \cdots & \cdots \end{array}\right], \tag{4.20}$$

we can derive the free Green's function on the dot site by the identity (4.19)

$$\mathcal{G}_{0,\sigma}(i\omega,d,d) = \left[i\omega+\mu-\epsilon_{d,\sigma}-\Delta(i\omega)\right]^{-1}. \tag{4.21}$$

Here $\Delta(i\omega)$ is the hybridization function, which is given by

$$\Delta(i\omega) = v^2 g_{b_1,b_2,\ldots}(i\omega,b_1,b_1). \tag{4.22}$$

By the Dyson equation (2.36) the full Green's function is related to $Q_\sigma(i\omega)$ and the self-energy

$$\begin{aligned}\mathcal{G}_\sigma(i\omega)^{-1} =& Q_\sigma(i\omega)-\Sigma_\sigma(i\omega)\\ =& \left[\begin{array}{c|ccccc} & d & b_1 & b_2 & b_3 & \cdots \\ \hline d & i\omega+\mu-\epsilon_{d,\sigma}-\Sigma_{\mathrm{dot},\sigma}(i\omega) & v & & & \\ b_1 & v & i\omega+\mu-\epsilon_1 & t_1 & & \\ b_2 & & t_1^* & i\omega+\mu-\epsilon_2 & t_2 & \\ b_3 & & & t_2^* & i\omega+\mu-\epsilon_3 & \cdots \\ \cdots & & & & \cdots & \cdots \end{array}\right].\end{aligned} \tag{4.23}$$

Note that the self-energy is located on the dot site, since the bath sites are noninteracting. Inverting the matrix (4.23), using the identity (4.19), gives the full Green's function on the dot

$$\mathcal{G}_\sigma(i\omega,d,d) = \left[i\omega+\mu-\epsilon_{d,\sigma}-\Sigma_{\mathrm{dot},\sigma}(i\omega)-\Delta(i\omega)\right]^{-1}. \tag{4.24}$$

In the same way one gets the Green's function for the first and second bath site,

$$\mathcal{G}_\sigma(i\omega,b_1,b_1) = \left[i\omega+\mu-\epsilon_1-\frac{v^2}{i\omega+\mu-\epsilon_{d,\sigma}-\Sigma_{\mathrm{dot},\sigma}(i\omega)}-|t_1|^2 g_{b_2,b_3,\ldots}(i\omega,b_2,b_2)\right]^{-1}, \tag{4.25}$$

$$\mathcal{G}_\sigma(i\omega,b_2,b_2) = \left[i\omega+\mu-\epsilon_2-\frac{|t_1|^2}{i\omega+\mu-\epsilon_1-\frac{v^2}{i\omega+\mu-\epsilon_{d,\sigma}-\Sigma_{\mathrm{dot},\sigma}(i\omega)}}-|t_2|^2 g_{b_3,b_4,\ldots}(i\omega,b_3,b_3)\right]^{-1}. \tag{4.26}$$

The Green's function $g_{b_2,b_3,...}$ and $g_{b_3,b_4,...}$ are defined analogous to (4.20). For the other bath sites with site index > 2, analogous expressions can be derived.
Up to this point we did not make any assumptions about the form of the bath dispersion ϵ_k. The above expressions can be simplified, if we choose the bath parameters of the Hamiltonian (4.16) in the form

$$\epsilon_n = 0, \quad t_n = t \quad \text{for all } n. \tag{4.27}$$

In this case one has $g_{b_1,b_2,...} = g_{b_2,b_3,...} = ... \equiv g_B$, and from (4.19) one gets the following relation for $g_B(i\omega) \equiv g_B(i\omega, b_1, b_1)$

$$g_B(i\omega) = \left[i\omega + \mu - t^2 g_B(i\omega)\right]^{-1}. \tag{4.28}$$

This equation can be used to derive an explicit expression for $g_B(i\omega)$,

$$g_B(i\omega) = \frac{1}{2t^2}\left(i\omega + \mu - i\mathrm{sgn}(\omega)\sqrt{4t^2 - (i\omega+\mu)^2}\right). \tag{4.29}$$

The retarded Green's function on the first bath site is given by

$$\begin{aligned} g_B\left(\omega + i0^+\right) =& \frac{1}{2t^2}\Big(\omega + \mu - i\sqrt{4t^2 - (\omega+\mu)^2}\Theta\left(2t - |\omega+\mu|\right) \\ & - \sqrt{(\omega+\mu)^2 - 4t^2}\Theta\left(|\omega+\mu| - 2t\right)\mathrm{sgn}(\omega+\mu)\Big). \end{aligned} \tag{4.30}$$

The density of states on the first bath site is then semi-elliptic

$$\begin{aligned} \rho_B(\omega) &= -\frac{1}{\pi}\mathrm{Im}\ g_B\left(\omega + i0^+\right) \\ &= \frac{1}{2\pi t^2}\sqrt{4t^2 - (\omega+\mu)^2}\Theta\left(2t - |\omega+\mu|\right), \end{aligned} \tag{4.31}$$

with bandwidth $W = 4t$. As a measure for the hybridization strength we define the quantity

$$\Delta_0 = \pi v^2 \rho_B(-\mu) = \frac{v^2}{t}. \tag{4.32}$$

4.2 Effective theory for the bath

4.2.1 Integrating out the core

We now separate the system into two parts as illustrated in Fig. 4.2. One part (called "core" in the following) contains the correlated site and the first L bath sites of the noninteracting tight binding chain ($L = 0, 1, 2, 3$). The other part (called "bath") contains all bath sites of the tight binding chain with index $n \geq L+1$. In the following we integrate

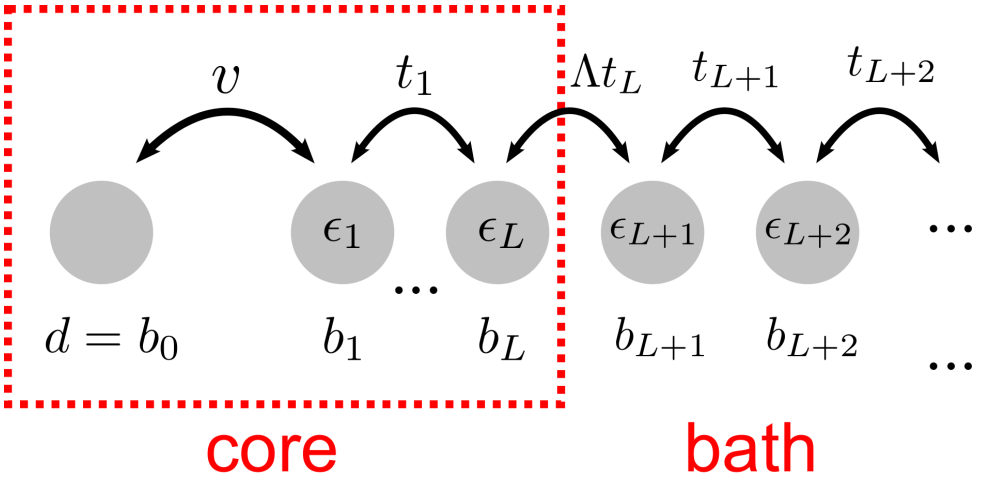

Figure 4.2: The semi-infinite tight binding chain is separated into two parts: The core includes the correlated site and the first L bath sites and the bath consists of the remaining bath sites. The two parts are coupled by a hopping term which is proportional to the parameter Λ.

out the core in a functional integral representation of our model, leading to an effective theory for the bath[1].
Our model is described by the grandcanonical partition function

$$\mathcal{Z} = \int \mathcal{D}\left[\bar{b}, b\right] \ \exp\left[-S\left[\bar{b}, b\right]\right] \tag{4.33}$$

with the action

$$\begin{aligned} S\left[\bar{b}, b\right] =& S_{\text{core}}\left[\bar{b}_0, b_0, \bar{b}_1, b_1, ..., \bar{b}_L, b_L\right] + S_{\text{bath}}\left[\bar{b}_{L+1}, b_{L+1}, \bar{b}_{L+2}, b_{L+2}, ...\right] \\ &+ S^{\Lambda}_{\text{coupling}}\left[\bar{b}_L, b_L, \bar{b}_{L+1}, b_{L+1}\right] . \end{aligned} \tag{4.34}$$

To make the notation more compact, we denote the dot site d as the 0th bath site b_0 and set $t_0 \equiv v$ and $\epsilon_0 \equiv \epsilon_{d,\sigma}$. S_{core} and S_{bath} are given by

$$\begin{aligned} S_{\text{core}}\left[\bar{b}_0, b_0, \bar{b}_1, b_1, ..., \bar{b}_L, b_L\right] =& \sum_{n=0}^{L} \left(\bar{b}_n, \left(\partial_\tau + \epsilon_n - \mu\right) b_n\right) - \sum_{n=0}^{L-1} \left[t_n \left(\bar{b}_n, b_{n+1}\right) + H.c.\right] \\ &+ U \int_0^\beta d\tau \ n_\uparrow(\tau)\, n_\downarrow(\tau) , \end{aligned} \tag{4.35}$$

$$S_{\text{bath}}\left[\bar{b}_{L+1}, b_{L+1}, \bar{b}_{L+2}, b_{L+2}, ...\right] = \sum_{n=L+1}^{\infty} \left(\bar{b}_n, \left(\partial_\tau + \epsilon_n - \mu\right) b_n\right) - \sum_{n=L+1}^{\infty} \left[t_n \left(\bar{b}_n, b_{n+1}\right) + H.c.\right] ,$$

[1] The idea of integrating out the correlated site to reduce the Anderson model to an effective bath theory is for the case $L = 0$ worked out in Ref. [Joe10]. In this work analytic results that are perturbative in the effective bath interaction as well as fRG results are presented. These served as benchmark to our numerical results.

where we introduced $n_\sigma(\tau) = \bar{b}_{0,\sigma}(\tau) b_{0,\sigma}(\tau)$. The coupling between the core and the bath is descibed by

$$S^{\Lambda}_{\text{coupling}}\left[\bar{b}_L, b_L, \bar{b}_{L+1}, b_{L+1}\right] = -\Lambda\left[t_L\left(\bar{b}_L, b_{L+1}\right) + H.c.\right]. \tag{4.36}$$

We introduced the flow parameter Λ. The original model (4.1) corresponds to $\Lambda = 1$, and for $\Lambda = 0$ core and bath are decoupled.
With the definition of the $(L+1)$-component fields

$$c = (b_0, b_1, b_2, ..., b_L), \tag{4.37}$$

$$\chi = (0, 0, ..., t_L b_{L+1}) \tag{4.38}$$

we can rewrite the action (4.34) as

$$S = S_{\text{core}}[\bar{c}, c] + S_{\text{bath}}\left[\bar{b}_{L+1}, b_{L+1}, \bar{b}_{L+2}, b_{L+2}, ...\right] - \sum_{n=0}^{L}(\bar{c}_n, \Lambda\chi_n) - H.c. \tag{4.39}$$

Now we can formally integrate out the c-fields,

$$\int \mathcal{D}[\bar{c}, c] \exp\left[-S_{\text{core}}[\bar{c}, c] + \sum_{n=0}^{L}(\bar{c}_n, \Lambda\chi_n) + H.c.\right] = \mathcal{Z}_{\text{core}} \exp\left[\mathcal{W}_{\text{core}}[\Lambda\bar{\chi}, \Lambda\chi]\right]. \tag{4.40}$$

$\mathcal{Z}_{\text{core}}$ is the partition function of the core problem given by

$$\mathcal{Z}_{\text{core}} = \int \mathcal{D}[\bar{c}, c] \ \exp\left[-S_{\text{core}}[\bar{c}, c]\right]. \tag{4.41}$$

and $\mathcal{W}_{\text{core}}$ is the generating functional for the connected core Green's functions. This yields an effective action for the bath

$$\begin{aligned}\mathcal{Z} &= \int \mathcal{D}\left[\bar{c}, c, \bar{b}_{L+1}, b_{L+1}, ...\right] \exp\left[-S_{\text{core}}[\bar{c}, c] + \sum_{n=0}^{L}(\bar{c}_n, \Lambda\chi_n) + H.c. - S_{\text{bath}}\left[\bar{b}_{L+1}, b_{L+1}, ...\right]\right] \\ &\propto \int \mathcal{D}\left[\bar{b}_{L+1}, b_{L+1}, \bar{b}_{L+2}, b_{L+2}, ...\right] \exp\left[-S^{\text{eff}}_{\text{bath}}\left[\bar{b}_{L+1}, b_{L+1}, \bar{b}_{L+2}, b_{L+2}, ...\right]\right].\end{aligned}$$

When we expand $\mathcal{W}_{\text{core}}(\Lambda\bar{\chi}, \Lambda\chi)$ in the $\bar{\chi}, \chi$-fields, the effective action has the following form

$$\begin{aligned}&S^{\text{eff}}_{\text{bath}}\left[\bar{b}_{L+1}, b_{L+1}, \bar{b}_{L+2}, b_{L+2}, ...\right] \\ =&S_{\text{bath}}\left[\bar{b}_{L+1}, b_{L+1}, \bar{b}_{L+2}, b_{L+2}, ...\right] - \mathcal{W}_{\text{core}}[\Lambda\bar{\chi}, \Lambda\chi] \\ =&S_{\text{bath}}\left[\bar{b}_{L+1}, b_{L+1}, \bar{b}_{L+2}, b_{L+2}, ...\right] - \sum_{n=0}^{\infty}\frac{(-1)^n\Lambda^{2n}}{n!^2}\sum_{\substack{i_1,...,i_n \\ i'_1,...,i'_n}}\int_0^\beta \mathrm{d}\tau_1...\mathrm{d}\tau_n\mathrm{d}\tau'_1...\mathrm{d}\tau'_n \\ &\times\mathcal{G}^{c,(n)}_{\text{core}}(i_1, \tau_1; ...; i_n, \tau_n | i'_1, \tau_1; , ...; i'_n, \tau'_n)\, \bar{\chi}_{i_1}(\tau_1)...\bar{\chi}_{i_n}(\tau_n)\chi_{i'_n}(\tau'_n)...\chi_{i'_1}(\tau'_1).\end{aligned}$$

In the following we neglect the term with $n = 0$, which does not contain any fields. Furthermore, we truncate the sum over n after $n = 2$. This means we consider only the first and second order of the expansion and neglect all correlation-functions $\mathcal{G}^{c,(\geq 3)}_{\text{core}}$.
In Matsubara space we get

$$
\begin{aligned}
&S^{\text{eff}}_{\text{bath}}\left[\bar{b}_{L+1}, b_{L+1}, \bar{b}_{L+2}, b_{L+2}, ...\right] \\
=&S_{\text{bath}}\left[\bar{b}_{L+1}, b_{L+1}, \bar{b}_{L+2}, b_{L+2}, ...\right] + \frac{\Lambda^2}{\beta}\sum_{i\omega}\sum_{i_1,i_1'}\bar{\chi}_{i1}(i\omega)\mathcal{G}^{c,(1)}_{\text{core}}\left(i\omega, i_1, i_1'\right)\chi_{i_1'}(i\omega) \\
&-\frac{\Lambda^4}{4\beta^3}\sum_{\substack{i\omega_1,i\omega_2,\\ i\omega_1',i\omega_2'}}\sum_{\substack{i_1,i_2,\\ i_1',i_2'}}\bar{\chi}_{i_1}(i\omega_1)\bar{\chi}_{i_2}(i\omega_2)\mathcal{G}^{c,(2)}_{core}\left(i\omega_1, i_1; i\omega_2, i_2 | i\omega_1', i_1'; i\omega_2', i_2'\right) \\
&\times\chi_{i_1'}(i\omega_1')\chi_{i_2'}(i\omega_2')\delta_{\omega_1+\omega_2,\omega_1'+\omega_2'} \\
=&S_{\text{bath}}\left[\bar{b}_{L+1}, b_{L+1}, \bar{b}_{L+2}, b_{L+2}, ...\right] + \frac{(\Lambda|t_L|)^2}{\beta}\sum_{i\omega}\sum_{\sigma}\bar{b}_{L+1,\sigma}(i\omega)\mathcal{G}^{c,(1)}_{\text{core},\sigma}\left(i\omega, b_L, b_L\right)b_{L+1,\sigma}(i\omega) \\
&-\frac{(\Lambda|t_L|)^4}{4\beta^3}\sum_{\substack{i\omega_1,i\omega_2,\\ i\omega_1',i\omega_2'}}\sum_{\substack{\sigma_1,\sigma_2,\\ \sigma_1',\sigma_2'}}\bar{b}_{L+1,\sigma_1}(i\omega_1)\bar{b}_{L+1,\sigma_2}(i\omega_2) \\
&\times\mathcal{G}^{c,(2)}_{\text{core}}\left(i\omega_1, b_L, \sigma_1; i\omega_2, b_L, \sigma_2 | i\omega_1', b_L, \sigma_1'; i\omega_2', b_L, \sigma_2'\right) \\
&\times b_{L+1,\sigma_1'}(i\omega_1')b_{L+1,\sigma_2'}(i\omega_2')\delta_{\omega_1+\omega_2,\omega_1'+\omega_2'}\delta_{\sigma_1+\sigma_2,\sigma_1'+\sigma_2'}\,.
\end{aligned}
$$

In the effective bath theory there is a local interaction on bath site $L+1$. The other bath sites ($L+2$,$L+3$,...) remain noninteracting and can be integrated out. This leads to the local effective action

$$
\begin{aligned}
S^{\text{eff}}_{\text{bath}}\left[\bar{b}_{L+1}, b_{L+1}\right] =& -\frac{1}{\beta}\sum_{i\omega}\sum_{\sigma}\bar{b}_{L+1,\sigma}(i\omega)Q^{\text{eff},\Lambda}_{\sigma}\left(i\omega\right)b_{L+1,\sigma}\left(i\omega\right) \\
&-\frac{(\Lambda|t_L|)^4}{4\beta^3}\sum_{\substack{i\omega_1,i\omega_2,\\ i\omega_1',i\omega_2'}}\sum_{\substack{\sigma_1,\sigma_2,\\ \sigma_1',\sigma_2'}}\bar{b}_{L+1,\sigma_1}(i\omega_1)\bar{b}_{L+1,\sigma_2}(i\omega_2) \\
&\times\mathcal{G}^{c,(2)}_{\text{core}}\left(i\omega_1, b_L, \sigma_1; i\omega_2, b_L, \sigma_2 | i\omega_1', b_L, \sigma_1'; i\omega_2', b_L, \sigma_2'\right) \\
&\times b_{L+1,\sigma_1'}(i\omega_1')b_{L+1,\sigma_2'}(i\omega_2')\delta_{\omega_1+\omega_2,\omega_1'+\omega_2'}\delta_{\sigma_1+\sigma_2,\sigma_1'+\sigma_2'}\,. \qquad (4.42)
\end{aligned}
$$

with

$$
Q^{\text{eff},\Lambda}_{\sigma}\left(i\omega\right) = i\omega + \mu - \epsilon_{L+1} - (\Lambda|t_L|)^2\mathcal{G}^{c,(1)}_{\text{core},\sigma}\left(i\omega, b_L, b_L\right) - |t_{L+1}|^2 g_{b_{L+2},b_{L+3},...}\left(i\omega, b_{L+2}, b_{L+2}\right). \qquad (4.43)
$$

The Green's functions $\mathcal{G}^{c,(1)}_{\text{core},\sigma}\left(i\omega, b_L, b_L\right)$ and $\mathcal{G}^{c,(2)}_{\text{core}}\left(i\omega_1, b_L, \sigma_1; i\omega_2, b_L, \sigma_2 | i\omega_1', b_L, \sigma_1'; i\omega_2', b_L, \sigma_2'\right)$ are calculated from the Lehmann representation (2.61) and (2.62). Note that an additional frequency dependent local term, as for example the local self-energy that arise in a DMFT cycle (cf. chapter 6), can be easily included in $Q^{\text{eff},\Lambda}_{\sigma}\left(i\omega\right)$.

4.2.2 Relation to the dot self-energy and the dot two-particle vertex

In the effective theory (4.42) the bath site $L+1$ is now interacting with a frequency dependent term, while in the original theory (4.34) it was noninteracting. The self-energy and all higher irreducible vertex functions are local on the dot site by construction. Nevertheless the local Green's function of the coupled problem on bath site $L+1$ is nontrivial and depends on the dot self-energy, as can be seen in (4.25) or (4.26). This Green's function can also be derived in the setup of the effective theory and one can use the identity $\mathcal{G}^{\Lambda}_{\sigma}(i\omega, b_{L+1}, b_{L+1}) = \mathcal{G}^{\mathrm{eff},\Lambda}_{\sigma}(i\omega, b_{L+1}, b_{L+1})$ with

$$\mathcal{G}^{\mathrm{eff},\Lambda}_{\sigma}(i\omega, b_{L+1}, b_{L+1}) = \left[Q^{\mathrm{eff},\Lambda}_{\sigma}(i\omega) - \Sigma^{\mathrm{eff},\Lambda}_{\sigma}(i\omega)\right]^{-1} \tag{4.44}$$

to get a relation between the dot self-energy and the effective self-energy $\Sigma^{\mathrm{eff},\Lambda}_{\sigma}$ on bath site $L+1$. These relations depend on L and for $L = 0, 1, 2, 3$ we get the relations:

$$L=0: \ \Sigma^{\Lambda}_{\mathrm{dot},\sigma}(i\omega) = i\omega + \mu - \epsilon_{d,\sigma} - \frac{(\Lambda v)^2}{\Sigma^{\mathrm{eff},\Lambda}_{\sigma}(i\omega) + (\Lambda v)^2 \ \mathcal{G}^{c,(1)}_{\mathrm{core},\sigma}(i\omega, b_0, b_0)}, \tag{4.45}$$

$$L=1: \ \Sigma^{\Lambda}_{\mathrm{dot},\sigma}(i\omega) = i\omega + \mu - \epsilon_{d,\sigma} - \frac{v^2}{i\omega + \mu - \epsilon_1 - \frac{(\Lambda|t_1|)^2}{\Sigma^{\mathrm{eff},\Lambda}_{\sigma}(i\omega) + (\Lambda|t_1|)^2 \ \mathcal{G}^{c,(1)}_{\mathrm{core},\sigma}(i\omega, b_1, b_1)}}, \tag{4.46}$$

$$L=2: \ \Sigma^{\Lambda}_{\mathrm{dot},\sigma}(i\omega) = i\omega + \mu - \epsilon_{d,\sigma} - \frac{v^2}{i\omega + \mu - \epsilon_1 - \frac{|t_1|^2}{i\omega+\mu-\epsilon_2 - \frac{(\Lambda|t_2|)^2}{\Sigma^{\mathrm{eff},\Lambda}_{\sigma}(i\omega) + (\Lambda|t_2|)^2 \ \mathcal{G}^{c,(1)}_{\mathrm{core},\sigma}(i\omega, b_2, b_2)}}}, \tag{4.47}$$

$$L=3: \ \Sigma^{\Lambda}_{\mathrm{dot},\sigma}(i\omega) = i\omega + \mu - \epsilon_{d,\sigma} - \frac{v^2}{i\omega + \mu - \epsilon_1 - \frac{|t_1|^2}{i\omega+\mu-\epsilon_2 - \frac{|t_2|^2}{i\omega+\mu-\epsilon_3 - \frac{(\Lambda|t_3|)^2}{\Sigma^{\mathrm{eff},\Lambda}_{\sigma}(i\omega) + (\Lambda|t_3|)^2 \mathcal{G}^{c,(1)}_{\mathrm{core},\sigma}(i\omega, b_3, b_3)}}}}}. \tag{4.48}$$

In a similar way one gets the local 1PI vertex function on the dot site from the vertex function of the effective bath theory $\gamma^{(2),\mathrm{eff},\Lambda=1} \equiv \gamma^{(2),\mathrm{eff}}$. The connected two-particle Green's function on site b_{L+1} is given by

$$\begin{aligned}
&\mathcal{G}^{c,(2)}(i\omega_1, b_{L+1}, \sigma_1; i\omega_2, b_{L+1}, \sigma_2 | i\omega_{1'}, b_{L+1}, \sigma_{1'}; i\omega_{2'}, b_{L+1}, \sigma_{2'}) \\
&= -\prod_{k=1}^{2} \mathcal{G}(i\omega_k, b_{L+1}, b_{L+1}) \gamma^{(2),\mathrm{eff}}(i\omega_1, b_{L+1}, \sigma_1; i\omega_2, b_{L+1}, \sigma_2 | i\omega_{1'}, b_{L+1}, \sigma_{1'}; i\omega_{2'}, b_{L+1}, \sigma_{2'}) \\
&\quad \times \prod_{k=1}^{2} \mathcal{G}(i\omega_{k'}, b_{L+1}, b_{L+1}).
\end{aligned} \tag{4.49}$$

By amputing the Green's function that connect the dot site with site b_{L+1} one gets the vertex function on the dot site

$$\begin{aligned}
&\gamma^{(2)}_{\mathrm{dot}}\left(i\omega_1, d, \sigma_1; i\omega_2, d, \sigma_2 | i\omega_{1'}, d, \sigma_{1'}; i\omega_{2'}, d, \sigma_{2'}\right) \\
=& -\prod_{k=1}^{2}\left[\mathcal{G}(i\omega_k, b_{L+1}, d)\right]^{-1} \mathcal{G}^{\mathrm{c},(2)}\left(i\omega_1, b_{L+1}, \sigma_1; i\omega_2, b_{L+1}, \sigma_2 | i\omega_{1'}, b_{L+1}, \sigma_{1'}; i\omega_{2'}, b_{L+1}, \sigma_{2'}\right) \\
&\times \prod_{k=1}^{2}\left[\mathcal{G}(i\omega_{k'}, d, b_{L+1})\right]^{-1}. \qquad (4.50)
\end{aligned}$$

4.3 Hybridization flow equations

The effective action in Eq. (4.42) reduces to a noninteracting model for $\Lambda = 0$, because the interaction term is proportional to Λ^4. This represents a simple starting point for a fRG flow in Λ, similar to the interaction flow scheme introduced in [HRAE04]. In order to use the fRG formalism for the 1PI vertices, the flow parameter Λ should only occur in the quadratic part of the action (cf. chapter 3.1). This can be achieved for any $\Lambda \neq 0$ by rescaling the fields $b_{L+1} \to b_{L+1}/\Lambda$ and $\bar{b}_{L+1} \to \bar{b}_{L+1}/\Lambda$. This leads to the quadratic part of the effective action,

$$S^{\mathrm{eff},0}_{\mathrm{bath}}\left[\bar{b}_{L+1}, b_{L+1}\right] = -\frac{1}{\beta}\sum_{i\omega}\sum_{\sigma}\bar{b}_{L+1,\sigma}(i\omega)\tilde{Q}^{\mathrm{eff},\Lambda}_{\sigma}\left(i\omega\right) b_{L+1,\sigma}\left(i\omega\right).$$

with

$$\begin{aligned}
\tilde{Q}^{\mathrm{eff},\Lambda}_{\sigma}\left(i\omega\right) &= \frac{1}{\Lambda^2} Q^{\mathrm{eff},\Lambda}_{\sigma}\left(i\omega\right) \\
&= \frac{i\omega + \mu - \epsilon_{L+1}}{\Lambda^2} - |t_L|^2 \mathcal{G}^{c,(1)}_{\mathrm{core},\sigma}\left(i\omega, b_L, b_L\right) - \frac{|t_{L+1}|^2}{\Lambda^2} g_{b_{L+2}, b_{L+3}, \ldots}\left(i\omega, b_{L+2}, b_{L+2}\right), \qquad (4.51)
\end{aligned}$$

and a quartic part which does not depend on Λ anymore. We denote rescaled operators by a tilde. Note that the rescaling changes correlation functions of different order in the fields differently, but in the end we will study the case $\Lambda = 1$.
The single scale propagator (3.11) follows as

$$\begin{aligned}
\tilde{S}^{\mathrm{eff},\Lambda}_{\sigma}(i\omega) &= \tilde{\mathcal{G}}^{\mathrm{eff},\Lambda}_{\sigma}(i\omega, b_{L+1}, b_{L+1}) \tfrac{\mathrm{d}}{\mathrm{d}\Lambda}\left[\tilde{Q}^{\mathrm{eff},\Lambda}_{\sigma}\left(i\omega\right)\right] \tilde{\mathcal{G}}^{\mathrm{eff},\Lambda}_{\sigma}(i\omega, b_{L+1}, b_{L+1}) \\
&= \frac{-2\Lambda\left[i\omega + \mu - \epsilon_{L+1} - |t_{L+1}|^2 g_{b_{L+2}, b_{L+3}, \ldots}(i\omega, b_{L+2}, b_{L+2})\right]}{\left[i\omega + \mu - \epsilon_{L+1} - (\Lambda|t_L|)^2 \mathcal{G}^{c,(1)}_{\mathrm{core},\sigma}(i\omega, b_L, b_L) - |t_{L+1}|^2 g_{b_{L+2}, b_{L+3}, \ldots}(i\omega, b_{L+2}, b_{L+2}) - \Lambda^2 \tilde{\Sigma}^{\mathrm{eff},\Lambda}_{\sigma}(i\omega)\right]^2}. \qquad (4.52)
\end{aligned}$$

In the following we present the flow equations for the SU(2) symmetric case. Using the spin conservation, the two-particle vertex can be parameterized in analogy to (2.51) as

$$\begin{aligned}
&\tilde{\gamma}^{(2),\mathrm{eff},\Lambda}\left(i\omega_1, b_{L+1}, \sigma_1; i\omega_2, b_{L+1}, \sigma_2 | i\omega_{1'}, b_{L+1}, \sigma_{1'}; i\omega_{2'}, b_{L+1}, \sigma_{2'}\right) \\
=& \tilde{V}^{\mathrm{eff},\Lambda}(i\omega_1; i\omega_2 | i\omega_{1'}, i\omega_{2'}) \delta_{\sigma_1,\sigma_{1'}} \delta_{\sigma_2,\sigma_{2'}} - \bar{\tilde{V}}^{\mathrm{eff},\Lambda}(i\omega_1; i\omega_2 | i\omega_{1'}, i\omega_{2'}) \delta_{\sigma_1,\sigma_{2'}} \delta_{\sigma_2,\sigma_{1'}}. \qquad (4.53)
\end{aligned}$$

From the antisymmetry of $\tilde{\gamma}^{(2),\mathrm{eff},\Lambda}(1,2|1',2')$ under the permutations $1' \leftrightarrow 2'$ and $1 \leftrightarrow 2$, it follows that the functions $\tilde{V}^{\mathrm{eff},\Lambda}$ and $\bar{\tilde{V}}^{\mathrm{eff},\Lambda}$ are related by

$$\tilde{V}^{\mathrm{eff},\Lambda}(i\omega_1, i\omega_2|i\omega_{1'}, i\omega_{2'}) = \bar{\tilde{V}}^{\mathrm{eff},\Lambda}(i\omega_2, i\omega_1|i\omega_{1'}, i\omega_{2'}) = \bar{\tilde{V}}^{\mathrm{eff},\Lambda}(i\omega_1, i\omega_2|i\omega_{2'}, i\omega_{1'}). \quad (4.54)$$

Using this parametrization we get the flow equation

$$\frac{d}{d\Lambda}\tilde{\Sigma}^{\mathrm{eff},\Lambda}(i\omega) = -\frac{1}{\beta}\sum_{i\omega'} \tilde{S}^{\mathrm{eff},\Lambda}(i\omega')\left[2\tilde{V}^{\mathrm{eff},\Lambda}(i\omega, i\omega'|i\omega) - \tilde{V}^{\mathrm{eff},\Lambda}(i\omega, i\omega'|i\omega')\right] \quad (4.55)$$

$$\frac{d}{d\Lambda}\tilde{V}^{\mathrm{eff},\Lambda}(i\omega_1, i\omega_2|i\omega_{1'}) = \mathcal{T}^{\Lambda}_{\mathrm{pp}}(i\omega_1, i\omega_2|i\omega_{1'}) + \mathcal{T}^{\Lambda}_{\mathrm{dph}}(i\omega_1, i\omega_2|i\omega_{1'}) + \mathcal{T}^{\Lambda}_{\mathrm{crph}}(i\omega_1, i\omega_2|i\omega_{1'}) \quad (4.56)$$

with

$$\begin{aligned}
\mathcal{T}^{\Lambda}_{\mathrm{pp}}(i\omega_1, i\omega_2|i\omega_{1'}) =& \frac{1}{\beta}\sum_{i\omega_3} L^{\Lambda}(i\omega_3, i\omega_1 + i\omega_2 - i\omega_3) \quad (4.57)\\
&\times \tilde{V}^{\mathrm{eff},\Lambda}(i\omega_1, i\omega_2|i\omega_3)\tilde{V}^{\mathrm{eff},\Lambda}(i\omega_3, i\omega_1 + i\omega_2 - i\omega_3|i\omega_{1'})\\
\mathcal{T}^{\Lambda}_{\mathrm{dph}}(i\omega_1, i\omega_2|i\omega_1') =& \frac{1}{\beta}\sum_{i\omega_3} L^{\Lambda}(i\omega_3, i\omega_1 - i\omega_{1'} + i\omega_3) \quad (4.58)\\
&\times \big[-2\tilde{V}^{\mathrm{eff},\Lambda}(i\omega_1, i\omega_3|i\omega_{1'})\tilde{V}^{\mathrm{eff},\Lambda}(i\omega_1 - i\omega_{1'} + i\omega_3, i\omega_2|i\omega_3)\\
&+ \tilde{V}^{\mathrm{eff},\Lambda}(i\omega_3, i\omega_1|i\omega_{1'})\tilde{V}^{\mathrm{eff},\Lambda}(i\omega_1 - i\omega_{1'} + i\omega_3, i\omega_2|i\omega_3)\\
&+ \tilde{V}^{\mathrm{eff},\Lambda}(i\omega_1, i\omega_3|i\omega_{1'})\tilde{V}^{\mathrm{eff},\Lambda}(i\omega_2, i\omega_1 - i\omega_{1'} + i\omega_3|i\omega_3)\big]\\
\mathcal{T}^{\Lambda}_{\mathrm{crph}}(i\omega_1, i\omega_2|i\omega_{1'}) =& \frac{1}{\beta}\sum_{i\omega_3} L^{\Lambda}(i\omega_3, i\omega_2 - i\omega_{1'} + i\omega_3) \quad (4.59)\\
&\times \tilde{V}^{\mathrm{eff},\Lambda}(i\omega_3, i\omega_2|i\omega_{1'})\tilde{V}^{\mathrm{eff},\Lambda}(i\omega_1, i\omega_2 - i\omega_{1'} + i\omega_3|i\omega_3).
\end{aligned}$$

Here L^{Λ} is given by

$$L^{\Lambda}(i\omega_1, i\omega_2) = \tilde{\mathcal{G}}^{\mathrm{eff},\Lambda}(i\omega_1)\tilde{S}^{\mathrm{eff},\Lambda}(i\omega_2) + \tilde{S}^{\mathrm{eff},\Lambda}(i\omega_1)\tilde{\mathcal{G}}^{\mathrm{eff},\Lambda}(i\omega_2). \quad (4.60)$$

The initial conditions of the flow equations follow from (3.12) - (3.14) as

$$\tilde{\Sigma}^{\mathrm{eff},\Lambda=0}_{\sigma}(i\omega) = 0, \quad (4.61)$$

$$\tilde{V}^{\mathrm{eff},\Lambda=0}(i\omega_1, i\omega_2|i\omega_{1'}, i\omega_{2'}) = |t_L|^4 \mathcal{G}^{c,(2)}_{\mathrm{core}}(i\omega_1, b_L, \uparrow; i\omega_2, b_L, \downarrow | i\omega_{1'}, b_L, \uparrow; i\omega_{2'}, b_L, \downarrow). \quad (4.62)$$

The bare interaction of the effective theory is given by a connected two-particle Green's function and is therefore strongly frequency dependent. Due to its suppression at large frequencies (cf. Fig. 4.3), we can restrict the frequency grid to the first N positive frequencies. Typically we took $N = 100$ at $\beta = 30/\Delta_0$. Note that for a constant frequency independent interaction a larger grid is needed to obtain converged results (cf. Ref. [IRB+10]). The flow equations can then be integrated by using standard DEQ-solvers.

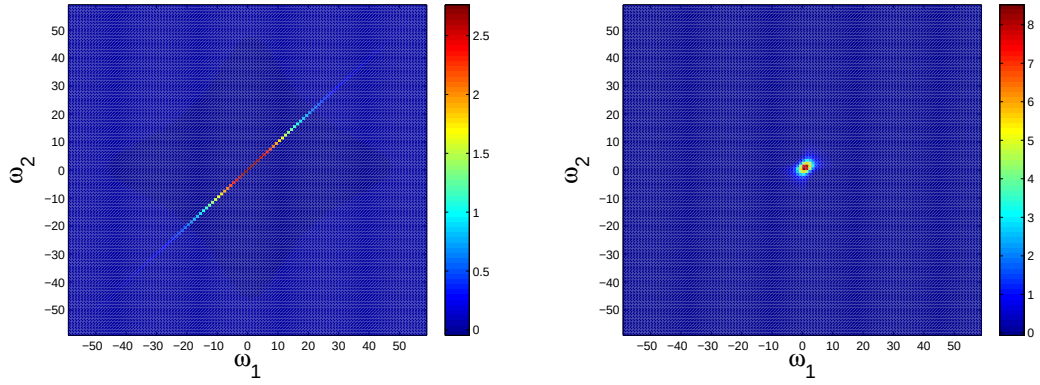

Figure 4.3: Density part of the connected Green's function $\mathcal{G}_d^{(2),c}(i\omega_1, b_L; i\omega_2, b_L | i\omega_1, b_L; i\omega_2, b_L)$ (real part) for $U = 8\Delta_0$, $\beta = 30/\Delta_0$ (Left: $L = 0$, Right: $L = 1$), which appears in the integral kernel on the right hand side of the flow equation for the self-energy of the effective bath theory (4.55). Note the suppression of the interaction at high frequencies.

4.4 Flow equation for the dot self-energy

Instead of doing the fRG flow in the effective bath theory (4.51), one could also derive flow equations directly for the dot self-energy and the two-particle 1PI vertex function on the dot site with the core 1PI vertex functions as initial condition. For $L > 0$ these flow equations have a more complicated structure, and in our case the expressions are more compact. In the following we derive the flow equation for $L = 0$ and approximation 1, and discuss its relation to the flow equation for $\tilde{\Sigma}^{\text{eff},\Lambda}$.

For the particle-hole symmetric case the Λ-dependent inverse free propagator on the dot site is given by[1]

$$Q^\Lambda(i\omega) = i\omega + \frac{U}{2} - \Lambda^2 \Delta(i\omega) \tag{4.63}$$

with the hybridization function (4.22). The full Green's function is then $\mathcal{G}^\Lambda(i\omega, d, d) = \left[Q^\Lambda(i\omega) - \Sigma^\Lambda_{\text{dot}}(i\omega)\right]^{-1}$ and the single scale propagator comes out as

$$\begin{aligned} S^\Lambda_{\text{dot}}(i\omega) &= \mathcal{G}^\Lambda(i\omega, d, d) \frac{\mathrm{d}}{\mathrm{d}\Lambda} \left[Q^\Lambda(i\omega)\right] \mathcal{G}^\Lambda(i\omega, d, d) \\ &= \frac{-2\Lambda v^2 g_{b_1, b_2, \ldots}(i\omega, b_1, b_1)}{\left[i\omega + \frac{U}{2} - \Sigma^\Lambda_{\text{dot}}(i\omega) - (\Lambda v)^2 g_{b_1, b_2, \ldots}(i\omega, b_1, b_1)\right]^2}. \end{aligned} \tag{4.64}$$

In approximation 1 the flow equation for the self-energy on the dot site is then given by

$$\frac{\mathrm{d}}{\mathrm{d}\Lambda} \Sigma^\Lambda_{\text{dot}}(i\omega) = -\frac{1}{\beta} \sum_{i\omega'} S^\Lambda_{\text{dot}}(i\omega') \left[2\gamma^{(2)}_{\text{dot}}(i\omega, \uparrow; i\omega', \downarrow | i\omega, \uparrow; \downarrow) - \gamma^{(2)}_{\text{dot}}(i\omega, \uparrow; i\omega', \downarrow | i\omega', \uparrow; \downarrow)\right] \tag{4.65}$$

[1] In the following we skip the spin-index.

with the initial condition (cf. appendix B.1 , Eq. (B.3))

$$\Sigma_{\mathrm{dot}}^{\Lambda=0}(i\omega) = \frac{U}{2} + \frac{U^2}{4i\omega}. \tag{4.66}$$

$\gamma_{\mathrm{dot}}^{(2)}$ is the 1PI vertex function of the isolated Hubbard site, explicitly written out in Eq. (B.4). Eq. (4.65) can be related to the flow equation for the rescaled effective bath self-energy $\tilde{\Sigma}^{\mathrm{eff},\Lambda}(i\omega) = \frac{1}{\Lambda^2}\Sigma^{\mathrm{eff},\Lambda}(i\omega)$. Therefore we write the single scale propagator (4.52) with Eq. (4.45) as

$$\begin{aligned}\tilde{S}^{\mathrm{eff},\Lambda}(i\omega) &= \frac{-2\Lambda g_{b_1,b_2,\ldots}(i\omega,b_1,b_1)\left[i\omega+\frac{U}{2}-\Sigma_{\mathrm{dot}}^{\Lambda}(i\omega)\right]^2}{\left[i\omega+\frac{U}{2}-\Sigma_{\mathrm{dot}}^{\Lambda}(i\omega)-(\Lambda v)^2 g_{b_1,b_2,\ldots}(i\omega,b_1,b_1)\right]^2} \\ &= \frac{1}{v^2}\left[i\omega+\frac{U}{2}-\Sigma_{\mathrm{dot}}^{\Lambda}(i\omega)\right]^2 S_{\mathrm{dot}}^{\Lambda}(i\omega).\end{aligned} \tag{4.67}$$

The derivation of $\Sigma_{\mathrm{dot}}^{\Lambda}$ with respect to Λ is given by

$$\begin{aligned}\frac{\mathrm{d}}{\mathrm{d}\Lambda}\Sigma_{\mathrm{dot}}^{\Lambda}(i\omega) &= v^2\left[\tilde{\Sigma}^{\mathrm{eff},\Lambda}(i\omega)+v^2\mathcal{G}_{\mathrm{core}}^{c,(1)}(i\omega,b_0,b_0)\right]^{-2}\frac{\mathrm{d}}{\mathrm{d}\Lambda}\tilde{\Sigma}^{\mathrm{eff},\Lambda}(i\omega) \\ &= \frac{1}{v^2}\left[i\omega+\frac{U}{2}-\Sigma_{\mathrm{dot}}^{\Lambda}(i\omega)\right]^2\frac{\mathrm{d}}{\mathrm{d}\Lambda}\tilde{\Sigma}^{\mathrm{eff},\Lambda}(i\omega).\end{aligned} \tag{4.68}$$

We express the derivative $\frac{\mathrm{d}}{\mathrm{d}\Lambda}\tilde{\Sigma}^{\mathrm{eff},\Lambda}(i\omega)$ by the flow equation (4.55) in approximation 1,

$$\frac{\mathrm{d}}{\mathrm{d}\Lambda}\tilde{\Sigma}^{\mathrm{eff},\Lambda}(i\omega) = -\frac{v^4}{\beta}\sum_{i\omega'}\tilde{S}^{\mathrm{eff},\Lambda}(i\omega')\left[2\mathcal{G}_{\mathrm{dot}}^{c,(2)}(i\omega,\uparrow;i\omega',\downarrow|i\omega,\uparrow;\downarrow)-\mathcal{G}_{\mathrm{dot}}^{c,(2)}(i\omega,\uparrow;i\omega',\downarrow|i\omega',\uparrow;\downarrow)\right]. \tag{4.69}$$

Inserting (4.67) and (4.69) into (4.68) leads to

$$\begin{aligned}\frac{\mathrm{d}}{\mathrm{d}\Lambda}\Sigma_{\mathrm{dot}}^{\Lambda}(i\omega) =& -\frac{1}{\beta}\left[i\omega+\frac{U}{2}-\Sigma_{\mathrm{dot}}^{\Lambda}(i\omega)\right]^2 \\ &\times\sum_{i\omega'}\left[i\omega'+\frac{U}{2}-\Sigma_{\mathrm{dot}}^{\Lambda}(i\omega')\right]^2 S_{\mathrm{dot}}^{\Lambda}(i\omega') \\ &\times\left[2\mathcal{G}_{\mathrm{dot}}^{c,(2)}(i\omega,\uparrow;i\omega',\downarrow|i\omega,\uparrow;\downarrow)-\mathcal{G}_{\mathrm{dot}}^{c,(2)}(i\omega,\uparrow;i\omega',\downarrow|i\omega',\uparrow;\downarrow)\right] \\ =& -\frac{1}{\beta}\left[\frac{i\omega+\frac{U}{2}-\Sigma_{\mathrm{dot}}^{\Lambda}(i\omega)}{i\omega+\frac{U}{2}-\Sigma_{d}^{\Lambda=0}(i\omega)}\right]^2 \\ &\times\sum_{i\omega'}\left[\frac{i\omega'+\frac{U}{2}-\Sigma_{\mathrm{dot}}^{\Lambda}(i\omega')}{i\omega'+\frac{U}{2}-\Sigma_{\mathrm{dot}}^{\Lambda=0}(i\omega')}\right]^2 S_{\mathrm{dot}}^{\Lambda}(i\omega') \\ &\times\left[2\gamma_{\mathrm{dot}}^{(2)}(i\omega,\uparrow;i\omega',\downarrow|i\omega,\uparrow;\downarrow)-\gamma_{\mathrm{dot}}^{(2)}(i\omega,\uparrow;i\omega',\downarrow|i\omega',\uparrow;\downarrow)\right].\end{aligned} \tag{4.70}$$

Compared to the flow equation (4.65), the interaction term is at each leg multiplied by a faktor $\frac{i\omega+\frac{U}{2}-\Sigma_{\mathrm{dot}}^{\Lambda}(i\omega)}{i\omega+\frac{U}{2}-\Sigma_{\mathrm{dot}}^{\Lambda=0}(i\omega)}$. In the beginning of the flow this factor is equal to one, but it will

change especially at low frequencies during the flow, since $\Sigma_{\mathrm{dot}}^{\Lambda=0}$ is diverging at $i\omega = 0$. In section 5.1 we will see that the flow equation (4.70) delivers the better results as the flow equation (4.65), which justifies doing the calculations in the effective bath theory.

Chapter 5

Results for the Single Impurity Anderson Model

In the following we present our results for the Single Impurity Anderson model with different core sizes ($L = 0, 1, 2, 3$). As described in chapter 4.1.2, we choose the hopping terms in the semi-infinite tight binding chain as constant leading to a semi-elliptic density of states (4.31). In most cases we consider particle-hole symmetry, $\epsilon_d = -U/2$. In most studies of the SIAM in the literature one considers a constant density of states and the wide band limit, i.e., W is much larger than all other scales of the problem. Then the physics for the symmetric model mostly depends on the ratio of the interaction strength U and the hybridization scale Δ. Here we keep the ω-dependence of the hybridization function. The hybridization strength (4.32) is given by $\Delta_0 = \frac{v^2}{t}$. We choose for simplicity $v = t$, so that $\Delta_0 = t$. This means that we do not have two independent parameters for bandwidth and hybridization, as it is usual in studies of the SIAM, and the finite bandwidth actually enters the problem. Therefore, our results differ quantitatively from the wide limit, which is common in the literature. We take $\Delta_0 = t$ as reference energy scale in the following.

Parts of this chapter are published in

M. Kinza, J. Ortloff, J. Bauer, and C. Honerkamp. Alternative functional renormalization group approach to the single impurity Anderson model. *Phys. Rev. B*, 87:035111, Jan 2013.

5.1 The case $L = 0$

For $L = 0$ the core is given by an isolated dot site with the Hamiltonian

$$\hat{H}_{\text{core}} = \epsilon_d \sum_\sigma d_\sigma^\dagger d_\sigma + U n_{d,\uparrow} n_{d,\downarrow} \tag{5.1}$$

In this case the core correlation functions can be calculated analytically (cf. appendix B.1), and one can also derive analytical results in the setup of the effective bath theory [Joe10].
The initial self-energy at $\Lambda = 0$ for $\epsilon_d = -U/2$ (i.e. particle-hole symmetry) is given by

$$\Sigma_{\text{dot}}\,(i\omega) = \frac{U}{2} + \frac{U^2}{4i\omega}, \tag{5.2}$$

which is the atomic limit result (B.3). $\Sigma_{\text{dot}}\,(i\omega)$ diverges at $i\omega = 0$. Note that the spectral density on the dot site for $\omega = 0$ is determined by the self-energy via

$$A_{\text{dot}}(\omega = 0) = -\frac{1}{\pi}\text{Im}\ \mathcal{G}(i0^+) = -\frac{1}{\pi\ \text{Im}\Sigma(i0^+)}. \tag{5.3}$$

Equation (5.3) shows that a divergent self-energy (5.2) leads to a vanishing spectral weight at $\omega = 0$. In Fig. 5.1 we show the $i\omega$-dependence of the self-energy at the end of the flow for $\Lambda = 1$ on the dot for $U = 10\Delta_0$, $\beta = 30/\Delta_0$ and $\epsilon_d = -U/2$ computed with the described fRG flow in both approximations 1 and 2. The divergence of the self-energy at $i\omega = 0$ has disappeared, but there is still a discontinuity, which is not cured by the flow. Because of this discontinuity we do not obtain a finite quasi-particle weight (4.12), and hence the flow equations are not able to restore the expected local Fermi liquid properties of the SIAM, if we start with the atomic solution. The height of the unphysical discontinuity becomes however smaller in approximation 2 compared to approximation 1 leading to an increased spectral density $A_{\text{dot}}(\omega = 0)$.
Let us come back to the flow equation for the dot self-energy (4.65). The right hand side of this equation diverges at $i\omega = 0$ at each scale Λ, which follows from the frequency structure of the core 1PI vertex function, given in Eq. (B.4). Therefore the self-energy keeps divergent at $i\omega = 0$ during the flow. This is different in the flow equation of the effective bath theory, which is in approximation 1 equivalent to Eq. (4.70) for the dot self-energy. Here the local vertex (B.4) is at each leg multiplied by a factor $\frac{i\omega + \frac{U}{2} - \Sigma_{\text{dot}}^{\Lambda}(i\omega)}{i\omega + \frac{U}{2} - \Sigma_{\text{dot}}^{\Lambda=0}(i\omega)}$. Due to the divergence of $\Sigma_{\text{dot}}^{\Lambda=0}$ at zero frequency this factor is supressed at small frequencies, which softens the divergence of the vertex and leads to a non-divergent self-energy. In the spectral density derived from a Padé-approximation to our numerical data at half filling (not shown) two slightly broadened atomic limit peaks at $\pm U/2$ appear. As expected from our Matsubara data we find a small portion of spectral weight at $\omega = 0$, but no central Kondo resonance with a Lorentzian shape as in Eq. (4.10) is obtained. Hence

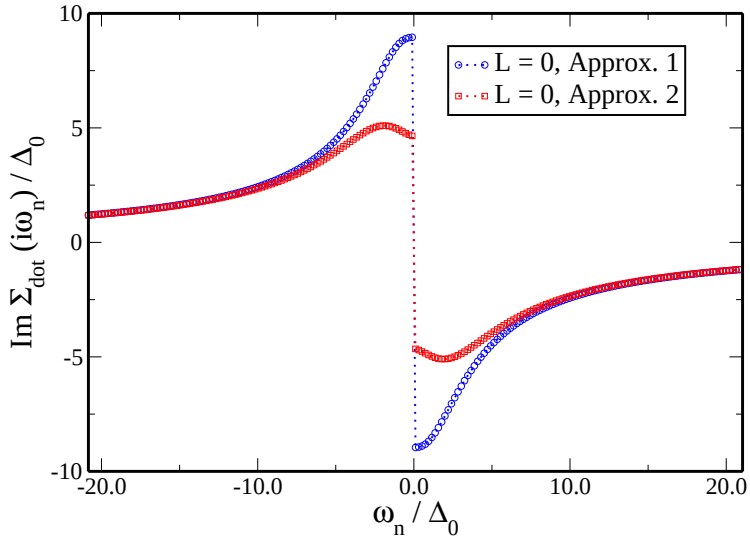

Figure 5.1: Comparison of approximations 1 and 2 to the Matsubara self-energy for $U = 10\Delta_0$, $\beta = 30/\Delta_0$ and $L = 0$. At $i\omega = 0$ one gets a discontinuity of $\mathrm{Im}\Sigma_{\mathrm{dot}}(i\omega_n)$, which is reduced if one increases the level of approximation. The finite step leads to a finite spectral density at $\omega = 0$. However, no coherent quasi-particle, which would require a continuous self-energy at $i\omega = 0$, is observed on this level of the approximation.

the $L = 0$ approximation fails to describe the screening of the local spin $1/2$ moment by the conduction electrons. This screening and singlet formation should develop when Λ is switched on, while at $\Lambda = 0$ the local moment is unscreened. We assume that this strong mismatch is the reason for the non-occurence of the Kondo resonance in this approximation.

Our results are consistent with the findings in Ref. [HJB+09], where a superperturbation approach to the Anderson model is developed. In this approach a finite local cluster containing the correlated dot site is solved exactly. The correlation functions of this cluster then serve as input for an effective theory of so-called dual fermion fields, which are introduced by a Hubbard-Stratonovich decoupling of the original theory. This dual fermion theory is treated by self-consistent perturbation theory and finally one can use exact relations to obtain the original self-energy on the dot site. Like in our setup, no Kondo resonance is observed, when the cluster contains only the correlated bath site.

5.2 The cases $L = 1, 2$ and 3

In the case $L = 1$ the isolated core consists of an interacting site coupled by a hopping term v to a noninteracting bath site.

$$\hat{H}_{\text{core}} = \epsilon_d \sum_\sigma \hat{n}_{d,\sigma} + U\hat{n}_{d,\uparrow}\hat{n}_{d,\downarrow} - v\sum_\sigma \left(d_\sigma^\dagger b_\sigma + H.c.\right) \tag{5.4}$$

This model is still analytically solvable (cf. appendix B.2). The ground state at half filling is a spin singlet state. For $\epsilon_d = -U/2$ and in the limit $v \ll U$ this state is given by

$$|N = 2; S = 0; 1\rangle = \frac{4v}{U}\left(|\uparrow\downarrow, e\rangle + |e, \uparrow\downarrow\rangle\right) - \left(1 - \frac{8v^2}{U^2}\right)\left(|\uparrow, \downarrow\rangle - |\downarrow, \uparrow\rangle\right) \tag{5.5}$$

with energy $\frac{1}{4}\left(-U - \sqrt{U^2 + 64v^2}\right) \overset{v\ll U}{\approx} -\frac{U}{2} - \frac{8v^2}{U}$. The first entry in $|.,.\rangle$ is the correlated site, the second the additional uncorrelated core site. e stands for an empty site. Now, in contrast to the case $L = 0$, the local moment on the dot is already in a singlet state for $\Lambda = 0$. This is a much better starting point to describe features of the Kondo effect. In Fig. 5.2 the Matsubara self-energy calculated in approximation 1 and 2 is shown. In approximation 1 the self-energy is continuous for small frequencies and the derivative $\frac{\mathrm{d}\mathrm{Im}\Sigma_{\text{dot}}(i\omega)}{\mathrm{d}\omega}\Big|_{\omega=0^+}$ is negative, which leads to a central resonance with reduced width $Z\Delta_0$ compared to the non-interacting case. As shown in the inset of Fig. 5.2 we obtain a small step between positive and negative Matsubara frequencies in approximation 2. This step leads to a slight broadening of the central resonance, which decreases with decreasing temperature. Therefore it can be understood as a physically sensible finite temperature effect.

For $L = 2$ the isolated core self-energy has a similar shape as in the $L = 0$ - case and for $\Lambda = 1$ we again get a finite step between positive and negative Matsubara frequencies in both approximations 1 and 2. In its ground state the core carries a finite $s = 1/2$-moment, doublet ground state, in this case which does not become screened when we switch on the coupling to the bath in the fRG flow. This shows once more the importance of choosing a core with singlet ground state for an at least qualitatively correct description of Kondo screening in this setup. The next larger core size with a singlet ground state contains $L = 3$ bath sites. Numerically the calculation of the two-particle vertex function is limited due to the exponential growth of the core Hilbert space (cf. chapter 2.4). We just used approximation 1 in the $L = 3$ case, because here we only need to calculate the vertex for two instead of three independent frequencies.

Let us discuss the numerical results in more detail. The spectrum of the isolated core with $L = 1$ (B.22) consists of four delta-peaks. Two of them are located at $\pm\epsilon_1 = \pm\frac{1}{4}\left(\sqrt{U^2 + 64v^2} + \sqrt{U^2 + 16v^2}\right) \overset{v\ll U}{\approx} \pm\left(\frac{U}{2} + \frac{10v^2}{U}\right)$, which belong to excitations from the ground state (5.5) to the one-particle states $|N = 1; s_z = \sigma; 1\rangle = \frac{2v}{U}|\sigma, e\rangle + \left(1 - \frac{2v^2}{U^2}\right)|e, \sigma\rangle$

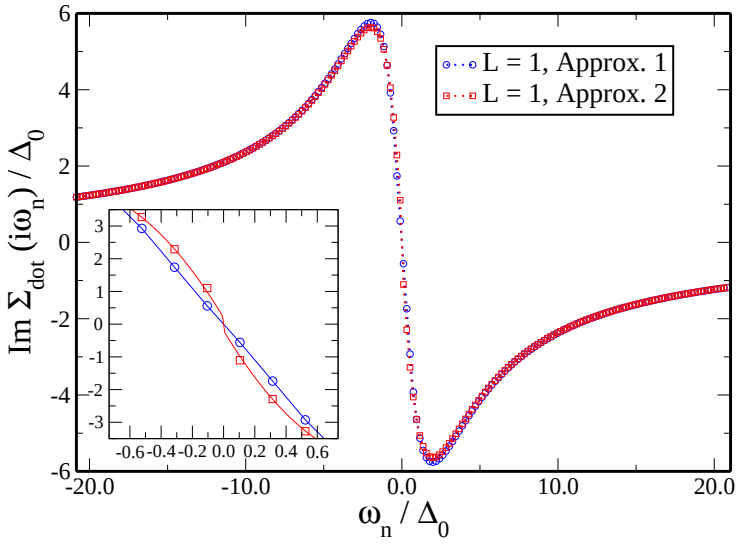

Figure 5.2: Comparison of approximations 1 and 2 to the Matsubara self-energy for $U = 10\Delta_0$, $\beta = 30/\Delta_0$ and $L = 1$. The self-energy is continuous at small frequencies. As shown in the inset one obtains a small step between positive and negative frequencies in approximation 2, which is interpretated as finite temperature effect.

$(v \ll U)$ and their corresponding three-particle states $|N = 3; S = 1/2; S_z = \sigma; 1\rangle$, which are connected by a particle-hole transformation. In the limit $v \to 0$ they are equal to the atomic $\pm U/2$-excitations of the $L = 0$-core. When we switch on the coupling to the bath in the fRG flow, they evolve into hybridization broadened peaks. The other two peaks in the spectrum of the $L = 1$-core lie close to $\omega = 0$ at $\pm\epsilon_2 = \pm\frac{1}{4}\left(\sqrt{U^2 + 64v^2} - \sqrt{U^2 + 16v^2}\right) \overset{v\ll U}{\approx} \pm\frac{6v^2}{U}$. They belong to excitations from the ground state to the one-particle states $|N = 1; s_z = \sigma; 2\rangle = \frac{2v}{U}|\sigma, e\rangle + \left(1 - \frac{2v^2}{U^2}\right)|e, \sigma\rangle \quad (v \ll U)$ and their corresponding three-particle states $|N = 3; S = 1/2; S_z = \sigma; 2\rangle$. The spectral weight of this excitations follows from (B.20) for $v \ll U$ as $2a_1 = \frac{36v^2}{U^2}$. This is in this limit equal to the quasi-particle spectral weight Z, which follows from the self-energy (B.24) as

$$Z = \left[1 - \frac{\mathrm{d}\mathrm{Im}\Sigma_{\mathrm{dot}}(i\omega)}{\mathrm{d}\omega}\bigg|_{\omega=0^+}\right]^{-1} = \frac{1}{1 + \frac{U^2}{36v^2}} \approx \frac{36v^2}{U^2}. \tag{5.6}$$

To obtain the spectral density on the dot site $A_{\mathrm{dot}}(\omega)$ we performed an analytic continuation of our Matsubara data $\mathcal{G}(i\omega_n, d, d) \to \mathcal{G}(\omega + i0^+, d, d)$ to the real frequency axis using a Padé-algorithm (cf. chapter 2.5). It turns out that already in the most simple approximation 1 we get a quasi-particle resonance at $\omega = 0$. The change of the spectrum for different values of Λ is shown in Fig. 5.3 for $U = 6\Delta_0$ and $\beta = 50/\Delta_0$.

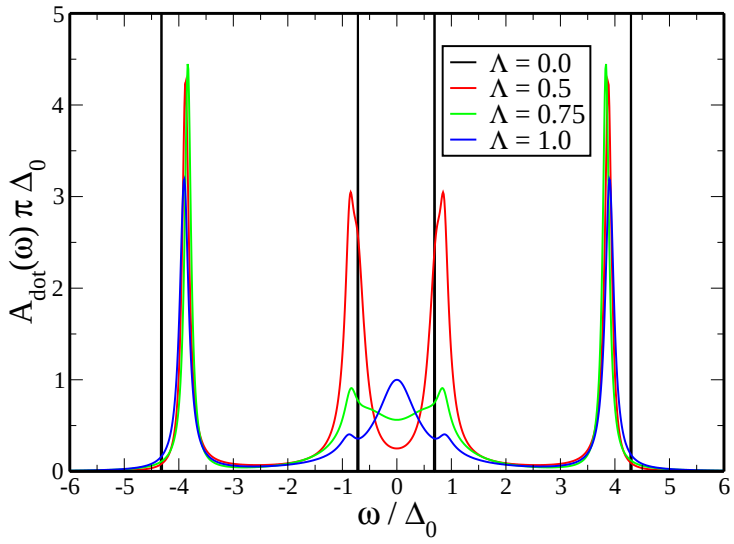

Figure 5.3: $L = 1$ dot spectra for several values of Λ at half filling and $U = 6\Delta_0$ and $\beta = 50/\Delta_0$, obtained from a Padé-approximation to our numerical data on the imaginary frequency axis. The atomic limit peaks become slightly broadened and their position changes from $4.2\Delta_0$ to $3.9\Delta_0$. At small frequencies a central resonance with height $A_{\mathrm{dot}}(\omega = 0) = 1/\pi\Delta_0$ is emerging during the fRG flow from $\Lambda = 0$ to $\Lambda = 1$.

The peaks $\epsilon_{1,2}$ become slightly broadened, but their positions does not change significantly. In the end of the flow (for $\Lambda = 1$) their maxima are not located at $\pm U/2 = \pm 3\Delta_0$, the position usually expected in the wide band limit with a purely imaginary hybridization function $\Delta(\omega)$ on the real frequency axis. However, in the present case where the bandwidth is less than U the hybridization function $\Delta(\omega)$ has a finite real part, which renormalizes this position. The small broadening of these high-energy peaks is related to the fact that they lie outside the bandwidth $(-2\Delta_0, 2\Delta_0)$ of the bath, such that the width is purely due to self-energy effects. During the flow, already for small values of Λ, the low-energy peaks $\epsilon_{3,4}$ become broadened and a central resonance at $\omega = 0$ with $A_{\mathrm{dot}}(\omega = 0) = \frac{1}{\pi\Delta_0}$ emerges. Note that at the end of the flow, for $\Lambda = 1$, there are still remnants of the peaks $\epsilon_{3,4}$, which is interpreted as an artefact of the approximation.
In Fig. 5.4 we show the dot spectra for $U = 6/\Delta_0$ and $\beta = 30/\Delta_0$ calculated for $L = 1$, approximation 1 and 2 and $L = 3$, approximation 1 in comparison with a NRG spectrum calculated at $T = 0$. In the NRG spectrum the Hubbard peaks are located at $\pm 3.9\Delta_0$, which is comparable to the result of the fRG calculation. One can see that the position of the Hubbard peaks moves closer to the position found in the NRG calculation when we increase the approximation-level of the fRG flow or the size of the core. The Hubbard peaks found in the NRG calculation are much more broader compared to the fRG calcu-

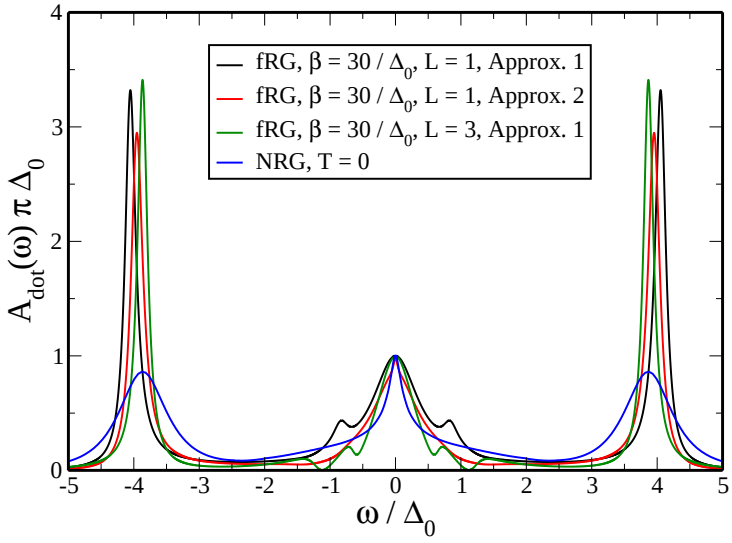

Figure 5.4: Dot spectra for $U = 6\Delta_0$ and $\beta = 30/\Delta_0$, calculated for $L = 1$, approximation 1 and 2 and $L = 3$, approximation 1 in comparison with a NRG spectrum calculated at $T = 0$ for the same semi-elliptic density of states.

lation, which is partly due to the logarithmic broadening of the conduction band in the NRG setup. The peaks at the shoulders of the central resonance, which are interpretated as remnants of the discrete core spectrum, are also visible in the $L = 3$-spectrum. For approximation 2 of the $L = 1$-core they have disappeared, although this is not generic for all parameter sets. At $T = 0$ one have $A_{\mathrm{dot}}(\omega = 0) = \frac{1}{\pi\Delta_0}$ as expected from Friedel's sum rule (4.13). This is indeed fulfilled in approximation 1. In approximation 2 there is a small deviation which corresponds to the small step in the Matsubara self-energy at $i\omega = 0$. This deviation is again due to finite temperature.

5.2.1 Results for the effective mass in comparison

To investigate if the Kondo scale (4.11) is present in our approach, we calculated the effective mass m^* which is defined as the inverse quasi-particle weight Z.

$$m^* = Z^{-1} = 1 - \left.\frac{\mathrm{dIm}\Sigma_{\mathrm{dot}}\left(i\omega\right)}{d\omega}\right|_{\omega=0^+}. \tag{5.7}$$

In the Kondo regime the quasi-particle weight Z determines the width of the Kondo resonance and is expected to scale exponentially with the interaction strength $Z \propto T_K$ (cf. chapter 4.1).
In Fig. 5.5 we show the effective mass for $L = 1$, approximation 1 and 2 and $L = 3$, approximation 1 in comparison with NRG data as function of the interaction strength

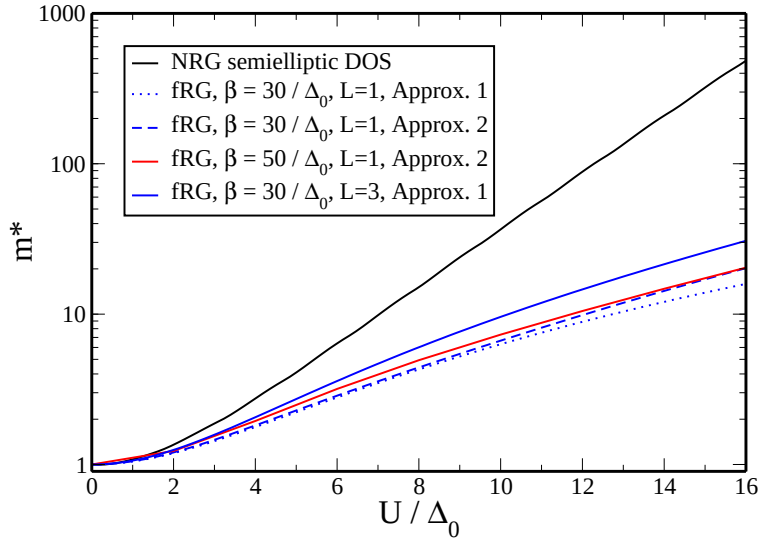

Figure 5.5: Effective mass ($\beta = 30, 50/\Delta_0$) for $L = 1$, approximation 1 and 2 and for $L = 3$, approximation 1 in comparison with NRG data. The NRG data are calculated for a bath with semi-elliptic density of states.

U. The NRG data are calculated at $T = 0$ for a semi-elliptic bath density of states. While the qualitative behaviour is similar, the effective mass from the fRG calculations is systematically too small compared with the NRG data and we can not reproduce the exponential Kondo scale quantitatively. For interaction strengths $U \sim 8-9\Delta_0$ the Kondo scale (4.11) becomes comparable with the temperature $T_K \approx \frac{1}{\beta}$, which we expect to be part of the reason for the deviations from the NRG result at large values of U. Note the slight increase of m^* with decreasing temperature in Fig. 5.5.

Our results for the effective mass fall in the range of other fermionic fRG approaches to the Anderson model [KHP+08, JPS10] (cf. Fig. 5.6), that are calculated for a bath in the wide band limit. A direct comparison of the data needs to take into account the fact that, as can be seen from the NRG data in Fig. 5.6, the effective mass $\propto T_k^{-1}$ for a semielliptic density of states with finite bandwidth is in general larger than for a bath in the wide band limit. For a small bandwidth $W \ll U$ the Kondo scale is $\propto W$ as in Eq. (4.11). Towards larger values of W it increases and reaches in the wide band limit $W \gg U$ a constant, which is given by $T_K = \sqrt{\frac{U\Delta_0}{2}} \exp\left[-\frac{\pi U}{8\Delta_0}\right]$ [Hew93], independent of W.

The failure in reproducing the exponential Kondo scale in the effective mass precisely is however common to all finite-frequency fRG approaches to the Anderson model. Note, that all fRG approaches truncate the hierarchy of flow equations after the two-particle level. Hence, we expect that this approximation is the reason for this deviation.

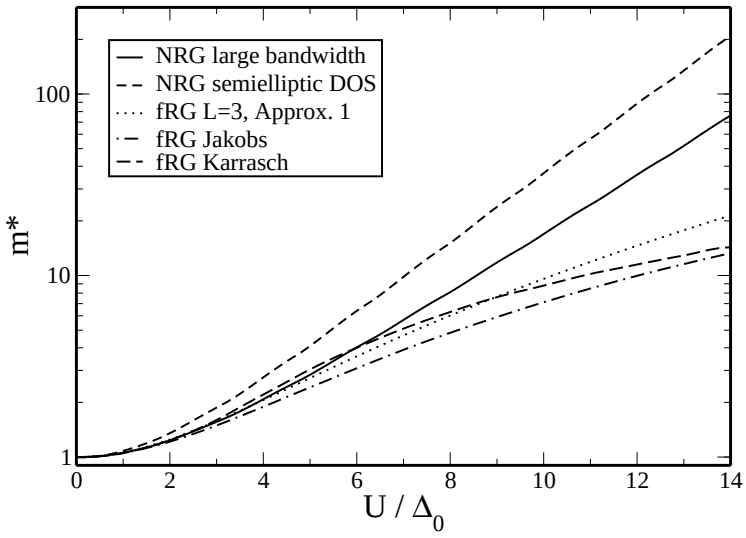

Figure 5.6: Effective mass ($\beta = 30/\Delta_0$) for $L = 3$, approximation 1 in comparison with fRG data from Ref. [JPS10] and approximation 1 in Ref. [KHP$^+$08]. As reference data we show NRG calculations for a semielliptic density of states and in the wide band limit.

5.2.2 Results for the conductance

We furthermore calculated the linear conductance of the dot $G = \sum_\sigma G_\sigma$ given by (we set $\hbar = e^2 = 1$) [MW92]

$$\begin{aligned} G_\sigma =& \frac{1}{2}\pi v^2 \int d\omega A_{d,\sigma}(\omega)\, \rho_b(\omega) \left(-\frac{\partial n_F(\omega)}{\partial \omega}\right) \\ \simeq& \frac{1}{2}\Delta_0 \int d\omega A_{d,\sigma}(\omega) \left(-\frac{\partial n_F(\omega)}{\partial \omega}\right). \end{aligned} \tag{5.8}$$

In the second line we used that the derivative of the Fermi function is sharply peaked at low temperature at $\omega = 0$ so that the ω-dependence of $\rho_b(\omega)$ can be neglected. Especially at zero temperature the derivative is given by a delta function and from Friedel's sum rule (4.13) one gets

$$G = \Delta_0 A_d(0) = \frac{\sin^2(\pi \langle n_{d,\sigma}\rangle)}{\pi} \tag{5.9}$$

In the Kondo regime, i.e. for gate voltages between $-\frac{U}{2}$ and $\frac{U}{2}$, the dot is occupied by a single electron, $\langle n_{d,\sigma}\rangle = 1/2$, leading to $G = \frac{1}{\pi} = 2G_0$, which is the unitary limit value[1]. The conductance is derived by an integral over the real frequency axis and at first sight one has to perform an analytic continuation. To circumvent this, we follow an approach,

[1] In physical units one has $G_0 = \frac{e^2}{h}$.

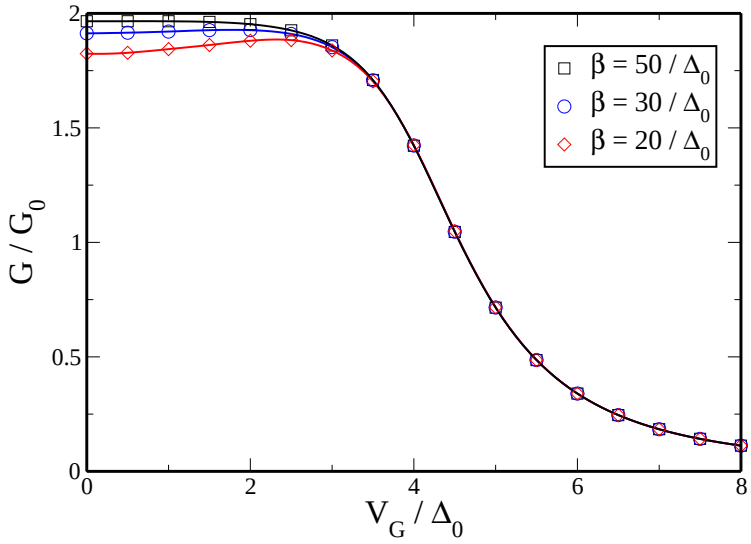

Figure 5.7: Comparison of the linear conductance for $U = 8\Delta_0$ and $\beta = 20, 30, 50/\Delta_0$, calculated in approximation 1. The value $G(V_G = 0)$ decreases quadratically with increasing temperature.

proposed in Ref. [KMS10], which does not require an analytic continuation. In this approach G follows from the formula

$$G_\sigma \simeq \Delta_0 T \sum_{\alpha>0} R_\alpha \mathrm{Im} \frac{d\mathcal{G}_\sigma(i\tilde{\omega}_\alpha)}{d\tilde{\omega}_\alpha}, \tag{5.10}$$

where the imaginary frequencies $i\tilde{\omega}_\alpha$ and the weights R_α are defined in Ref. [KMS10]. The frequencies $i\tilde{\omega}_\alpha$ differ from the original Matsubara frequencies and we determine $\frac{d\mathcal{G}_\sigma(i\tilde{\omega}_\alpha)}{d\tilde{\omega}_\alpha}$ from a Padé-approximation.

In Fig. 5.7 we show G as function of the gate voltage V_g for several temperatures and $U = 8\Delta_0$. At low temperatures $\beta = 50/\Delta_0$ we get a plateau in the conductance for gate voltages between $-\frac{U}{2}$ and $\frac{U}{2}$, as expected from Friedel's sum rule. For higher temperatures the conductance at $V_g = 0$ decreases quadratically with the temperature.

In Fig. 5.8 the linear conductance derived in the two approximation schemes 1 and 2 is shown. In approximation 2 the linear conductance for small gate voltages is reduced in comparison with approximation 1. We understand this again as a finite temperature effect. In approximation 2, the Kondo peak gets narrower, i.e. the effective Kondo scale comes out smaller. Hence, in this approximation the actual temperature β^{-1} is closer to T_K as in approximation 1 and the conductivity shows a stronger finite temperature suppression.

Fig. 5.9 shows the suppression of the gate voltage at $V_G = 0$ due to a finite magnetic

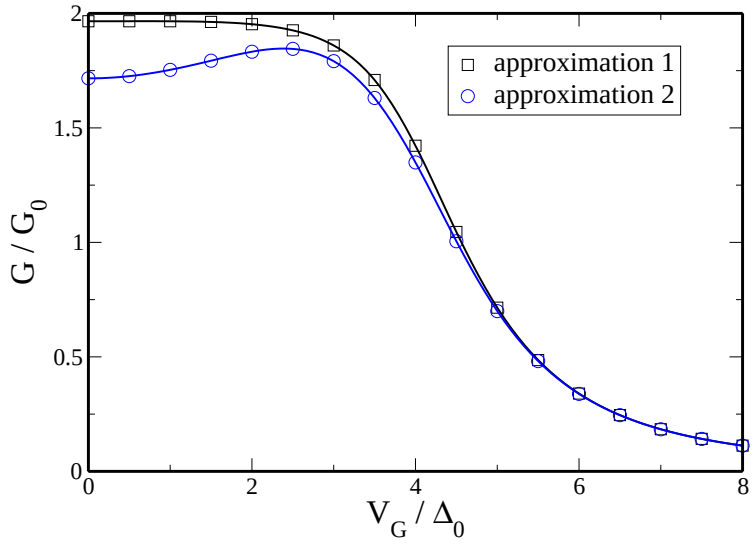

Figure 5.8: Comparison of approximation 1 and 2 to the linear conductance for $U = 8\Delta_0$, $\beta = 50/\Delta_0$. In approximation 2 the linear conductance for small gate voltages is reduced in comparison with approximation 1.

field. As shown in Ref. [KEM06] one can extract the Kondo scale from this supression within a frequency independent fRG scheme with frequency cutoff. Therefore one defines the Kondo scale T_K as equal to the magnetic field $B_{1/2}$ that is required to suppress the gate voltage $G(V_G = 0)$ to $G_0 = e^2/h$, which is one half of the unitary limit.
In the right part of Fig. 5.9 we show $B_{1/2}$ as function of U. As shown the data for small U can be fitted to an exponential curve of the form $a \exp(-bU/\Delta_0)$. This behaviour is expected in the Kondo regime. Here we find it already for these intermediate values of U. For larger U there are systematic deviations from exponential behaviour. These deviations begin at $U \sim 8 - 9\Delta_0$, where the Kondo scale according to this association becomes comparable to the temperature, $T_K \approx \frac{1}{\beta} = \frac{\Delta_0}{30}$. From our fit we get $b \approx 0.32$, in good agreement with the exact value $b = \pi/8 \approx 0.39$ (cf. Eq. (4.11)).

5.2.3 Results for the spin suseptibility and Wilson ratio

We also calculated the static spin susceptibility, which is defined by

$$\chi_s = \left. \frac{d\left(\langle n_\uparrow \rangle - \langle n_\downarrow \rangle\right)}{dB} \right|_{B=0}. \tag{5.11}$$

Here $\langle n_\sigma \rangle$ is the average occupation of electrons with spin σ, which is calculated by

$$\langle n_\sigma \rangle = \frac{1}{2} + 2T \sum_{\alpha > 0} R_\alpha \mathrm{Re}\, \mathcal{G}_\sigma(i\tilde{\omega}_\alpha) \tag{5.12}$$

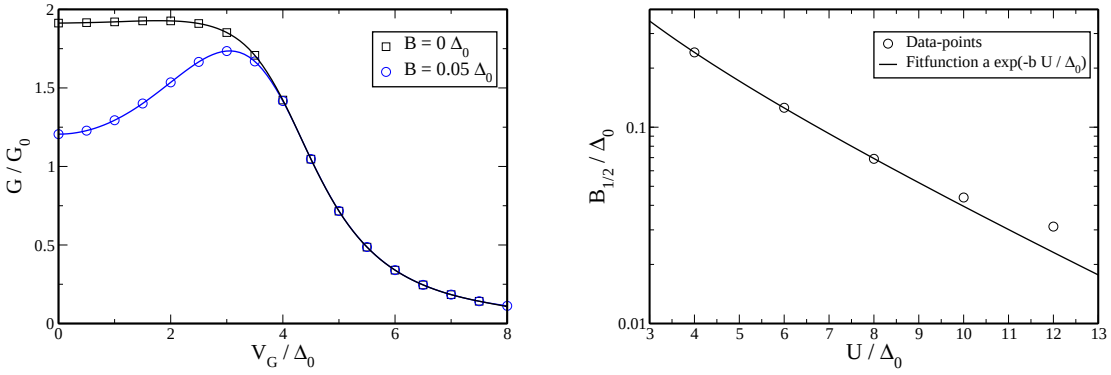

Figure 5.9: Left: Linear conductance for $U = 8\Delta_0$, $\beta = 30/\Delta_0$, calculated in approximation 1. For a finite magnetic field $B = 0.05\Delta_0$ the linear conductance for small gate voltages is reduced in comparison with zero magnetic field. Right: $B_{1/2}$, i.e. the magnetic field that is required to supress $G(V_G = 0)$ to $G_0 = e^2/h$, as function of U, $\beta = 30/\Delta_0$, approximation 1, together with an exponential fit curve $a \exp(-bU/\Delta_0)$.

with the same R_α and $\tilde{\omega}_\alpha$ as in Eq. (5.10).

In Fig. 5.10 we show the spin susceptibility in comparison with NRG data. For large values of U the spin susceptibility is expected to be inversely proportional to the Kondo temperature $\chi_s \sim 1/T_K$ [Hew93]. Therefore one expects an exponential dependence on the interaction strength. While the susceptibility definitely rises with increasing U, the exponential behaviour is not found in our fRG approach. A part of this deviation might again be a thermal effect, as for $U \gtrsim 8 - 9\Delta_0$ the Kondo temperature falls below β^{-1} where the calculation takes place.

In Fig. 5.11 we show the Wilson ratio, which is defined as $R = \frac{\pi^2}{3}\frac{\chi_s}{\gamma}$, whereat γ is the linear coefficient of the specific heat C, i.e. $C = \gamma T$. In the Anderson impurity model one has $\gamma = \frac{2\pi}{3}\frac{m^*}{\Delta_0}$ [Hew93], such that we can calculate R from our data of the effective mass and the spin susceptibility. With the relation $\frac{1}{m^*} = \frac{4}{\pi\Delta_0(\chi_s+\chi_c)}$, which follow from the Yamada-Yosida Ward Identities [Hew93, KBC+10], we get $R = \frac{2\chi_s}{\chi_s+\chi_c}$ with the charge susceptibility $\chi_c = \lim_{\mu\to 0}\sum_\sigma \frac{d\langle n_\sigma\rangle}{d\mu}$. In the Kondo regime charge fluctuations are completely suppressed, i.e. $\chi_c = 0$, which leads to $R = 2$. As seen in Fig. 5.11, for $U \gtrsim 8\Delta_0$ the fRG data come out very close to $R = 2$ even though χ_s is too small in the fRG. This points to advantageous cancellations of errors for this ratio in the fRG. Indeed m^* comes out too small as well. The slight decrease of R for $U > 9\Delta_0$ might be again due to effects of finite temperature.

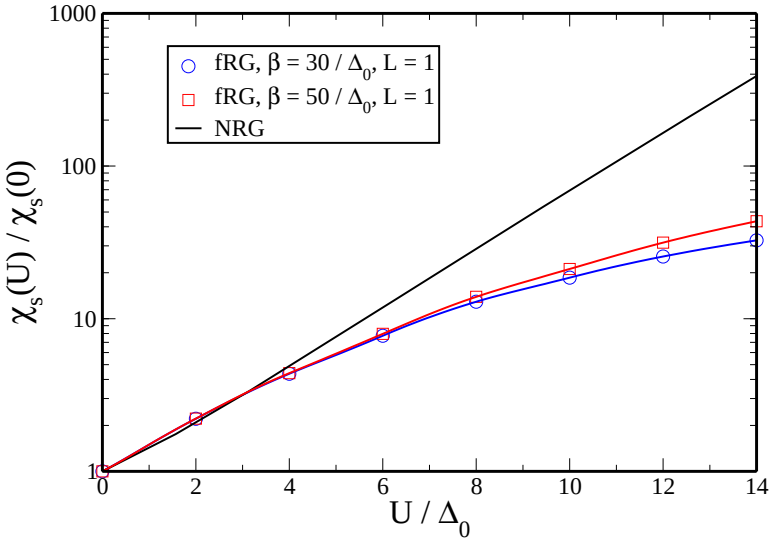

Figure 5.10: Spin susceptibility as function of U, $\beta = 30/\Delta_0, 50/\Delta_0$, approximation 1 in comparison with NRG data.

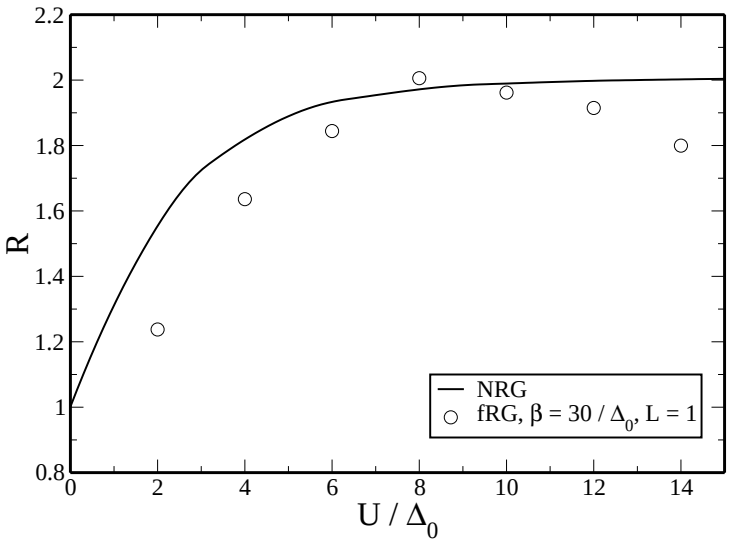

Figure 5.11: Wilson ratio R as function of U, $\beta = 30/\Delta_0$, approximation 1 in comparison with NRG data.

5.3 Conclusion

In this chapter we applied the fRG hybridization flow scheme to the single impurity Anderson model with a semi-elliptic bath density of states. The results show a pronounced even-odd effect. In the case $L = 0$ we were not able to describe the local Fermi liquid properties of the Anderson model, although the divergence of the self-energy $\Sigma_{\mathrm{dot}}(i\omega)$ at $i\omega = 0$ was cured by the flow. Similar results were obtained in the case $L = 2$. In contrast with this, the numerical results for clusters with an odd number of sites ($L = 1$ and $L = 3$) showed that the flow equations are able to recover the Fermi liquid behaviour. This even-odd disparity is interpreted as an effect of the total spin of the initial condition, i.e. the isolated core. Apparently, the truncated flow scheme is not able to change the system from a nonzero moment to a screened moment. The dependence of the quasi-particle weight Z with increasing U is quantitatively different from NRG results and we were not able to reproduce the correct exponential dependence. The deviations at large U might be partly due to the finite temperature, for which our scheme is implemented. We also derived the linear conductance as function of the gate voltage and could reproduce the conductance plateau, which is expected in the Kondo regime from Friedel's sum rule. The suppression of the plateau value $G(V_g = 0)$ by a finite magnetic field showed signs of exponential behaviour, although a clear statement is again difficult due to the finite temperature scale in our calculations. A similar statement holds for the spin susceptibility, where the exponential behaviour in the Kondo regime could not be reproduced correctly. The Wilson ratio was for large values of U approximately equal to 2, which is the expected value in the Kondo regime. Summarizing these findings, we state that the hybridization flow for an even number of core sites provides a qualitatively correct description of the Kondo physics in the SIAM. Quantitatively the method cannot compete with established solvers, but as the fRG is a versatile method, it may still be useful to explore the uses of the proposed scheme further.

Chapter 6

Hybridization Flow and Dynamical Mean Field Theory

In this chapter we show that the hybridization flow setup can be used as impurity solver in the dynamical mean field theory, i.e. in DMFT(fRG). Primarily, the fRG is still a relatively cheap impurity solver in terms of numerical effort, so studying its applicability in the DMFT framework may be useful. Furthermore, the fRG is a flexible and transparent method that nicely illustrates how non-local correlations emerge from local interactions, so using the fRG to build in correlations beyond the local physics may be rewarding. If one wants to pursue this line, one should check how well the fRG works for small cores. We will see, that in DMFT(fRG) the hallmarks of the Mott transition can be reproduced, but also notice some technical complications, that may require further improvements of the fRG scheme in order for the method to become truly competitive with other established solvers. But as the results are qualitatively reasonable and the numerical effort is rather manageable, we can go to a second field of interest, the frequency structure of the local and non-local effective interaction vertices, which explicitly appear in our DMFT(fRG) scheme. As already mentioned these quantities play an important role in non-local extensions of the single-site DMFT setup. We find that the effective vertices exhibit "boson-like" frequency features, but also other "loop-coupling" features, that are not easily captured by simple parameterizations of the frequency dependence in terms of frequency transfers or the total frequency. Here, our findings confirm results by the Vienna group [RVT12] for the local vertex, obtained with DMFT using exact diagonalization (ED) as impurity solver, and expand them to the non-local situation.

Parts of this chapter are already presented in
Michael Kinza and Carsten Honerkamp. Two-particle correlations in a functional renormalization group scheme using a dynamical mean-field theory approach. *Phys. Rev. B*, 88:195136, Nov 2013

6.1 The Hubbard model

The one-band Hubbard model [Hub63, Gut63, Kan63] is a conceptually simple, but nevertheless highly nontrivial model to describe correlated lattice fermions. At half filling it is given by

$$\hat{H} = \hat{H}_t + \hat{H}_U, \tag{6.1}$$

$$\hat{H}_t = \sum_{i,j,\sigma} t_{ij} c^\dagger_{i,\sigma} c_{j,\sigma} \tag{6.2}$$

$$\hat{H}_U = U \sum_i \left(\hat{n}_{i,\uparrow} - 1/2\right)\left(\hat{n}_{i,\downarrow} - 1/2\right), \tag{6.3}$$

where $c^\dagger_{i,\sigma}(c_{i,\sigma})$ create (annihilate) electrons with spin σ on site i and $\hat{n}_{i,\sigma} = c^\dagger_{i,\sigma} c_{i,\sigma}$. t_{ij} is the hopping amplitude between lattice sites i and j and $U > 0$ is the onsite Coulomb repulsion. If the model is defined on a bipartite lattice, the interaction part of the Hamiltonian (6.3) is particle-hole symmetric.

The Hubbard model describes a complex many body problem, which except for dimension $D = 1$ [LW68] cannot be solved analytically. The physical behaviour of this model is determined by the competition between the kinetic energy $\hat{H}_t$ and the local interaction-energy $\hat{H}_U$. Due to the kinetic energy electrons hop from one lattice site to the next, which leads to doubly occupied sites. These have to be paid by an onsite repulsion energy U. For a better understanding of the interplay between these two effects, it is instructive to have a look at two limiting cases:

For $U = 0$ the electrons behave as delocalized Bloch electrons with band dispersion $\epsilon_{\vec{k}} = \frac{1}{N}\sum_{i,j} \mathrm{e}^{i\vec{k}(\vec{R}_i - \vec{R}_j)} t_{ij}$. If we assume that the model is defined on a two-dimensional squarelattice and that $t_{ij} = -t$ for nearest neighbours $\langle i, j\rangle$ and $t_{ij} = 0$ else, the band dispersion is given by

$$\epsilon_{\vec{k}} = -2t\left[\cos(k_x) + \cos(k_y)\right] \tag{6.4}$$

with bandwidth $W = 8t$. At half filling the system is metallic. At small $U \ll t$ the system remains in a Fermi liquid state with a coherent quasi-particle weight (cf. upper part of Fig. 6.1.a).

For a large local repulsion $U \gg t$ doubly occupied sites become energetically costly, and hence the system will minimize its energy by localizing the electrons leading to one spin 1/2 degree of freedom on each lattice site. Due to the large Coulomb-repulsion the mobility of the electrons is thereby strongly supressed resulting in a correlated Mott Insulator state. The spectral density splits into a lower (LHB) and an upper Hubbard band (UHB) (cf. lower part of Fig. 6.1.a), that are separated by the energy scale U.

Fluctuations of the localized spins are well described by the antiferromagnetic spin 1/2 Heisenberg model with exchange energy $J \propto t^2/U$ [AS06], which follows as effective model

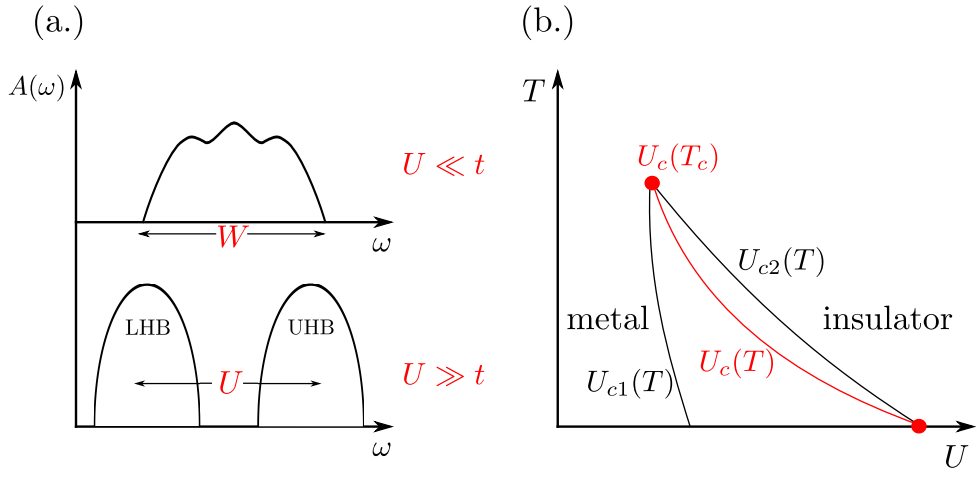

Figure 6.1: Schematic illustration of the Mott metal-insulator transition in the infinite-dimensional Hubbard model. (a.) For $U \ll t$ and for suppressed magnetic order the system is metallic with a finite quasi-particle weight. In the case $U \gg t$ the spectrum splits into a lower (LHB) and an upper Hubbard band (UHB), separated by a gap proportional to the interaction energy U. The system is in a correlated Mott insulator state. (b.) Phase-diagram of the Mott metal-insulator transition in the U-T plane. Below a critical end point T_c one finds a coexistence region $U_{c1}(T) < U < U_{c2}(T)$ where metallic and insulating solutions coexist. At $U_c(T)$ a first order phase transition occurs.

from the Hubbard model in this limit. On bipartite lattices the Heisenberg model shows long-range antiferromagnetic order with finite T_c for $D > 2$ [DLS78, KLS88] and with $T_c = 0$ in $D = 2$ [Hoh67, MW66].

In between these two limiting cases one finds a Mott metal-insulator transition (MIT) with critical interaction strength $U_c \sim W$ [Mot68, Geb97]. In the transition region one has $\langle \hat{H}_t \rangle \approx \langle \hat{H}_U \rangle$, and to find reliable, controlled approximation schemes, which can describe this transition, is therefore very challenging. Early attempts use a Green's function decoupling scheme [Hub63, Hub64], which can describe the splitting into a lower and an upper Hubbard band in the insulating region, but fails in describing the low energy quasi-particle behaviour in the metallic phase. On the contrary, the latter is well described by the Gutzwiller-Brinkman-Rice approach [Gut63, Gut65, BR70] without reproducing the lower and upper Hubbard bands. A numerically controlled access to the Mott MIT, which bases on the limit of infinite dimensions, and a quantitative theory of models and materials near or in the Mott state can be given by the various forms of the dynamical mean field theory (DMFT) [GKKR96, PJF95, KV04]. A detailed introduction into this method can be found in the next section.

In Fig. 6.1.b we show the DMFT phase-diagram of the Mott transition in the infinite-dimensional Hubbard model (in the paramagnetic case, i.e. for suppressed magnetic order). Below a critical temperature T_c one finds a coexistence region $U_{c1}(T) < U <$

$U_{c2}(T)$, where the DMFT equations allow for both, a metallic and an insulating solution. The width of the quasi-particle in the metallic solution ceases to exist at the line $U_{c2}(T)$, while the insulating gap vanishes at $U_{c1}(T)$. The first-order phase transition occurs at the line $U_c(T)$, where the free energies of both phases are equal. At the critical end points $U_c(0)$ and $U_c(T_c)$ the phase transition is second order.

6.2 Dynamical Mean Field Theory

The theoretical description of classical and quantum mechanical systems can be simplified, if one considers the limit of high spatial dimension or high coordination number respectively. In this limit mean field theories become exact, as for example the Weiss mean field theory for the classical Ising model, in which a single localized spin is only influenced by the other spins via a static magnetization [Bax82]. To describe correlation effects in quantum mechanical fermion systems such a static mean field approach (like for example the Hartree-Fock theory) is not sufficient, and one has to apply a *dynamical* mean field theory. Here, a local problem for a subset of the full lattice, augmented by a dynamical Weiss field that represents the influence of the environment, is solved exactly by means of an impurity solver. Then the solution of this local problem is proliferated to the whole lattice, from which a new Weiss field is determined and the local problem is solved again. This procedure is iterated until the Weiss field and the local properties converge. In the following we deduce the DMFT selfconsistency equations for the single-band Hubbard model.

6.2.1 Single-site DMFT

We study the Hubbard model (6.1) on a Bethe lattice with infinite connectivity $z \to \infty$. To make sure that it is physically meaningful we have to scale the hopping parameter t like $\frac{t^*}{\sqrt{z}}$ with constant t^* [MV89]. The local density of states (DOS) is then semi-elliptic [Eco06]

$$\mathrm{DOS}\left(\omega\right) = \frac{1}{2\pi t^2}\sqrt{4t^2 - \omega^2}\,\Theta\left(2t - |\omega|\right) \tag{6.5}$$

with bandwidth $W = 4t$ [1]. The self-energy becomes a purely local quantity i.e. $\Sigma_{ij}\left(i\omega\right) = \Sigma_i\left(i\omega\right)\delta_{ij}$ and because of translational invariance it is site-independent $\Sigma_i\left(i\omega\right) = \Sigma\left(i\omega\right)$. The local lattice Green's function is then given by

$$\mathcal{G}(i\omega) = \int \mathrm{d}\epsilon \frac{\mathrm{DOS}(\epsilon)}{i\omega - \Sigma(i\omega) - \epsilon} = \mathcal{G}_0(i\omega - \Sigma(i\omega)) \tag{6.6}$$

with the free local lattice Green's function $\mathcal{G}_0$.

[1] Here and in the following we denote t^* by t.

The local self-energy can be written as a functional of the local lattice Green's function $\Sigma = \mathcal{S}[\mathcal{G}]$ in terms of skeleton diagrams [GK92, Jar92]. This can be used to map the Hubbard model to a single impurity Anderson model (4.1), which describes a dot level with onsite energy ϵ_d and local interaction U that is coupled by a hybridization-term $V_{\vec{k}}$ to uncorrelated bath levels with energy $\epsilon_{\vec{k}}$.
The local dot Green's function is given by

$$\mathcal{G}_{\mathrm{dot}}(i\omega) = \frac{1}{i\omega - \epsilon_d - \Sigma_{\mathrm{dot}}(i\omega) - \Delta(i\omega)} \tag{6.7}$$

with the hybridization function

$$\Delta(i\omega) = \sum_{\vec{k}} \frac{|V_{\vec{k}}|^2}{i\omega - \epsilon_{\vec{k}}}. \tag{6.8}$$

The self-energy is by construction local on the dot level and it has the same functional dependence on the dot Green's function as in the Hubbard model $\Sigma_{\mathrm{dot}} = \mathcal{S}[\mathcal{G}_{\mathrm{dot}}]$. If we now choose the parameters $V_{\vec{k}}$ and $\epsilon_{\vec{k}}$ such that

$$\Delta(i\omega) = i\omega - \epsilon_d - \Sigma_{\mathrm{dot}}(i\omega) - \mathcal{G}(i\omega)^{-1} \tag{6.9}$$

holds, we arrive at

$$\Sigma_{\mathrm{dot}}(i\omega) = \Sigma(i\omega). \tag{6.10}$$

With Eqs.(6.6), (6.9) and (6.10) we can express $\Delta(i\omega)$ by the free hybridization function $\Delta_0(i\omega) = i\omega - \epsilon_d - \mathcal{G}_0(i\omega)^{-1}$ via

$$\Delta(i\omega) = \Delta_0(i\omega - \Sigma(i\omega)). \tag{6.11}$$

The Eqs. (6.6), (6.9) and (6.10) form a set of self-consistency equations for the local self-energy $\Sigma(i\omega)$ (cf. Fig. 6.2). To solve the SIAM a large class of impurity solvers is available, like for instance the numerical renormalization group [BHP98, Bul99], the quantum Monte Carlo [Jar92, RZK92] or the exact diagonalization method [CK94, LI12].

6.2.2 Hybridization flow scheme as impurity solver

In the following we use the hybridization flow fRG scheme as impurity solver in the DMFT. In order to apply this scheme we have to map the bath of the Anderson model to a semi-infinite tight binding chain in which its first site is connected to the impurity site (cf. chapter 4.1.1).

$$\begin{aligned}\hat{H}_{\mathrm{And}} =& \epsilon_d \sum_\sigma d_\sigma^\dagger d_\sigma + U \sum_\sigma \left(\hat{n}_{d,\uparrow} - 1/2\right)\left(\hat{n}_{d,\downarrow} - 1/2\right) - v \sum_\sigma \left(d_\sigma^\dagger b_{1,\sigma} + H.c.\right) \\ & - \sum_{i=1}^{\infty} \sum_\sigma t_i \left(b_{i,\sigma}^\dagger b_{i+1,\sigma} + H.c.\right) + \sum_{i=1}^{\infty} \sum_\sigma \epsilon_i b_{i,\sigma}^\dagger b_{i,\sigma}\end{aligned} \tag{6.12}$$

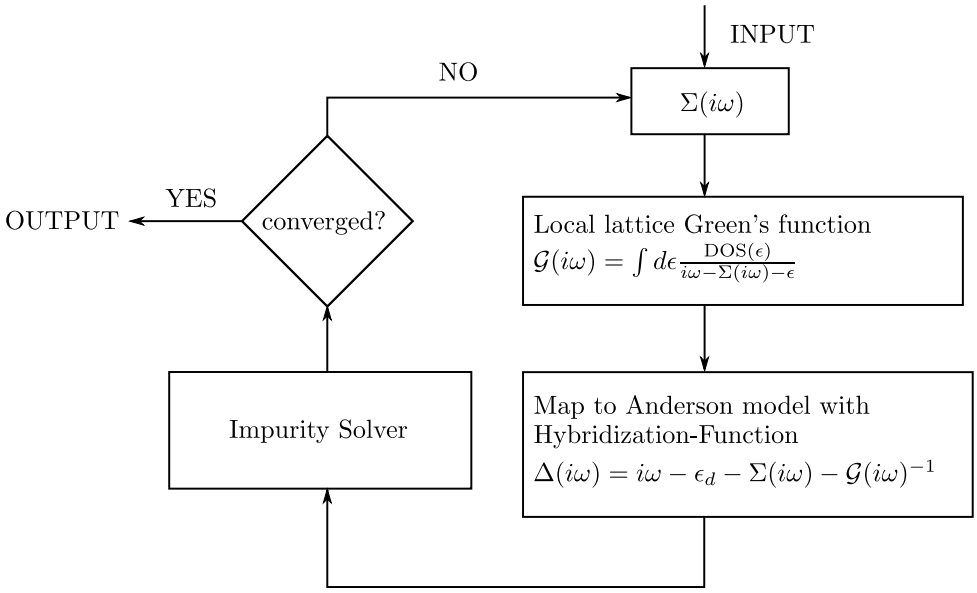

Figure 6.2: The picture illustrates the DMFT self-consistency cycle that involves the Eqs. (6.6), (6.9) and (6.10)

For a semi-elliptic local DOS (6.5) we have to choose $\epsilon_i = 0$ and $t_i = t$ for all i. Then the free hybridization function has the form

$$\begin{aligned} \Delta_0(i\omega) =& v^2 g_t\left(i\omega\right) \\ \text{with } g_t\left(i\omega\right) =& \frac{1}{2t^2}\left(i\omega - i\mathrm{sgn}(\omega)\sqrt{4t^2 - (i\omega)^2}\right). \end{aligned} \tag{6.13}$$

If we now additionally choose $\epsilon_d = 0$ and $v = t$ the free local dot Green's function $\mathcal{G}_0$ is given by g_t and the local $\mathrm{DOS}(\omega) = -\frac{1}{\pi}\mathrm{Im}\ \mathcal{G}_0\left(i\omega \to \omega + i0^+\right)$ is semi-elliptic (cf. chapter 4.1.2).

Insulating phase

We saw in chapter 5.1 that our fRG scheme is not able to reproduce the Fermi liquid properties of the SIAM, if the core consists only in the impurity site (case $L = 0$). This choice of the core is therefore not suitable to describe the metallic phase of the Hubbard model, which can be characterized by a finite quasi-particle weight Z. However one can still hope to arrive at a reasonable description of the insulating phase even with this simplest choice for the core. Below we see that this indeed works.
The full hybridization function $\Delta(i\omega)$ is given by Eq. (6.11). It corresponds to a semi-infinite tight binding chain with a local term $\Sigma(i\omega)$ on each lattice site (cf. Fig. 6.3).

To get an estimate for which interactions U this approach delivers a reasonable description of an insulating phase, we show in Fig. 6.5 the gap Δ as function of U for $\beta = 30/t$. The

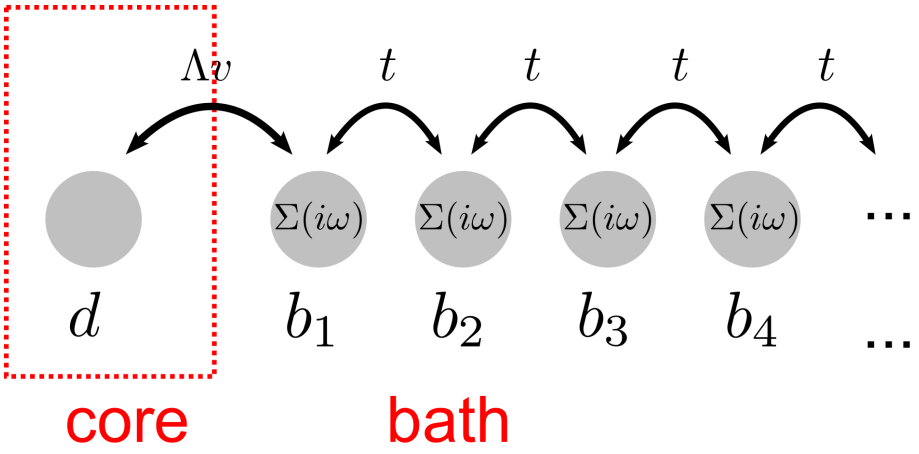

Figure 6.3: Anderson model for the case $L = 0$. The hybridization function $\Delta(i\omega) = \Delta_0(i\omega - \Sigma(i\omega))$ corresponds to a semi-infinite tight binding chain with a local term $\Sigma(i\omega)$ on each lattice site.

gap-sizes Δ are obtained from the spectral density calculated in approximation 1 of the fRG flow equations. The gap vanishes at $U_c \approx 3.8t$.

Metallic phase

In order to describe the metallic phase of the Hubbard model, the $L = 1$-core, containing the correlated site and one bath site is an appropriate starting point, as this core also successfully reproduced the Kondo central peak in the SIAM setup (cf. chapter 5.2). In the spectrum of the decoupled core one obtains two peaks near zero energy which leads to a continuous Matsubara self-energy at $i\omega = 0$ resulting with Eq. (5.7) in a finite quasi-particle weight Z.
The full hybridization function is again given by $\Delta(i\omega) = \Delta_0(i\omega - \Sigma(i\omega))$, but opposite to the $L = 0$-case a local self-energy term on the first bath site, which is part of the $L = 1$-core, is forbidden, because the exact diagonalization of the core requires a frequency independent core-Hamiltonian. To circumvent this we approximate $\Sigma(i\omega)$ for small frequencies as $\Sigma(i\omega) \approx (1 - Z^{-1})\, i\omega$, with the quasi-particle weight Z. The full hybridization function $\Delta(i\omega)$ is then given by

$$\begin{aligned}
\Delta(i\omega) &= \Delta_0(i\omega - \Sigma(i\omega)) \approx \Delta_0(i\omega/Z) \\
&= \frac{v^2}{2t^2}\left(\frac{i\omega}{Z} - i\mathrm{sgn}(\omega)\sqrt{4t^2 - \left(\frac{i\omega}{Z}\right)^2}\right) \\
&= \frac{(\sqrt{Z}v)^2}{2(Zt)^2}\left(i\omega - i\mathrm{sgn}(\omega)\sqrt{4(Zt)^2 - (i\omega)^2}\right) \\
&= (\sqrt{Z}v)^2 g_{Zt}(i\omega)
\end{aligned} \tag{6.14}$$

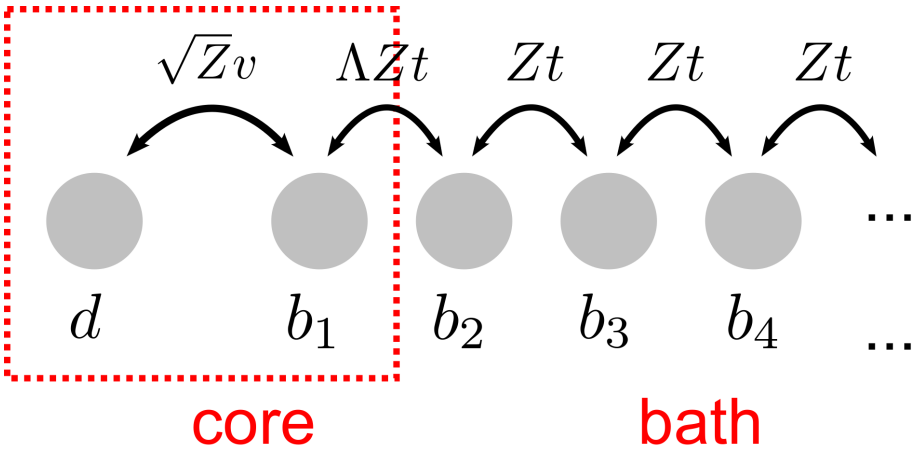

Figure 6.4: The Anderson model for the case $L = 1$. It corresponds to a semi-infinite tight binding chain with hopping Zt and impurity-bath coupling $\sqrt{Z}t$.

It corresponds to a semi-infinite tight binding chain with hopping Zt and impurity-bath coupling $\sqrt{Z}v$ (cf. Fig. 6.4). In each selfconsistency-cycle of the DMFT equations one calculates the quasi-particle weight Z from the local self-energy, which defines the new hopping-parameters in the next cycle. For $\Lambda = 0$, i.e. without solving the fRG flow equations, this scheme is equivalent to the two-site DMFT scheme[1], introduced in Ref. [Pot01]. This two-site DMFT scheme yields a satisfactory description of the Mott transition and the Fermi liquid state in the single-band Hubbard model at $T = 0$. The quasi-particle weight is predicted as $Z = 1 - U^2/U_c^2$ with $U_c = 1.5W$, which is very close to the result of the numerical renormalization group [Bul99]. For values of U larger than U_c this scheme reduces to the Hubbard-I-approximation [Hub63]. Our extended scheme is implemented at finite temperatures. In Fig. 6.5 we show the quasi-particle weight Z as function of U at $\beta = 30/t$ and $\beta = 50/t$ (calculated in approximation 1). These temperatures are still lower than the critical end point of the MIT phase diagram. The quasi-particle weight Z vanishes discontinuous at certain values $U_c(T)$, which marks the breakdown of the metallic state. For larger values of U the quasi-particle weight decreases in the DMFT cycle until a linearization of the self-energy is no more possible. Compared to the literature [Blu03], the obtained values $U_c(T)$ come out too small. Note that the approximation for the hybridization function (6.14) becomes very bad at large frequencies especially for small quasi-particle weights near the phase transition. The obtained U_c is larger than the interaction strength, where the gap Δ vanishes (cf. Fig. 6.5). Although one expects a hysteresis region at the phase transition and the two values are indeed different, a direct comparison is of course problematic due to the distinct approaches used to describe the insulating and the metallic phase.

[1]Not to be confused with the two-site cluster DMFT.

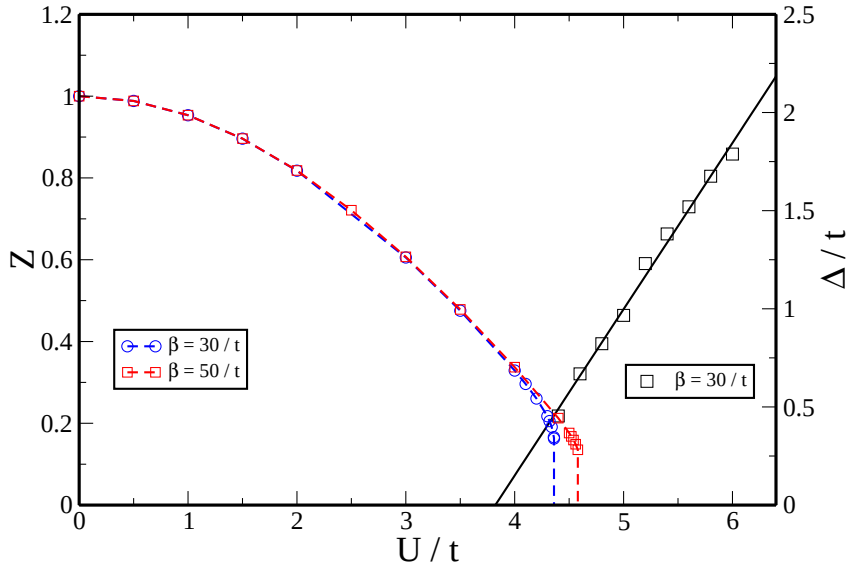

Figure 6.5: The plot shows the gap-size Δ in the insulating phase and the quasi-particle weight Z in the metallic phase as function of the interaction-strength U at several temperatures, calculated in single-site DMFT(fRG). The gap-sizes are estimated from the spectral density calculated in approximation 1 of the fRG flow equations. Compared to the literature [Blu03] the quasi-particle weight Z goes down too slowly, which is consistent with the behavior found in the Anderson Impurity case.

Note that unlike in the Anderson model, in the DMFT solution of the Hubbard model the quasi-particle weight Z is different from the effective Kondo energy scale, where the crossover to the strong coupling fix point in the renormalization group flow occurs [HPT13]. We expect this to be the reason, why we get a reasonable description of the metallic state in the Hubbard model, although the Kondo energy scale is not accurately resolved by the fRG hybridization flow setup (cf. chapter 5.2.1). As shown in Ref. [HPT13], the effective Kondo scale is connected with another energy scale in the Hubbard model, where kinks in the energy-momentum distribution [BKH$^+$07] and in the specific heat [TCCH09] occur. This second energy scale is probably absent in our fRG approach.

6.2.3 Two-site cluster DMFT

Although the DMFT is only exact in the limit of infinite dimensions, it turnes out to be an extremely useful approximation scheme for systems with finite dimension. In these systems non-local correlation effects like e.g. antiferromagnetic fluctuations or superconducting d-wave pairing play an important role and several extensions of the simple DMFT

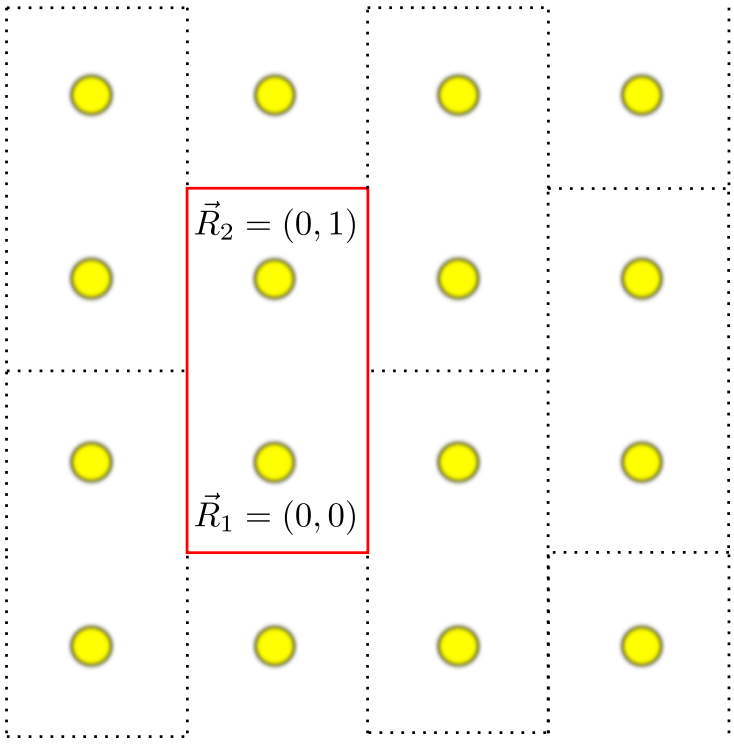

Figure 6.6: Tiling of the square lattice with two-site clusters. Each lattice site can be uniquely described by a cluster vector and the site within the cluster $\vec{R}_j$. Note that other periodic arrangements of the two-site clusters, corresponding to a different choice of the superlattice, would be also possible. However, this would only lead to another equivalent description of our problem and with our choice the quantities in the reciprocal superlattice acquire the most compact form.

framework exist that capture these effects. Important examples are perturbational expansions arround the local DMFT solution [SK04, TKH07, HKT08, RKL08, RKLG09] or numerical cluster DMFT schemes, where short-ranged correlations within a finite cluster are included [LK00, KSPB01, MJPH05].

In the following we extend our setup to a cluster DMFT scheme for the Hubbard model on a two-dimensional squarelattice with tight binding dispersion (6.4). As shown in Fig. 6.6 we divide the lattice into plaquettes with $L = 2$ sites. This breaks the translational invariance of the original lattice problem and introduces a superlattice Γ of clusters, whose sites form a subset of the original lattice γ. Each lattice site of the original lattice $\vec{r}_i$ can then be uniquely described by a cluster-vector $\vec{r}_m$ and the site within the cluster $\vec{R}_j$ as $\vec{r}_i = \vec{r}_m + \vec{R}_j$ [1].

The Brillouin zone of the original lattice (BZ_γ) contains L points of the reciprocal superlattice Γ^*. For the two-site clusters these are $\vec{K}_1 = (0,0)$ and $\vec{K}_2 = (\pi,\pi)$. Any wavevector $\vec{k} \in BZ_\gamma$ can be uniquely written as $\vec{k} = \vec{K} + \tilde{\vec{k}}$, with $\vec{K} \in \{\vec{K}_1, \vec{K}_2\}$ and $\tilde{\vec{k}}$

[1] Here we follow the notation of chapter 8 and 12 in [AM12].

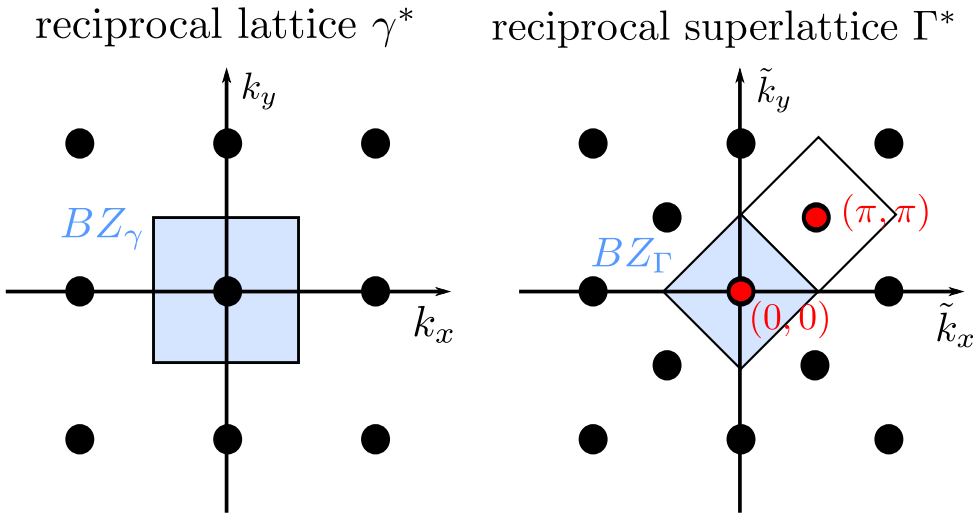

Figure 6.7: Reciprocal lattice γ^* with the first Brillouin zone BZ_γ and reciprocal superlattice Γ^* with Brillouin zone BZ_Γ. Any wavevector $\vec{k} \in BZ_\gamma$ can be uniquely written as $\vec{k} = \vec{K} + \tilde{\vec{k}}$ with $\tilde{\vec{k}} \in BZ_\Gamma$ and $\vec{K} \in BZ_\gamma \wedge \ \in \Gamma^*$.

belonging to the Brillouin zone of the superlattice (BZ_Γ) (cf. Fig. 6.7).
The hopping amplitude between two sites of the same cluster $\vec{R}_a$ and $\vec{R}_b$ can be obtained from the dispersion relation by the Fourier transformation

$$\begin{aligned} t_{ab} &= \frac{1}{N}\sum_{\vec{k}} \mathrm{e}^{i\vec{k}(\vec{R}_a-\vec{R}_b)}\epsilon_{\vec{k}} \\ &= \frac{1}{N}\sum_{\vec{K},\tilde{\vec{k}}} \mathrm{e}^{i(\vec{K}+\tilde{\vec{k}})(\vec{R}_a-\vec{R}_b)}\epsilon_{\vec{K}+\tilde{\vec{k}}} \\ &= \frac{L}{N}\sum_{\tilde{\vec{k}}} \underbrace{\mathrm{e}^{i\tilde{\vec{k}}(\vec{R}_a-\vec{R}_b)}\frac{1}{L}\sum_{\vec{K}} \mathrm{e}^{i\vec{K}(\vec{R}_a-\vec{R}_b)}\epsilon_{\vec{K}+\tilde{\vec{k}}}}_{\hat{t}_{ab}(\tilde{\vec{k}})}. \end{aligned} \tag{6.15}$$

$\hat{t}(\tilde{\vec{k}})$ is the partial Fourier transformation of the band dispersion, i.e. a matrix in the cluster space, which depends on the wavevector $\tilde{\vec{k}}$ of the reciprocal superlattice. For the tight binding dispersion (6.4) it is given by

$$\hat{t}(\tilde{\vec{k}}) = \begin{bmatrix} 0 & \mathrm{e}^{-i\tilde{k}_y}\epsilon_{\tilde{\vec{k}}} \\ \mathrm{e}^{i\tilde{k}_y}\epsilon_{\tilde{\vec{k}}} & 0 \end{bmatrix}. \tag{6.16}$$

The main approximation of cluster DMFT is now the assumption that the self-energy is local on each cluster, i.e. independent of $\tilde{\vec{k}}$. Then we obtain the $\tilde{\vec{k}}$-dependent Green's function as

$$\hat{\mathcal{G}}(i\omega,\tilde{\vec{k}}) = \left[i\omega\mathbf{1} - \hat{t}(\tilde{\vec{k}}) - \hat{\Sigma}(i\omega)\right]^{-1}. \tag{6.17}$$

A partial Fourier transform back to real space leads to

$$\hat{\mathcal{G}}\left(i\omega\right) = \frac{L}{N}\sum_{\vec{\tilde{k}}} \hat{\mathcal{G}}(i\omega, \vec{\tilde{k}}) = \hat{\mathcal{G}}_0\left(i\omega\mathbf{1} - \hat{\Sigma}(i\omega)\right). \tag{6.18}$$

This can be interpretated as the local Green's function of a two-impurity Anderson model with hybridization function

$$\hat{\Delta}(i\omega) = i\omega\mathbf{1} - \hat{t} - \hat{\Sigma}(i\omega) - \hat{\mathcal{G}}(i\omega)^{-1} = \hat{\Delta}_0\left(i\omega\mathbf{1} - \hat{\Sigma}(i\omega)\right). \tag{6.19}$$

The free hybridization function $\hat{\Delta}_0$ is given by

$$\hat{\Delta}_0(i\omega) = i\omega\mathbf{1} - \hat{t} - \hat{\mathcal{G}}_0(i\omega)^{-1}. \tag{6.20}$$

$\hat{t}$ is the cluster hopping matrix defined by

$$\hat{t} = \begin{bmatrix} 0 & -t \\ -t & 0 \end{bmatrix}. \tag{6.21}$$

To apply our fRG scheme the two-impurity Anderson model must have the form of a two-chain ladder as shown in Fig. D.1 with Hamiltonian (D.1). To determine the parameters of the two-chain ladder we fit the eigenvalues of the free hybridization function, $\Delta_0^{(1)}(i\omega)$ and $\Delta_0^{(2)}(i\omega)$, to a discretized hybridization function of the form

$$\Delta_0^{N,(i)}(i\omega) = \sum_{i=1}^{N} \frac{|v_i|^2}{i\omega - \epsilon_i}, \tag{6.22}$$

where the fit-parameters v_i and ϵ_i are calculated by a conjugate gradient minimization [GKKR96] of the distance function

$$d = \frac{1}{\omega_{\max}} \sum_{\omega} |\Delta_0^{(i)}(i\omega) - \Delta_0^{N,(i)}(i\omega)|^2. \tag{6.23}$$

Note that the fit-parameters for the two eigenvalues are not independent because it is $\Delta_0^{(2)}(i\omega) = -\Delta_0^{(1)}(i\omega)^*$, which is a consequence of particle-hole symmetry and can be deduced from Eq. (2.58). The finite bath can then be transformed to a tridiagonal form by the Lanczos algorithm, which determines the hopping-parameters of the two-chain ladder (cf. chapter 4.1.1).

6.3 Results

6.3.1 Single-site DMFT

First let us discuss the results for using the hybridization flow as DMFT solver for the case of single-site DMFT, embedded in a Bethe lattice. We show that the approach can reasonably describe both the insulating as well as the metallic phase, and give results for the effective interaction vertices in these phases.

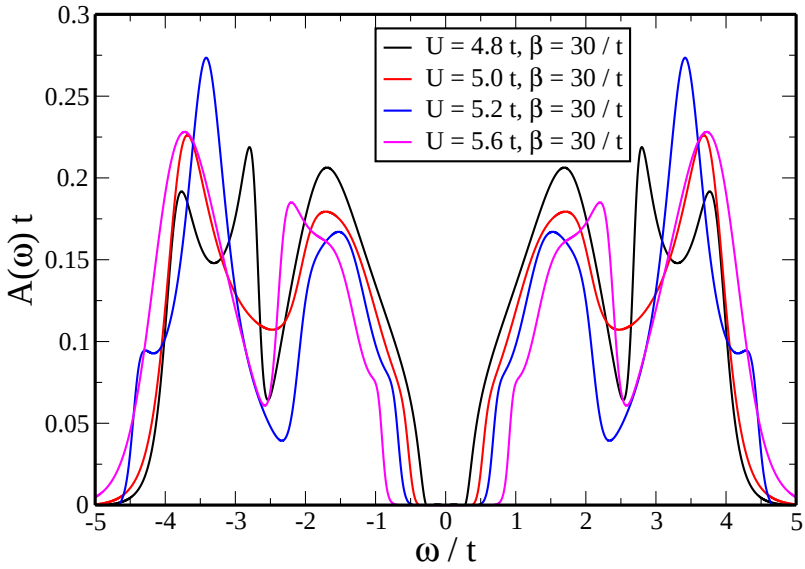

Figure 6.8: Spectral density in the insulating phase for $U = 4.8t, 5t, 5.2t, 5.6t$ at $\beta = 30/t$. At $\omega = 0$ a Mott-gap opens with an average center-to-center separation of the two Hubbard bands of $\sim U$.

Insulating phase

From our numerical data for the self-energy on the Matsubara frequency axis we obtain the spectral density $A(\omega) = -\frac{1}{\pi}\mathrm{Im}\,\mathcal{G}(\omega + i0^+)$ by an analytical continuation using a Padé-algorithm. The spectral density for several values of U/t is shown in Fig. 6.8. One obtains an opening of a Mott-gap arround $\omega = 0$ with an average center-to-center separation of the two Hubbard bands of $\sim U$. The width of the Hubbard bands for these moderate U-values is only a little smaller than the band width of the non-interacting problem, $W = 4t$. The rich multi-peak structure of the Hubbard bands (with a variable number of maxima) is propably an artifact of our approximation, most likely due to the discrete core used in the initial condition of the flow equation.

Next let us discuss the frequency structure of the local, 1PI interaction vertex at the converged DMFT solution as it comes out of the fRG flow that embeds the core into the lattice. In Fig. 6.9 we show the density part of this 1PI local vertex, $|\gamma_d(i\omega_1, i\omega_2|i\omega_1 - i\nu, i\omega_2 + i\nu) - U/2|$, and the magnetic part, $|\gamma_m(i\omega_1, i\omega_2|i\omega_1 - i\nu, i\omega_2 + i\nu) + U/2|$, for $U = 5t$ and $\beta = 30/t$ as functions of the incoming frequencies ω_1 (x-axis) and ω_2 (y-axis). The decomposition of the general vertex into density and magnetic part is described in chapter 2.3.4, in Eqs. (2.55) and (2.56). The outgoing frequencies are parametrized by the bosonic Matsubara frequency ν and we show the two cases $\nu = 0$ and $\nu = 40\frac{\pi}{\beta}$. To visualize the

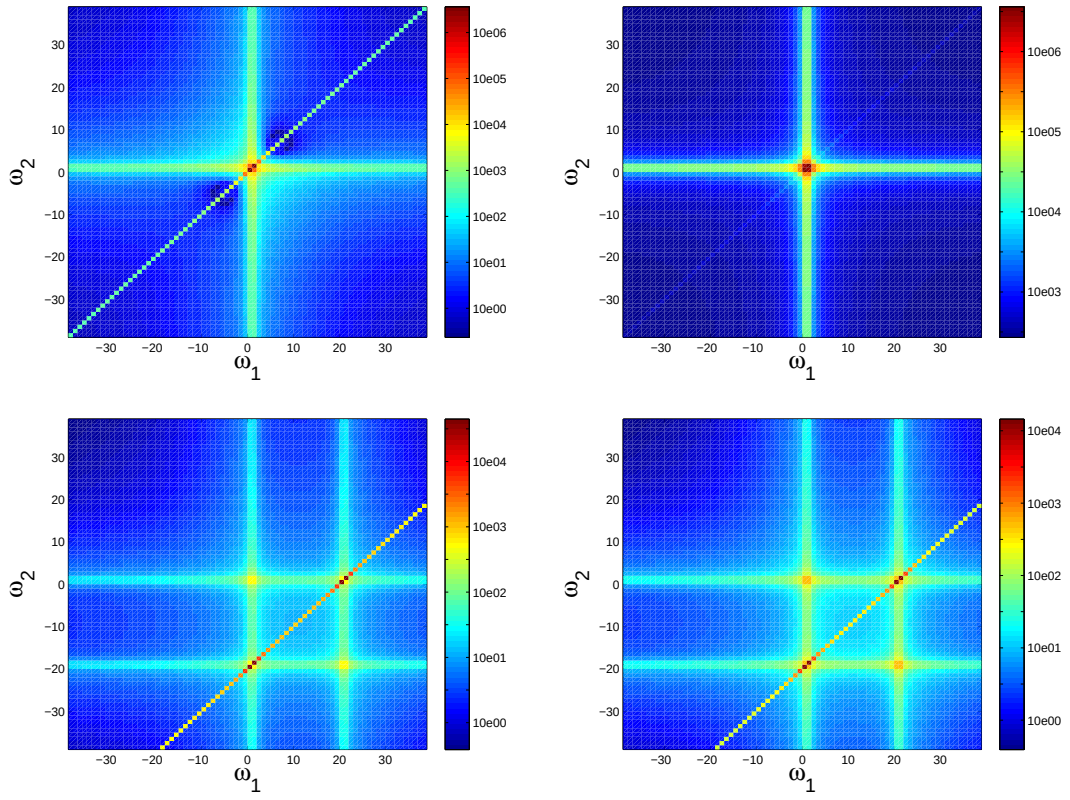

Figure 6.9: Absolute values of the vertex functions for $U = 5t$, $\beta = 30/t$. Density part $|\gamma_d(i\omega_1, i\omega_2|i\omega_1 - i\nu) - U/2|$ (left) and magnetic part $|\gamma_m(i\omega_1, i\omega_2|i\omega_1 - i\nu) + U/2|$ (right). Upper panel: $\nu = 0$, Lower panel: $\nu = 40\frac{\pi}{\beta}$. The frequencies are signed by their Matsubara index.

frequency structure better we subtracted the frequency independent term $U/2$ $(-U/2)$ from the density (magnetic) part. Because of particle-hole symmetry the vertices are purely real (cf. Eq. (2.59)). As explained in appendix C they are mirror-symmetric with respect to the lines A: $\omega_2 = \omega_1 - \nu$ and B: $\omega_2 = -\omega_1$.

Note that the connected part of the dynamic charge and spin susceptibilities $\chi^{\text{charge/spin},c}(i\nu)$ is obtained from the connected two-particle Green's function $\mathcal{G}^{c,(2)}_{d/m}(i\omega_1, i\omega_2|i\omega_1 - i\nu, i\omega_2 + i\nu)$ by summations with respect to ω_1 and ω_2 (cf. appendix A, Eqs. (A.3) and (A.8)). $\mathcal{G}^{c,(2)}_{d/m}$ and $\gamma_{d/m}$ are connected by Eq. (2.37), from which follows that the frequency structure of $\gamma_{d/m}$ determines the local charge and spin response of the system.

The main features of the obtained frequency structure correspond to those that are already visible in the single-site Hubbard vertex (B.7) and (B.8) at half filling that describes the response of a free spin 1/2. This is of course expected, because the insulating phase in the single-site DMFT is given by a paramagnetic insulator with local uncoupled spin degrees of freedom.

In all vertices of Fig. 6.9 one recognizes a sharply peaked diagonal structure for $\omega_2 =$

$\omega_1 - \nu$. In the single-site Hubbard vertex (B.7) and (B.8) this corresponds to the term proportional to $\delta_{\omega_2,\omega_{1'}}$. In the DMFT vertex it remains very sharp and no broadening is observed. As discussed in Ref. [RVT12] it diverges in the Mott phase for $T \to 0$, which explains the strong enhancement of this structure.
The first δ-term in the single-site Hubbard vertex (B.7) and (B.8), which is proportional to $\delta_{\omega_1,-\omega_2}$, would lead to an additional peak structure on the secondary diagonal in the ω_1, ω_2-plane. But for repulsive interactions $U > 0$ it is exponentially suppressed already for the single-site and also in the DMFT vertex no such structure is obtained.
The last term in the single-site Hubbard vertex (B.7) and (B.8) proportional to $\delta_{\omega_1,\omega_{1'}}$ only gives a contribution for $\nu = 0$. In the density part this contribution is not visible, because this term is again exponentially suppressed. In the magnetic part it is finite and occurs in the DMFT vertex as large difference in the offset between $\nu = 0$ and $\nu \neq 0$ (right column of Fig. 6.9). This difference leads to a term $\propto \delta_{\nu,0}$ in the spin-susceptibility, which will be discussed further below.
Furthermore there is a $+$-shaped cross structure in the DMFT vertex, that is centered at $(\omega_1 = 0, \omega_2 = 0)$ (for $\nu = 0$). At nonzero $\nu = 40\frac{\pi}{\beta}$ four of those structures can be found, centered at $(0,0)$, $(-\nu,0)$, $(-\nu,\nu)$ and $(0,\nu)$. In the local Hubbard vertex these correspond to the terms proportional to U^3 and U^5.
Summarizing these observations we can state that the 1PI interaction vertex is by no means a simple object. At least for this insulating regime it appears difficult to parametrize the vertex in a simple way. In particular, the cross structures indicate that a parametrization in terms of bosonic transfer frequencies does not capture the vertex in all aspects. In order to see that these vertices make physical sense, we now compute the local dynamical spin susceptibility from the 1PI vertex, by Eq. (A.8). Due to our finite frequency patching (we included 100 positive Matsubara frequencies at $\beta = 30/t$) our results become inaccurate especially for large frequencies because of the different speed of convergence of the connected and the disconnected part of the susceptibility. Nevertheless we obtain reasonable results by an analytical continuation of our data at least at low frequencies. In Fig .6.10 we show the real part of the spin susceptibility on the Matsubara axis (the imaginary part vanishes due to particle-hole symmetry). Beside a continuous frequency dependence at nonzero frequencies we obtain an additional term proportional to $\delta_{\nu,0}$, which is characteristic for a free spin-degree of freedom. This feature is already visible in the spin susceptibility of the local Hubbard model (B.14). It does not occur in the imaginary part of the spin susceptibility on the real frequency axis, because this vanishes at $\omega = 0$ due to Im $\chi^{\text{spin}}(i\omega) = -\text{Im } \chi^{\text{spin}}(-i\omega)$. To obtain stable Padé-results from our data was only possible for a few set of parameters. This showed a broad spectrum of spin excitations with an onset of twice the single-particle gap in agreement with Ref. [RU09] or the data shown in Fig. 6.8. Note that in this single-site DMFT approach non-local collective spin excitations that should appear below the particle-hole continuum are not

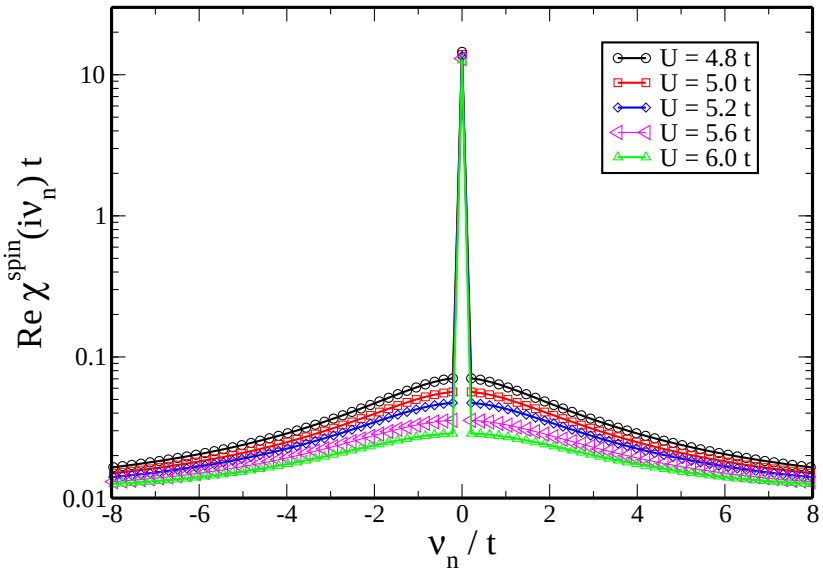

Figure 6.10: Real part of the Matsubara local spin susceptibility in the insulating regime of single-site DMFT(fRG) for $U = 4.8t, 5t, 5.2t, 5.6t, 6t$ at $\beta = 30/t$.

included.

Metallic phase

Next let us explore the results of single-site DMFT(fRG) for the metallic regime of the Bethe lattice Hubbard model, using the scheme presented in Subsection 6.2.2. In Fig. 6.11 we show the spectral density for $U = 1t, 2t, 3t$ at $\beta = 30/t$. In all cases we get only stable Padé-results for frequencies $|\omega| < 2t$. The spectral weight at $\omega = 0$ is pinned to the noninteracting value $A(\omega = 0) = \mathrm{DOS}(\omega = 0) = \frac{1}{\pi t}$, which is for $T = 0$ expected from Luttinger's theorem [MH89a, MH89b]. Here we find it also for nonzero temperature values. The shoulders at the side of the quasi-particle are located near the position of the low energy peaks at energies $\pm\frac{1}{4}\left(\sqrt{U^2 + 64z(U)v^2} - \sqrt{U^2 + 16z(U)v^2}\right)$ in the spectrum of the $L = 1$-core and remain as artifacts in the DMFT spectra (cf. the discussion in chapter 5.2).

In Fig. 6.12 the density part $\gamma_d(i\omega_1, i\omega_2|i\omega_1 - i\nu, i\omega_2 + i\nu) - U/2$ and the magnetic part $\gamma_m(i\omega_1, i\omega_2|i\omega_1 - i\nu, i\omega_2 + i\nu) + U/2$ of the 1PI vertex function for $U = 2t$ and $\beta = 30/t$ is shown. Again, the vertices are purely real due to particle-hole symmetry.

The main features of the frequency structure described above for the insulating phase are also visible in the metallic phase, but there are also certain differences. It can be clearly seen that now the vertices are continuos in the whole frequency plane and no sharp δ-like

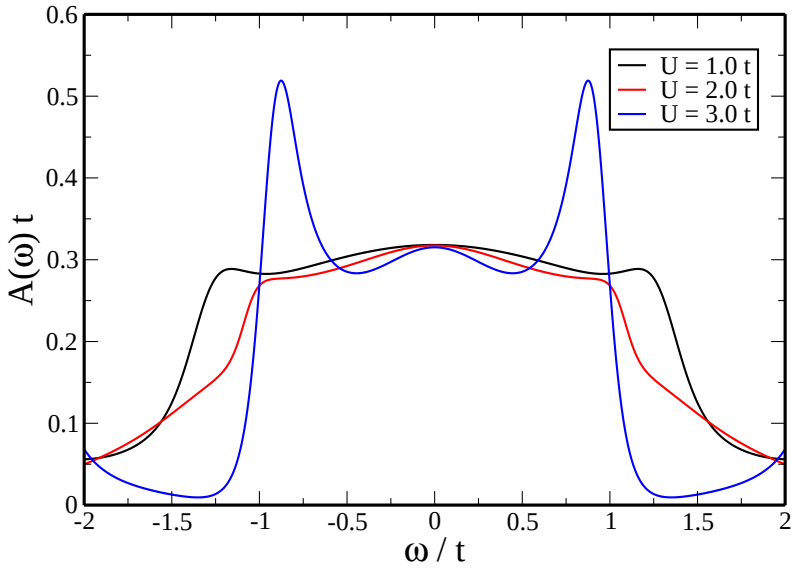

Figure 6.11: Spectral density for $U = 1t, 2t, 3t$ at $\beta = 30/t$. We get only stable Padé-results for $|\omega| < 2$. The kinks at the side of the quasi-particle peaks are located near the position of the low-energy peaks in the spectrum of the $L = 1$-core and remain as artifacts in the DMFT spectra.

features or singularities, as in the insulating phase, occur.
On the main diagonal at $\omega_2 = \omega_1 - \nu$ one observes again a pronounced structure, which is much more broadened compared to the insulating phase. In addition there is a similar structure on the secondary diagonal at $\omega_1 = -\omega_2$, which was absent in the insulating phase. As discussed in Ref. [RVT12] these features stem diagrammatically from particle-hole and particle-particle scattering processes respectively. Both are already visible in the vertices of the $L = 1$-core (cf. Fig. 6.13) and become only more pronounced in the fRG flow.
There is also a $+$-shaped structure at the same position as in the insulating phase. As seen in the lower panel of Fig. 6.12 this structure evolves into a band with width $|\nu|$ for $\nu = 40\frac{\pi}{\beta}$. In perturbation theory these structures correspond to third-order diagrams [RVT12], which involve mixing of particle-particle and particle-hole bubbles. No such structures occur in the vertices of the $L = 1$-core (Fig. 6.13). This means that they are generated entirely in the fRG flow that accomplishes the embedding into the lattice.
We compared our vertex data with DMFT(ED) vertices, calculated by the Vienna group [RVT12] for the same set of parameters (cf. Fig. 6.14). All described features are also visible in the frequency structure of the DMFT(ED) vertices and even their relative size and sign are qualitatively reproduced in our scheme. Quantitatively there are differences.

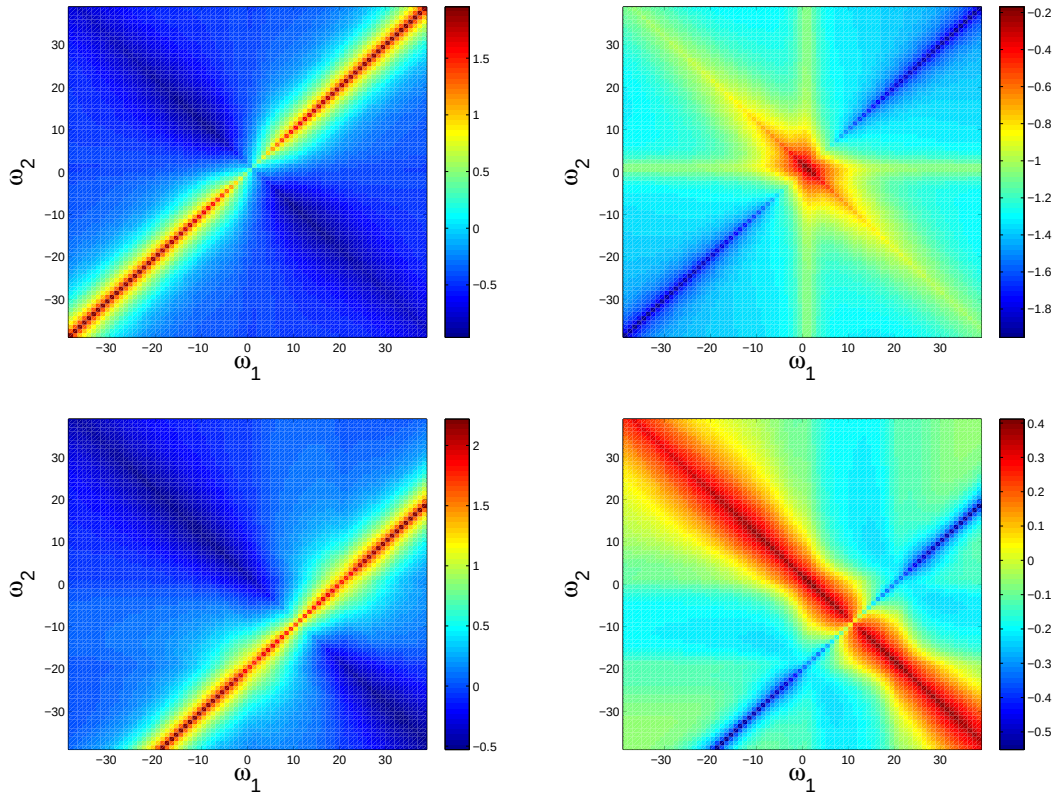

Figure 6.12: Vertex functions for $U = 2t$, $\beta = 30/t$. Density part $\gamma_d(i\omega_1, i\omega_2|i\omega_1 - i\nu) - U/2$ (left) and magnetic part $\gamma_m(i\omega_1, i\omega_2|i\omega_1 - i\nu) + U/2$ (right). Upper panel: $\nu = 0$, Lower panel: $\nu = 40\frac{\pi}{\beta}$. The frequencies are signed by their Matsubara index.

For example the vertical structure at $\omega_2 = \omega_1 - \nu$ is broadened and its absolute size comes out smaller in our scheme.

Summarizing the description of the single-site vertices, we can state that both in insulating as well as in the metallic state, the interaction vertices exhibit a lot of structure. The bosonic (diagonal) features could be captured by simpler parametrizations using functions depending on certain transfer frequencies only (cf. Ref. [KHP+08]), but other features like the +-structures would not be captured by that. In Ref. [RVT12] the decomposition of the 1PI vertex into two-particle irreducible (2PI) vertices and the fully irreducible vertex is discussed. We have reproduced this reasoning for some examples. In the 2PI vertices, certain bosonic features are removed, but other bosonic features due to the channel coupling remain, e.g. in the particle-particle 2PI vertices one still sees sharp features for specific frequency transfers that originate from particle-hole insertions. The fully irreducible vertex has a nontrivial frequency structure as well [RVT12, SRG+13].

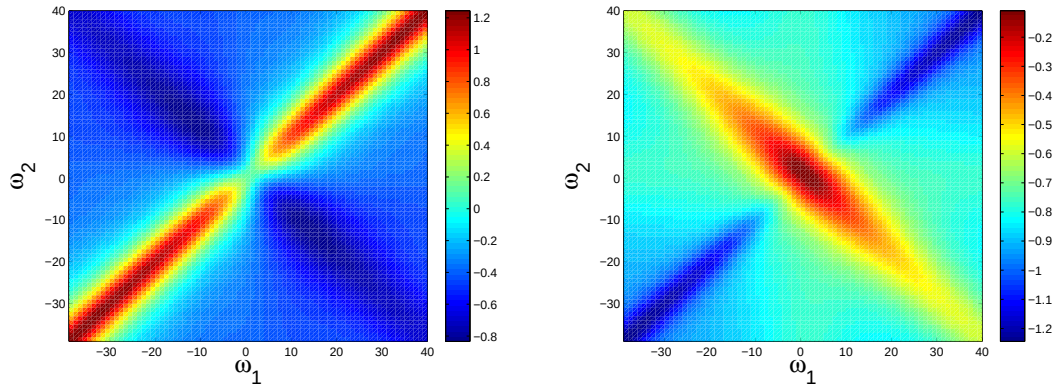

Figure 6.13: Vertex functions of the $L = 0$-core for $U = 2t$, $\beta = 30/t$. Density part $\gamma_d(i\omega_1, i\omega_2|i\omega_1) - U/2$ (left) and magnetic part $\gamma_m(i\omega_1, i\omega_2|i\omega_1) + U/2$ (right).

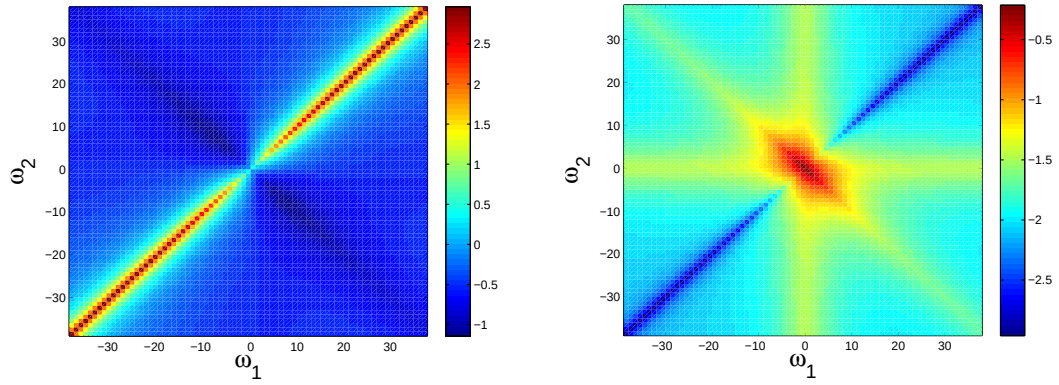

Figure 6.14: Vertex functions from DMFT(ED) for $U = 2t$, $\beta = 30/t$, calculated by the Vienna group [RVT12]. Density part $\gamma_d(i\omega_1, i\omega_2|i\omega_1) - U/2$ (left) and magnetic part $\gamma_m(i\omega_1, i\omega_2|i\omega_1) + U/2$ (right).

6.3.2 Two-site cluster DMFT

In Fig. 6.15 we show the local spectral density $A(\omega) = -\frac{1}{\pi}\mathrm{Im}\ \mathcal{G}_{ii}(\omega + i0^+)$ for $U = 4t$ and $U = 10t$ at $\beta = 30/t$. Unlike for the single-site DMFT(fRG) scheme, using the two-site cluster as core, we can describe metallic and insulating behaviour with the same fRG scheme, without having to parametrize the self-energy by a Z-factor. For $U = 10t$ we find an insulating spectrum with two Hubbard bands at $\omega = \pm 5t$ separated by a gap. In the metallic spectrum for $U = 4t$ these Hubbard bands are still visible as weakly pronounced shoulders at $\omega = \pm 2t$. The sharp peak at $\omega = 0$ is due to the van Hove singularity in the free density of states of the two-dimensional square lattice. Hence the single-particle spectra are qualitatively correct and show the expected energy scales. This gives us a robust starting point for studying the 1PI interaction vertex for the two-site core, now including its non-local part.

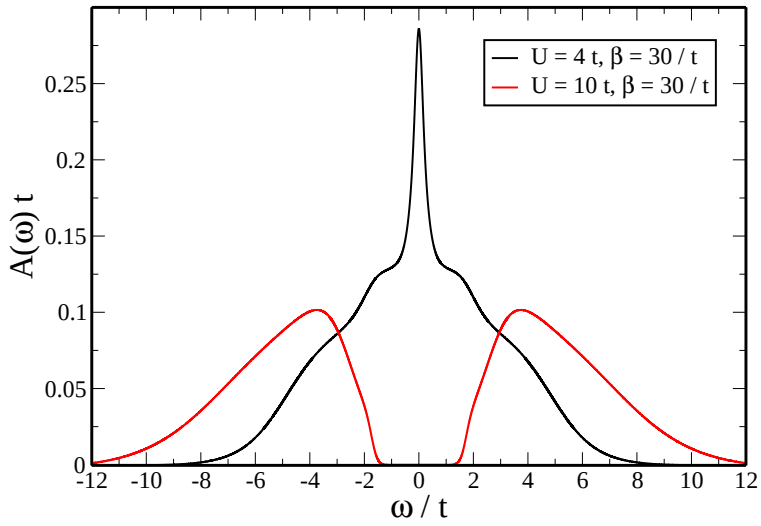

Figure 6.15: Local single-particle spectral density $A(\omega) = -\frac{1}{\pi}\mathrm{Im}\ \mathcal{G}_{ii}(\omega + i0^+)$ for $U = 4t$ and $U = 10t$ at $\beta = 30/t$, obtained by two-site cluster DMFT(fRG).

As for the single-site DMFT, we discuss the frequency structure of the 1PI vertex functions for the insulating and the metallic phase in terms of the density and magnetic parts. Note that in units of the bandwidth W, the onsite interaction U is in both cases the same as in the data shown for the single-site DMFT. Therefore, the vertices can be directly compared to each other on the energy axis[1]. Opposite to the single-site DMFT, the two-site cluster DMFT includes antiferromagnetic fluctuations between neighbored sites. These should characterized by the energy scale J that is for large U given by $J \sim 4\frac{t^2}{U}$.
By the Fourier transformation $U_{\vec{K}_i,\vec{R}_j} = \frac{1}{\sqrt{2}}\exp(i\vec{K}_i\vec{R}_j)$ we transform the vertices to cluster momentum space with the cluster momenta $\vec{K}_1 = (0,0)$ and $\vec{K}_2 = (\pi,\pi)$. $\vec{R}_1 = (0,0)$ and $\vec{R}_2 = (0,1)$ are shown in Fig. 6.6. Due to momentum conservation the only non-negative contributions are given by

$$\begin{aligned}
\Gamma_{d/m}(\vec{K}_1, i\omega_1; \vec{K}_1, i\omega_2 | \vec{K}_1, i\omega_{1'}; \vec{K}_1, i\omega_{2'}) &\equiv \Gamma^{1111}_{d/m}(i\omega_1; i\omega_2 | i\omega_{1'}; i\omega_{2'}),\\
\Gamma_{d/m}(\vec{K}_1, i\omega_1; \vec{K}_2, i\omega_2 | \vec{K}_1, i\omega_{1'}; \vec{K}_2, i\omega_{2'}) &\equiv \Gamma^{1212}_{d/m}(i\omega_1; i\omega_2 | i\omega_{1'}; i\omega_{2'}),\\
\Gamma_{d/m}(\vec{K}_1, i\omega_1; \vec{K}_2, i\omega_2 | \vec{K}_2, i\omega_{1'}; \vec{K}_1, i\omega_{2'}) &\equiv \Gamma^{1221}_{d/m}(i\omega_1; i\omega_2 | i\omega_{1'}; i\omega_{2'}),\\
\Gamma_{d/m}(\vec{K}_1, i\omega_1; \vec{K}_1, i\omega_2 | \vec{K}_2, i\omega_{1'}; \vec{K}_2, i\omega_{2'}) &\equiv \Gamma^{1122}_{d/m}(i\omega_1; i\omega_2 | i\omega_{1'}; i\omega_{2'})
\end{aligned}$$

and the same quantities with $\vec{K}_1 \leftrightarrow \vec{K}_2$ respectively. Due to particle-hole symmetry one

[1]To be more precise, one should compare the ratio $\frac{U}{\sigma}$, where σ is the standard deviation of the noninteracting density of states. Anyhow, one has $\sigma = t$ for the Bethe lattice and $\sigma = 2t$ for the two-dimensional square lattice, so that both criteria are equivalent in our case.

Table 6.1: In the $\omega_1 - \omega_2$-plane there are two symmetry axes: (A) at $\omega_2 = \omega_1 - \nu$ and (B) at $\omega_1 = -\omega_2$ with the corresponding mirror operators M_A and M_B respectively. In the table we show the transformation behaviour of $\Gamma^{\#_1\#_2\#_3\#_4}_{d/m}(i\omega_1; i\omega_2|i\omega_1 - i\nu; i\omega_2 + i\nu)$ under M_A and M_B.

	M_A	M_B
$\Gamma^{1111}_{d/m}$	$\Gamma^{1111}_{d/m}$	$\left(\Gamma^{1111}_{d/m}\right)^*$
$\Gamma^{1212}_{d/m}$	$\left(\Gamma^{1212}_{d/m}\right)^*$	$\Gamma^{1212}_{d/m}$
$\Gamma^{1221}_{d/m}$	$\Gamma^{1221}_{d/m}$	$\Gamma^{1221}_{d/m}$
$\Gamma^{1122}_{d/m}$	$\left(\Gamma^{1122}_{d/m}\right)^*$	$\left(\Gamma^{1122}_{d/m}\right)^*$

has $\Gamma^{2222}_{d/m} = \left(\Gamma^{1111}_{d/m}\right)^*$, $\Gamma^{2121}_{d/m} = \left(\Gamma^{1212}_{d/m}\right)^*$, $\Gamma^{2112}_{d/m} = \left(\Gamma^{1221}_{d/m}\right)^*$ and $\Gamma^{2211}_{d/m} = \left(\Gamma^{1122}_{d/m}\right)^*$. Hence we can restrict the discussion to the former vertices.

If we plot $\Gamma^{\#_1\#_2\#_3\#_4}_{d/m}(i\omega_1; i\omega_2|i\omega_1 - i\nu; i\omega_2 + i\nu)$ in the $\omega_1 - \omega_2$-plane we have the symmetry axes (A) at $\omega_2 = \omega_1 - \nu$ and (B) at $\omega_1 = -\omega_2$. M_A and M_B are mirror operators at axis (A) and (B) respectively. In Table 6.1 we show the transformation behaviour of $\Gamma^{1111}_{d/m}$, $\Gamma^{1212}_{d/m}$, $\Gamma^{1221}_{d/m}$ and $\Gamma^{1122}_{d/m}$ under M_A and M_B which follows from time-reversal symmetry and particle-hole symmetry (cf. appendix C). For $\nu = 0$ one can furthermore show that $\Gamma^{1221}_{d/m} \in \mathbb{R}$ and $\Gamma^{1122}_{d/m} \in \mathbb{R}$. In presenting the data, we will restrict the discussion to the case of zero transfer frequencies ν, either for the charge or the magnetic channel. Based on the experience from the single-site vertex, this data contains the main features, which would get shifted or split, but not changed drastically in the case of finite frequency transfer.

Insulating phase

In Fig. 6.16 we show the vertices $|\Gamma^{1111}_{d/m}(i\omega_1; i\omega_2|i\omega_1; i\omega_2) \mp U/4|$, $|\Gamma^{1212}_{d/m}(i\omega_1; i\omega_2|i\omega_1; i\omega_2) \mp U/4|$, $\Gamma^{1221}_{d/m}(i\omega_1; i\omega_2|i\omega_1; i\omega_2) \mp U/4$ and $\Gamma^{1122}_{d/m}(i\omega_1; i\omega_2|i\omega_1; i\omega_2) \mp U/4$ for $U = 10t$ and $\beta = 30/t$. Since Γ^{1111} and Γ^{1212} are complex-valued we plot their absolute values.

In the density and magnetic part of Γ^{1111} and Γ^{1221}, the only apparent feature is a $+$-shaped structure, which reaches its maximum in the center at $(\omega_1 = 0, \omega_2 = 0)$. It is much more broadened compared to the single-site DMFT (Fig. 6.9) and its width increases with the interaction U.

The density and magnetic part of Γ^{1212} and Γ^{1122} are dominated by a peaked diagonal frequency structure at $\omega_1 = \omega_2$, which reaches its maximum at $(\omega_1 = 0, \omega_2 = 0)$. Except for the magnetic part of Γ^{1122}, an additional $+$-shaped structure is only very weakly pronounced. Snapshots of the peaked structure at $\omega_1 = \omega_2$ along or parallel to the main diagonal can be described by a Lorentzian with width $\approx J$. This should be compared to the local vertex of the single-site DMFT (cf. Fig. 6.9). Here the antiferromagnetic coupling J is absent and also the peaked structure at $\omega_2 = \omega_1$ is δ-shaped, i.e. its width

Table 6.2: Spin excitation energies $\Delta E_{11}^{\text{spin}}$ and $\Delta E_{12}^{\text{spin}}$ obtained from the data in Fig. 6.17 in comparison with the two-site Hubbard model $\Delta E_{\text{2-site}}^{\text{spin}} = J_{\text{2-site}} = \left(\sqrt{U^2+16t^2}-U\right)/2$.

U/t	$\Delta E_{11}^{\text{spin}}/t$	$\Delta E_{12}^{\text{spin}}/t$	$\Delta E_{\text{2-site}}^{\text{spin}}/t$
10	0.351	0.357	0.385
12	0.310	0.316	0.325
14	0.274	0.280	0.280

is equal to zero. This difference is mainly caused by the fact that in the two-site core, the localized spins couple antiferromagnetically and form a singlet. The embedding of this core in the gapped bath only leads to quantitative changes, but without allowing for longer-ranged spin correlations in this cluster DMFT framework, the singlet character does not change. Therefore, qualitatively, the important features in the frequency structure of the embedded vertex are already visible in the vertex of the isolated two-site Hubbard model, which serves as core in our cluster DMFT scheme. Hence, if one tries to describe a short-range correlated system, using a finite-site vertex of a core with qualitatively similar properties may be a good approximation or guide to look for viable parametrizations. Near phase transitions the picture may become more complicated [RTKH11].

In Fig. 6.17 we show the local and next-neighbor spin susceptibilities on the Matsubara axis. In contrast to the single-site DMFT (cf. Fig. 6.10) no term $\propto \delta_{\nu,0}$ occurs in the local spin susceptibility, which was characteristic for a free spin degree of freedom. Now, the spin moments are screened by an antiferromagnetic exchange interaction. The Padé-spectra show sharp spin excitations at certain values $\pm\Delta E_{ij}^{\text{spin}}$ and the Matsubara data are consistent with a functional dependence of the form $\chi_{ij}^{\text{spin}}(i\nu) \sim (-1)^{(i-j)} \frac{\Delta E_{ij}^{\text{spin}}}{\nu^2+(\Delta E_{ij}^{\text{spin}})^2}$. The spin excitation energy in the two-site Hubbard model is given by $\Delta E_{\text{2-site,11}}^{\text{spin}} = \Delta E_{\text{2-site,12}}^{\text{spin}} = \Delta E_{\text{2-site}}^{\text{spin}} = \left(\sqrt{U^2+16t^2}-U\right)/2$ (corresponding to spin fluctuations between the ground state $|N=2;S=0;1\rangle$ and the triplet sector, compare appendix B.3). It is equal to the antiferromagnetic exchange energy $J_{\text{2-site}}$ in the corresponding two-site Heisenberg model. In Table 6.2 we present the fitted values $\Delta E_{11}^{\text{spin}}$, $\Delta E_{12}^{\text{spin}}$ and $\Delta E_{\text{2-site}}^{\text{spin}}$ for the data in Fig. 6.17. Not unexpectedly, the trend shows that for increasing insulating character, i.e. larger U, the excitation energies come closer to the value of the isolated two-site cluster.

Metallic phase

In Fig. 6.18 we show the vertices $|\Gamma_{d/m}^{1111}(i\omega_1;i\omega_2|i\omega_1;i\omega_2) \mp U/4|$, $|\Gamma_{d/m}^{1212}(i\omega_1;i\omega_2|i\omega_1;i\omega_2) \mp U/4|$, $\Gamma_{d/m}^{1221}(i\omega_1;i\omega_2|i\omega_1;i\omega_2) \mp U/4$ and $\Gamma_{d/m}^{1122}(i\omega_1;i\omega_2|i\omega_1;i\omega_2) \mp U/4$ for $U = 4t$ and $\beta = 30/t$, i.e. in the metallic phase.

Compared to the insulating phase, the obtained frequency structures are now even richer. The density and magnetic parts of Γ^{1111} and the density part of Γ^{1221} are beyond a

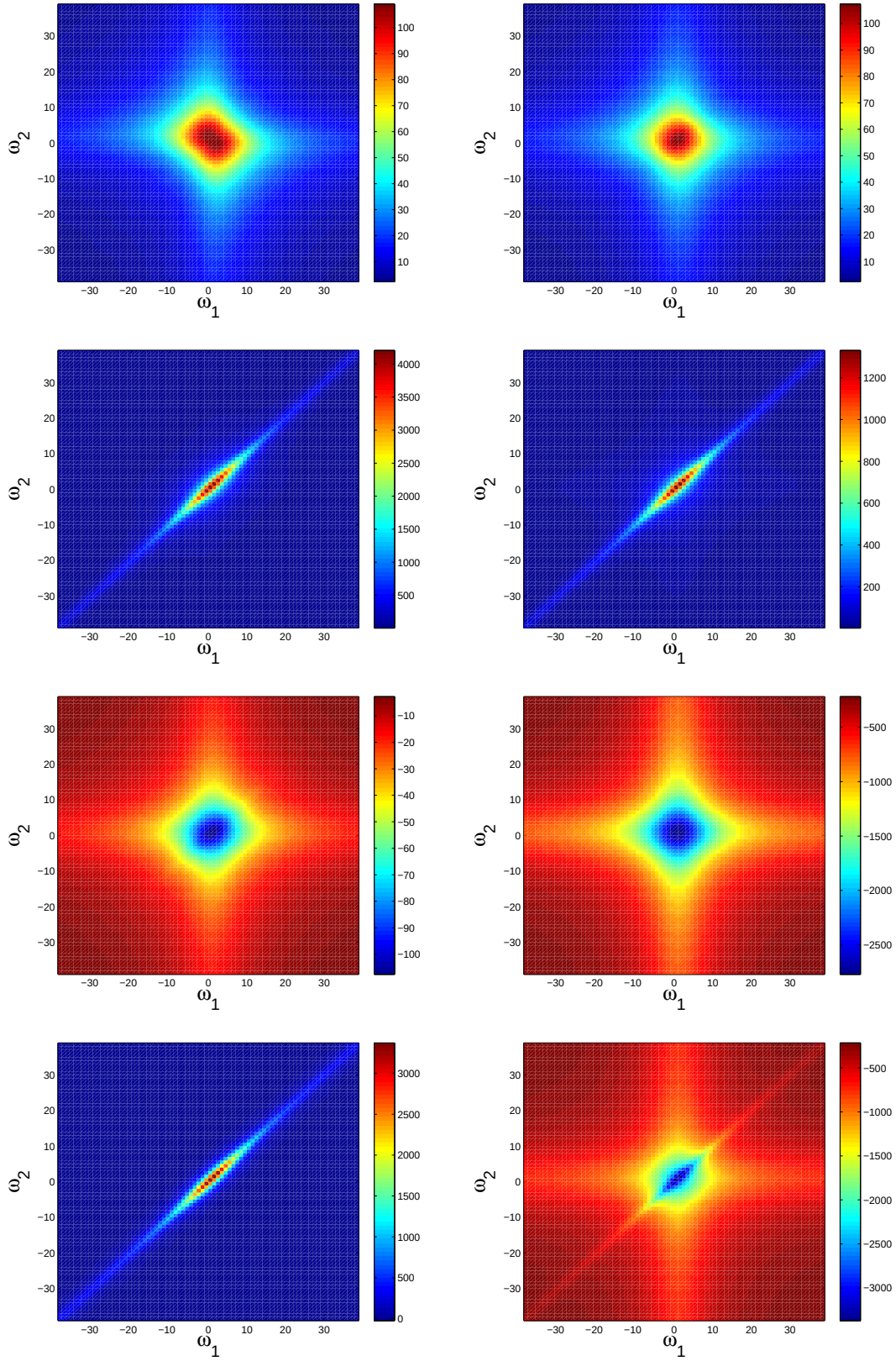

Figure 6.16: Vertex functions $|\Gamma^{1111}_{d/m}(i\omega_1; i\omega_2|i\omega_1; i\omega_2) \mp U/4|$, $|\Gamma^{1212}_{d/m}(i\omega_1; i\omega_2|i\omega_1; i\omega_2) \mp U/4|$, $\Gamma^{1221}_{d/m}(i\omega_1; i\omega_2|i\omega_1; i\omega_2) \mp U/4$ and $\Gamma^{1122}_{d/m}(i\omega_1; i\omega_2|i\omega_1; i\omega_2) \mp U/4$ for $U = 10t$, $\beta = 30/t$, obtained in two-site cluster DMFT(fRG). Left column: density part. Right column: magnetic part. The frequencies are signed by their Matsubara index.

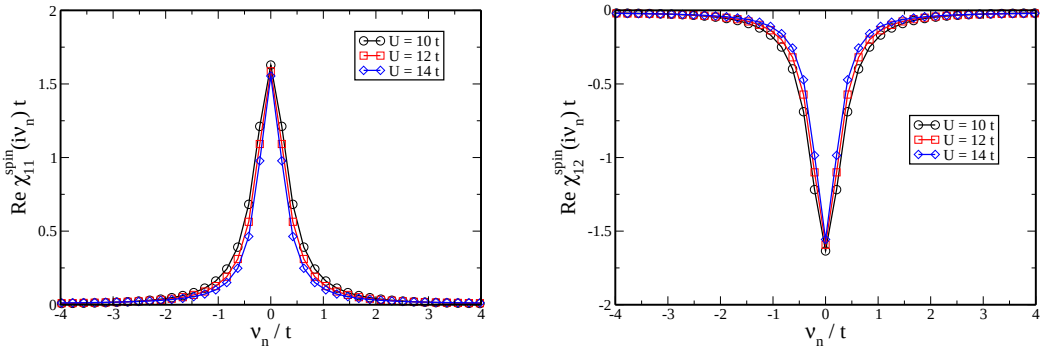

Figure 6.17: Spin susceptibility $\chi^{\text{spin}}_{ij}(i\nu)$ on the Matsubara axis, obtained in the insulating regime of the two-site cluster DMFT(fRG) for the Hubbard model on the square lattice. Left plot: local spin susceptibility. Right plot: next-neighbor spin susceptibility.

simple description and posses rather detailed structures along the $\omega_1 = \omega_2$ and $\omega_1 = -\omega_2$ lines, overlaid by an additional +-shaped structure. Opposite to the insulating case, the vertices become minimal in their absolute values at this +-shaped structure, especially at the point $(\omega_1 = 0, \omega_2 = 0)$, rather than reaching a maximum. This is best visible in the magnetic part of Γ^{1221}, which is determined solely by this structure. Except to this different behaviour at the +-shaped structure, the vertices Γ^{1212} and Γ^{1122} are similar to the corresponding vertices in the insulating phase.

6.3.3 Summary of the vertex analyis

Quite generally, our data supports the findings of Ref. [RVT12] that the vertices show rich structure, including +-structures that cannot be parametrized in terms of the "bosonic" transfer frequencies. While the physical meaning of these structures beyond a connection to higher-order diagrams is not obvious, they represent a formidable challenges for the above mentioned approaches that want to use the DMFT vertices as input in order to explore correlations on longer scales, in particular if wave vector dependencies are supposed to be added. Beyond this principal statement, we can use our data to make two valuable comparisons. First we can study the *a)* difference between the vertices in the metallic and the insulating phase. Second we can *b)* scrutinize what changes occur when non-local correlations are included.

Regarding comparison *a)*, we find much milder frequency dependences in the metallic case. In particular, the sharp bosonic features of the single-site solution are smeared out, and the +-structures are broadened as well. Furthermore, many (but not all) cross sections of the vertices in the metallic phase show a reduction at low frequencies compared to high frequencies which points to a screening effect. In the insulating state, the opposite is found.

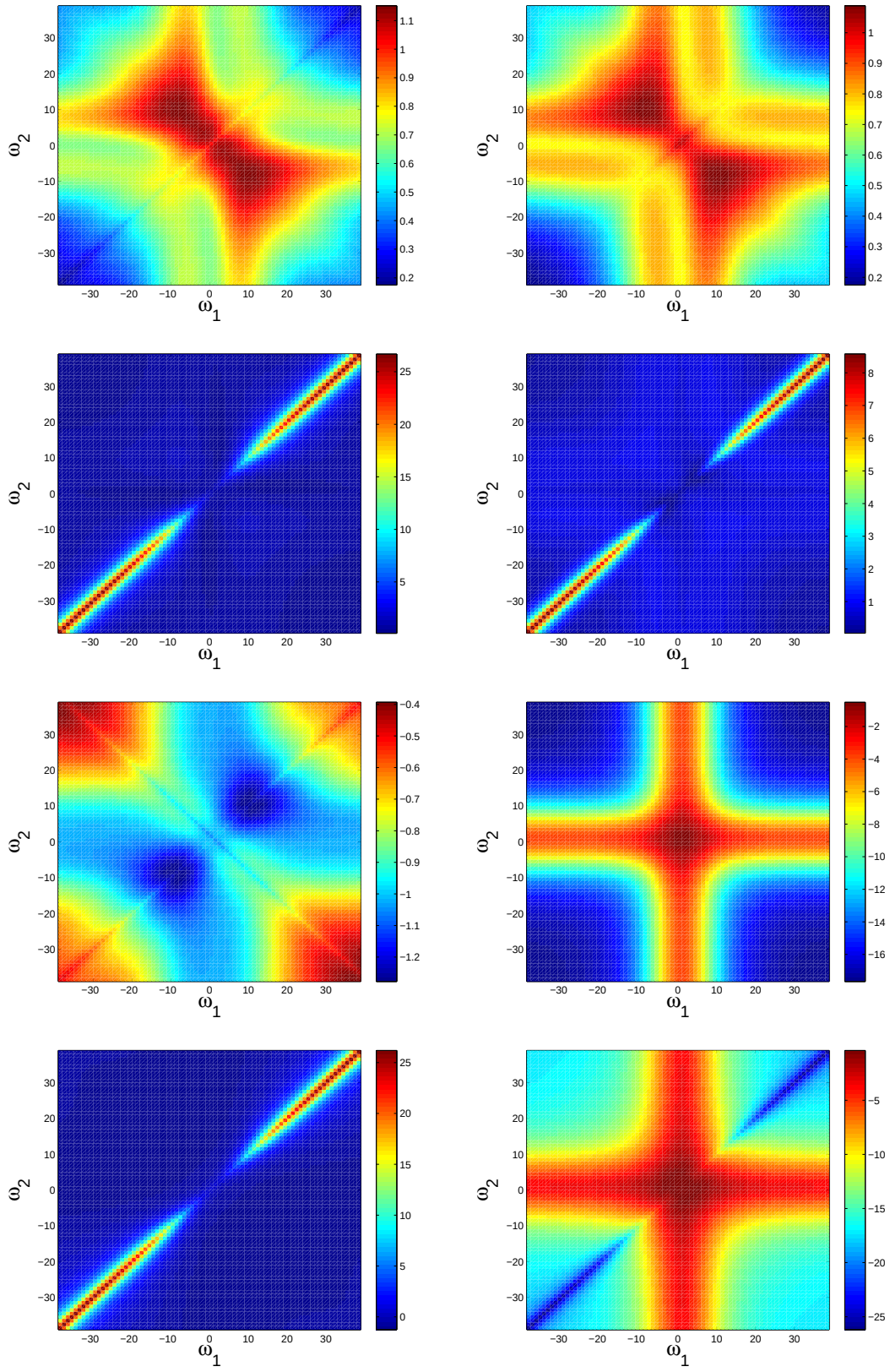

Figure 6.18: Vertex functions $|\Gamma^{1111}_{d/m}(i\omega_1; i\omega_2|i\omega_1; i\omega_2) \mp U/4|$, $|\Gamma^{1212}_{d/m}(i\omega_1; i\omega_2|i\omega_1; i\omega_2) \mp U/4|$, $\Gamma^{1221}_{d/m}(i\omega_1; i\omega_2|i\omega_1; i\omega_2) \mp U/4$ and $\Gamma^{1122}_{d/m}(i\omega_1; i\omega_2|i\omega_1; i\omega_2) \mp U/4$ for $U = 4t$, $\beta = 30/t$. Left column: density part. Right column: magnetic part. The frequencies are signed by their Matsubara index.

Here, the low frequency vertices are mostly enhanced. Finally, in the metallic phase of the single-site solution one can also find enhancement features at zero incoming frequency, pointing to the role of pairing fluctuations. These cannot be seen in the insulating state, and these features are also much weaker in the two-site solution, possibly due to the spin gap. Note that the possible soft collective fluctuations, which are not captured by the present cluster schemes, could lead to additional frequency structures. Their systematics should however be correspond to what is known from random-phase approximation or related approaches.

Comparison *b)* between single-site and two-site DMFT vertices shows on one hand that new features and energy scales can come in. Our data describes how the sharp diagonal features for fixed frequency transfer get broadened, and displays the exchange energy scale J. Beyond these expected changes, the frequency structures are definitely dispersive, as can be seen from the vertices for different wavevector combinations. From our work one can only see that non-local correlations have a definite effect on the vertices. However, we are far away from understanding how far one should go in the cluster size to obtain convergence, e.g., of the local vertex. Yet, at least for larger U, the behaviour on a nearest-neighbor bond captured in our results should contain the dominant strong coupling physics, unless phase transitions with diverging length scales or geometric frustration come into play.

To obtain the local dynamic charge and spin susceptibilites from our vertex data is more challenging due to the finite frequency patching and the different speed of convergence of the connected and disconnected parts of the susceptibilities, but we still managed to estimate effective exchange coupling from the data. Yet, the analytical continuation by a Padé-algorithm does not deliver meaningful results for all sets of parameters. One might try to achieve better results by an appropriate parametrization of the vertex function in the lines of Ref. [Ort]. Note, that frequency dependent vertex corrections are found to be essential for understanding experimentally observed dynamic susceptibilites in realistic material calculations, as for example in the case of iron-based superconductors [PHK11, TAH$^+$12, LHL$^+$12]. Therefore, there is a great need for developing new flexible solvers, which facilitate the heavy calculation of these quantities in realistic multi-orbital cases.

Chapter 7

Conclusion and outlook

In this thesis we developed a new renormalization group approach to the single impurity Anderson model, and showed that it can serve as an efficient and flexible impurity solver for the dynamical mean-field theory.

The starting point was the exact result for the one- and two-particle correlation functions of a small subsystem (core) containing the correlated impurity site. Then we tracked the evolution of these functions when the coupling to the bath is switched on slowly. In this way, the solution of the small isolated cluster was implemented exactly, and the flow generated changes of infinite order in the hybridization with the bath. The main approximation was the truncation of the flow equations after the two-particle vertex. In the present case this means that the change of the higher-order vertices (three-particle, four-particle, etc.) upon coupling to the bath is not allowed to influence the lower order vertices, i.e. the two-particle vertex and the self-energy. Yet, the idea that led us take this avenue was that starting with the exact self-energy and two-particle vertex of the small core contains enough strong correlation physics in order to give physically reasonable results. The local interaction physics, such as the atomic scales, were well represented in our approach. However, the Kondo effect requires to describe the subtle interplay with a continuum of states including many energy scales and our approach captured this only qualitatively, but not quantitatively.

In chapter 5 we applied our approach to the single impurity Anderson model with a semi-elliptic bath density of states. The numerical results for clusters with an odd number of sites ($L = 1$ and $L = 3$) showed that the flow equations produce qualitatively correct results, whereas for even numbers the Fermi liquid behaviour was not recovered. The dependence of the width of the Kondo peak on increasing U was quantitatively different from NRG results, i.e. the correct exponential dependence was not reproduced. For larger U the Kondo scale becomes smaller than the nonzero temperatures, for which the fRG scheme is feasible. Hence no clear statement could be made regarding the large-U behaviour. However, in the interesting intermediate coupling regime, the deviations may

be tolerable. In this sense, embedding this new impurity solver in a different context to describe itinerant and strongly coupled physics qualitatively correct (see discussion below) seems a viable possibility.

In comparison with other finite-frequency functional RG techniques, e.g. those that are perturbative in U, our data end up in the same range, as shown in Fig. 5.6. Since the ground state for weak and strong coupling remains the same, it is not entirely surprising that approaches starting at the opposite ends lead to qualitatively similar results. The quantitative agreement could potentially be interpreted as a measure of the error, that is introduced by the truncation after the two-particle vertex, which is common to both lines of approach. Note that in a recent paper Streib et al. [SIK13] were able to reproduce the exponential Kondo scale, using a fRG scheme with partial bosonization of the transverse spin-fluctations. By using Ward identities they were able to avoid further truncations of the flow equations. In this way they obtained the spin susceptibility and the effective mass in good agreement with the exact Bethe ansatz solution.

One could think of a possible generalization of our fRG method to correlated lattice systems (i.e. with more than one correlated site, like the two-dimensional Hubbard model). In this case, both self-energy and interaction vertex will become increasingly non-local during the flow, and suitable approximations would have to be found in order to keep the amount of information manageable. For example, small correlated cluster cores can be coupled together during the flow by switching on the hopping amplitude between the clusters from 0 to the original value. The solution of the core will then provide the spectral weight transfers on the energy scale U and the accompanying reduction of the spectral weight near the Fermi level. Together with the core interaction vertex, this spectrum will serve as an effective action of a strongly correlated Fermi liquid, which then can undergo a longrange ordering transition when the cores are coupled together. Note that in extension of earlier ideas in the vein of cluster perturbation theory (see, e.g. Refs. [GV93, SPP02]), the fRG scheme also allows one to determine the non-local hybridization effects on the interaction, which has direct consequences for the character and scale of low-temperature instabilities such as unconventional superconductivity. This way one could possibly extend the successful functional RG instability analysis for weakly correlated fermions to the more strongly correlated regime. The high-energy physics of a strongly interacting Hubbard-like system is certainly more local than the low-energy physics of collective ordering. Hence, the break-up into small cores and subsequent coupling together also closely follows the physical intuition of first solving the problem with the largest energy scale before the low-energy end is considered. One approach that follows this direction is the recently proposed DMF^{2}RG method [TAB$^+$13]. Here, starting from the local DMFT solution of the two-dimensional Hubbard model, non-local correlations are built in via the functional renormalization group. This way, divergences of the two-particle vertex, that occur in weak-coupling fRG, are shifted to lower temperatures and also non-local

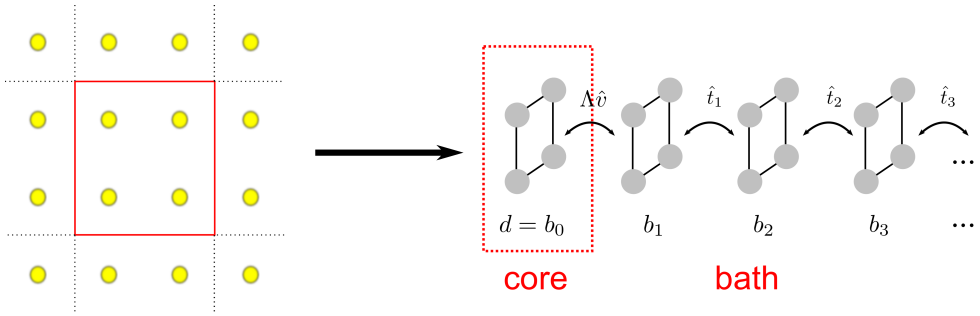

Figure 7.1: Extension of our cluster DMFT scheme to four-site clusters.

corrections to the DMFT self-energy are found.

In chapter 6 we demonstrated that our hybridization flow scheme can serve as a fast and numerically inexpensive impurity solver in the DMFT setup. Using this new impurity solver, we studied at first the half-filled Hubbard model on a Bethe lattice in infinite dimension. We were able to reproduce the hallmarks of metallic and insulating phases, although the transition region could not be resolved very clearly, at least with the current implementation. While we think that it is interesting and important to explore new impurity solvers, we certainly do not claim that the current version of the hybridization flow impurity solver is superior to established techniques with respect to single-particle properties. However, a quantity that has not been investigated thoroughly in the past but that is quite easily accessible in the fRG impurity solver is the local 1PI vertex function. It explicitly appears in the fRG solution of the impurity problem and is hence obtained at no additional cost. We obtained its density and magnetic part for the insulating and the metallic phase in good qualitative agreement with recent calculations using DMFT with exact diagonalization as impurity solver [RVT12]. Understanding the frequency structure of this vertex function in DMFT is important for several reasons. On the one hand it is an important ingredient of perturbative DMFT extensions, that include non-local degrees of freedom [SK04, TKH07, HKT08, RKL08, RKLG09, RTH$^+$13, TAB$^+$13], but also in the single-site DMFT two-particle correlation functions can be used to identify nonperturbative precursors of the Mott physics inside the metallic phase of the MIT [SRG$^+$13]. Furthermore the frequency-structure of the two-particle interaction is important for realistic material calculations, where the bare Hubbard U already gains a frequency-dependence due to screening effects [ATMS09]. This additional frequency-dependence strongly influences the single-site DMFT results [WM10]. Note that there are further ways to separate the 1PI vertex into other parts, like the fully irreducible vertex and 2PI vertices, see Ref. [RVT12]. As shown in this reference, these other vertices show slightly reduced complexity in their frequency structures, but also remain nontrivial functions of the frequencies. In order to keep the discussion manageable, we have not taken this road and only presented data for the 1PI vertex.

Since we got reasonable results in the single-site case, we extended our scheme to a two-site cluster DMFT approach and studied the two-dimensional Hubbard model on a square lattice. In this case, antiferromagnetic fluctuations between nearest neighbor sites are included. We obtained the density and magnetic part of the cluster vertex functions for the insulating and the metallic phase. From the local and next-neighbor spin susceptibility we obtained the spin-spin coupling J as function of U in the insulating phase. This exchange energy could also be identified in the frequency structure of the cluster vertices.

A possibility for a future project would be to use our hybridization flow scheme as impurity solver in a four-site cluster DMFT calculation (cf. Fig. 7.1), although calculating the initial two-particle Green's function for the four-site cluster requires already a huge amount of numerical effort [RVT12, Lui12].

Appendix A

Dynamic susceptibilities

A.1 charge susceptibility

The dynamic charge-susceptibility is defined as the Fourier-transform of the density-density correlation function

$$\chi_{ij}^{\text{charge}}(i\nu) = \int_0^\beta \mathrm{d}\tau \mathrm{e}^{i\nu\tau} \left[\langle T_\tau \hat{\rho}_i(\tau)\hat{\rho}_j(0)\rangle - \langle\hat{\rho}_i\rangle\langle\hat{\rho}_j\rangle\right] \tag{A.1}$$

with the density-operator

$$\hat{\rho}_i = \sum_\sigma c_{i\sigma}^\dagger c_{i\sigma}. \tag{A.2}$$

The expectation-value can be written as sum over a two-particle Green's function

$$\begin{aligned}
\chi_{ij}^{\text{charge}}(i\nu) =& \int_0^\beta \mathrm{d}\tau \mathrm{e}^{i\nu\tau} \sum_{\sigma,\sigma'} \mathcal{G}^{(2)}\left(i,\sigma,\tau;j,\sigma',0^-|i,\sigma,\tau;j,\sigma'\right) - \beta\delta_{\nu,0}\langle\hat{\rho}_i\rangle\langle\hat{\rho}_j\rangle \\
=& \frac{1}{\beta^2}\sum_{i\omega_1,i\omega_2}\sum_{\sigma,\sigma'} \mathcal{G}^{(2)}\left(i,\sigma,i\omega_1;j,\sigma',i\omega_2|i,\sigma,i\omega_1-i\nu;j,\sigma'\right) - \beta\delta_{\nu,0}\langle\hat{\rho}_i\rangle\langle\hat{\rho}_j\rangle \\
=& \frac{4}{\beta^2}\sum_{i\omega_1,i\omega_2} \mathcal{G}_d^{(2)}\left(i,i\omega_1;j,i\omega_2|i,i\omega_1-i\nu;j\right) - \beta\delta_{\nu,0}\langle\hat{\rho}_i\rangle\langle\hat{\rho}_j\rangle \\
=& \frac{4}{\beta^2}\sum_{i\omega_1,i\omega_2} \mathcal{G}_d^{c,(2)}\left(i,i\omega_1;j,i\omega_2|i,i\omega_1-i\nu;j\right) - \frac{2}{\beta}\sum_{i\omega}\mathcal{G}\left(i\omega,i,j\right)\mathcal{G}\left(i\omega-i\nu,j,i\right) \\
=& \chi_{ij}^{\text{charge},c}(i\nu) + \chi_{ij}^{\text{charge},dc}(i\nu)
\end{aligned} \tag{A.3}$$

Here we used

$$\langle\hat{\rho}_i\rangle = \frac{2}{\beta}\sum_{i\omega}\mathrm{e}^{i\omega 0^+}\mathcal{G}\left(i\omega,i,i\right). \tag{A.4}$$

A.2 spin susceptibility

The dynamic spin-susceptibility follows from the spin-spin correlation function

$$\chi_{ij}^{\text{spin}}(i\nu) = \int_0^\beta \mathrm{d}\tau \mathrm{e}^{i\nu\tau} \left\langle T_\tau \hat{S}_i^+(\tau)\hat{S}_j^-(0)\right\rangle \tag{A.5}$$

with the spin operators

$$\hat{S}_i^+(\tau) = c_{i\uparrow}^\dagger(\tau)c_{i\downarrow}(\tau), \tag{A.6}$$

$$\hat{S}_i^-(\tau) = c_{i\downarrow}^\dagger(\tau)c_{i\uparrow}(\tau). \tag{A.7}$$

The expectation value is again given by a two-particle Green's function

$$\begin{aligned}
\chi_{ij}^{\text{spin}}(i\nu) =& -\int_0^\beta \mathrm{d}\tau \mathrm{e}^{i\nu\tau} \mathcal{G}^{(2)}\left(j,\uparrow,0^-;i,\downarrow,\tau|i,\uparrow,\tau;j,\downarrow\right) \\
=& -\frac{1}{\beta^2}\sum_{i\omega_1,i\omega_2} \mathcal{G}^{(2)}\left(j,\uparrow,i\omega_1;i,\downarrow,i\omega_2|i,\uparrow,i\omega_2-i\nu;j,\downarrow\right) \\
=& \frac{2}{\beta^2}\sum_{i\omega_1,i\omega_2} \mathcal{G}_m^{(2)}\left(i,i\omega_2;j,i\omega_1|i,i\omega_2-i\nu;j\right) \\
=& \frac{2}{\beta^2}\sum_{i\omega_1,i\omega_2} \mathcal{G}_m^{c,(2)}\left(i,i\omega_2;j,i\omega_1|i,i\omega_2-i\nu;j\right) \\
& -\frac{1}{\beta}\sum_{i\omega} \mathcal{G}\left(i\omega,i,j\right)\mathcal{G}\left(i\omega-i\nu,j,i\right) \\
=& \chi_{ij}^{\text{spin},c}(i\nu) + \chi_{ij}^{\text{spin},dc}(i\nu)
\end{aligned} \tag{A.8}$$

Appendix B

Exact diagonalization of the core-Hamiltonians

B.1 L=0-core

The Hamiltonian of the one-site Hubbard model (for $\epsilon_d = -U/2$, i.e. particle-hole symmetry) is given by

$$\hat{H} = -\frac{U}{2}\sum_{\sigma} n_\sigma + U n_\uparrow n_\downarrow. \tag{B.1}$$

There are four eigenstates given by

- the vacuum state $|0\rangle$ with energy $E_0 = 0$.
- $|N = 1, s_z = \sigma\rangle = d_\sigma^\dagger |0\rangle$ with energy $E_{N=1,s_z=\sigma} = -U/2$.
- $|N = 2, S = 0\rangle = d_\uparrow^\dagger d_\downarrow^\dagger |0\rangle$ with energy $E_{N=2,S=0} = 0$.

The one-particle Green's function can be calculated from the Lehmann representation (2.61).

$$\begin{aligned}\mathcal{G}(i\omega) =& \frac{i\omega}{(i\omega)^2 - \frac{U^2}{4}} \\ =& \frac{1}{i\omega + U/2 - \Sigma_{\text{dot}}(i\omega)}\end{aligned} \tag{B.2}$$

and the self-energy is obtained as

$$\Sigma_{\text{dot}}(i\omega) = \frac{U}{2} + \frac{U^2}{4i\omega}. \tag{B.3}$$

The two-particle 1PI vertex function follows from the Lehmann representation (2.62) and equations (2.27) and (2.37). It is given by [HJB+09]

$$\gamma^{(2)}\left(\uparrow, i\omega_1; \uparrow, i\omega_2 | \uparrow, i\omega_1'; \uparrow\right) = -\beta \frac{U^2}{4} \frac{\delta_{\omega_1,\omega_1'} - \delta_{\omega_2,\omega_1'}}{(i\omega_1)^2 (i\omega_2)^2} \left[(i\omega_1)^2 - \frac{U^2}{4}\right] \left[(i\omega_2)^2 - \frac{U^2}{4}\right] \tag{B.4}$$

$$\begin{aligned}
\gamma^{(2)}\left(\uparrow, i\omega_1; \downarrow, i\omega_2 | \uparrow, i\omega_1'; \downarrow\right) =& U + \left(\frac{U}{2}\right)^3 \frac{\sum_{i=1,2,1',2'} (i\omega_i)^2}{\prod_{i=1,2,1',2'} (i\omega_i)} - 6\left(\frac{U}{2}\right)^5 \prod_{i=1,2,1',2'} \frac{1}{(i\omega_i)} \\
&- \beta\delta_{\omega_1,-\omega_2} \frac{U^2}{2} n_F\left(\frac{U}{2}\right) \frac{\left[(i\omega_1)^2 - \frac{U^2}{4}\right]\left[(i\omega_{1'})^2 - \frac{U^2}{4}\right]}{(i\omega_1)^2 (i\omega_{1'})^2} \\
&+ \beta\delta_{\omega_2,\omega_1'} \frac{U^2}{2} n_F\left(-\frac{U}{2}\right) \frac{\left[(i\omega_1)^2 - \frac{U^2}{4}\right]\left[(i\omega_{1'})^2 - \frac{U^2}{4}\right]}{(i\omega_1)^2 (i\omega_{1'})^2} \\
&- \beta\delta_{\omega_1,\omega_1'} \frac{U^2}{4} \left[n_F\left(\frac{U}{2}\right) - n_F\left(-\frac{U}{2}\right)\right] \frac{\left[(i\omega_1)^2 - \frac{U^2}{4}\right]\left[(i\omega_2)^2 - \frac{U^2}{4}\right]}{(i\omega_1)^2 (i\omega_2)^2}
\end{aligned} \tag{B.5}$$

with $\omega_2' = \omega_1 + \omega_2 - \omega_1'$ and the Fermi function

$$n_F(x) = \frac{1}{1 + \exp(\beta x)} \tag{B.6}$$

The density- and magnetic part of γ follow with Eqs. (2.55) and (2.56) as

$$\begin{aligned}
\gamma_d\left(i\omega_1, i\omega_2 | i\omega_{1'}\right) =& \frac{1}{2}\left[\gamma\left(\uparrow, i\omega_1; \uparrow, i\omega_2 | \uparrow, i\omega_1'; \uparrow\right) + \gamma\left(\uparrow, i\omega_1; \downarrow, i\omega_2 | \uparrow, i\omega_1'; \downarrow\right)\right] \\
=& \frac{U}{2} + \frac{1}{2}\left(\frac{U}{2}\right)^3 \frac{\sum_{i=1,2,1',2'} (i\omega_i)^2}{\prod_{i=1,2,1',2'} (i\omega_i)} - 3\left(\frac{U}{2}\right)^5 \prod_{i=1,2,1',2'} \frac{1}{(i\omega_i)} \\
&- \beta\delta_{\omega_1,-\omega_2} \frac{U^2}{4} n_F\left(\frac{U}{2}\right) \frac{\left[(i\omega_1)^2 - \frac{U^2}{4}\right]\left[(i\omega_{1'})^2 - \frac{U^2}{4}\right]}{(i\omega_1)^2 (i\omega_{1'})^2} \\
&+ \beta\delta_{\omega_2,\omega_{1'}} \frac{U^2}{4} \left[\frac{1}{2} + n_F\left(-\frac{U}{2}\right)\right] \frac{\left[(i\omega_1)^2 - \frac{U^2}{4}\right]\left[(i\omega_2)^2 - \frac{U^2}{4}\right]}{(i\omega_1)^2 (i\omega_2)^2} \\
&- \beta\delta_{\omega_1,\omega_{1'}} \frac{U^2}{4} n_F\left(\frac{U}{2}\right) \frac{\left[(i\omega_1)^2 - \frac{U^2}{4}\right]\left[(i\omega_2)^2 - \frac{U^2}{4}\right]}{(i\omega_1)^2 (i\omega_2)^2}
\end{aligned} \tag{B.7}$$

$$\begin{aligned}\gamma_m\left(i\omega_1, i\omega_2|i\omega_{1'}\right) =& \frac{1}{2}\left[\gamma\left(\uparrow, i\omega_1;\uparrow, i\omega_2|\uparrow, i\omega_1';\uparrow\right) - \gamma\left(\uparrow, i\omega_1;\downarrow, i\omega_2|\uparrow, i\omega_1';\downarrow\right)\right] \\ =& -\frac{U}{2} - \frac{1}{2}\left(\frac{U}{2}\right)^3 \frac{\sum_{i=1,2,1',2'}(i\omega_i)^2}{\prod_{i=1,2,1',2'}(i\omega_i)} + 3\left(\frac{U}{2}\right)^5 \prod_{i=1,2,1',2'}\frac{1}{(i\omega_i)} \\ &+ \beta\delta_{\omega_1,-\omega_2}\frac{U^2}{4}n_F\left(\frac{U}{2}\right)\frac{\left[(i\omega_1)^2 - \frac{U^2}{4}\right]\left[(i\omega_{1'})^2 - \frac{U^2}{4}\right]}{(i\omega_1)^2(i\omega_{1'})^2} \\ &+ \beta\delta_{\omega_2,\omega_{1'}}\frac{U^2}{4}\left[\frac{1}{2} - n_F\left(-\frac{U}{2}\right)\right]\frac{\left[(i\omega_1)^2 - \frac{U^2}{4}\right]\left[(i\omega_2)^2 - \frac{U^2}{4}\right]}{(i\omega_1)^2(i\omega_2)^2} \\ &- \beta\delta_{\omega_1,\omega_{1'}}\frac{U^2}{4}n_F\left(-\frac{U}{2}\right)\frac{\left[(i\omega_1)^2 - \frac{U^2}{4}\right]\left[(i\omega_2)^2 - \frac{U^2}{4}\right]}{(i\omega_1)^2(i\omega_2)^2} \end{aligned} \tag{B.8}$$

with $\omega_2' = \omega_1 + \omega_2 - \omega_1'$.
With Eq. (A.3) one gets the dynamic charge-susceptibility

$$\chi^{\text{charge},c}\left(i\nu\right) = -U\frac{n_F\left(\frac{U}{2}\right) - n_F\left(-\frac{U}{2}\right)}{(i\nu)^2 - U^2} + \beta\delta_{\nu,0}n_F\left(\frac{U}{2}\right)^2, \tag{B.9}$$

$$\chi^{\text{charge},dc}\left(i\nu\right) = U\frac{n_F\left(\frac{U}{2}\right) - n_F\left(-\frac{U}{2}\right)}{(i\nu)^2 - U^2} + \beta\delta_{\nu,0}n_F\left(\frac{U}{2}\right)n_F\left(-\frac{U}{2}\right), \tag{B.10}$$

$$\chi^{\text{charge}}\left(i\nu\right) = \beta\delta_{\nu,0}n_F\left(\frac{U}{2}\right). \tag{B.11}$$

With Eq. (A.8) one gets the dynamic spin-susceptibility

$$\chi^{\text{spin},c}\left(i\nu\right) = -\frac{U}{2}\frac{n_F\left(\frac{U}{2}\right) - n_F\left(-\frac{U}{2}\right)}{(i\nu)^2 - U^2} + \beta\delta_{\nu,0}\frac{1}{2}n_F\left(-\frac{U}{2}\right)^2, \tag{B.12}$$

$$\chi^{\text{spin},dc}\left(i\nu\right) = \frac{U}{2}\frac{n_F\left(\frac{U}{2}\right) - n_F\left(-\frac{U}{2}\right)}{(i\nu)^2 - U^2} + \beta\delta_{\nu,0}\frac{1}{2}n_F\left(\frac{U}{2}\right)n_F\left(-\frac{U}{2}\right), \tag{B.13}$$

$$\chi^{\text{spin}}\left(i\nu\right) = \beta\delta_{\nu,0}\frac{1}{2}n_F\left(-\frac{U}{2}\right). \tag{B.14}$$

B.2 L=1-core

The $L = 1$-core consists of an interacting dot site connected to a noninteracting bath site. It is described by the Hamiltonian

$$\hat{H} = \epsilon_d\sum_\sigma \hat{n}_{d,\sigma} + U\hat{n}_{d,\uparrow}\hat{n}_{d,\downarrow} - v\sum_\sigma\left(d_\sigma^\dagger b_\sigma + b_\sigma^\dagger d_\sigma\right) \tag{B.15}$$

Written as a matrix in Fock space it can be diagonalized analytically and in the following we list the eigenstates and corresponding energies. Denoting the Vacuum-state by $|0\rangle$, the one-particle states are given by (unnormalized)

- $|N=1;s_z=\sigma;1\rangle = \left[\left(\epsilon_d - \sqrt{4v^2+\epsilon_d^2}\right) d_\sigma^\dagger - 2v b_\sigma^\dagger\right]|0\rangle$
  with energy $E_{N=1;1} = \frac{1}{2}\left(\epsilon_d - \sqrt{4v^2+\epsilon_d^2}\right)$.
- $|N=1;s_z=\sigma;2\rangle = \left[\left(\epsilon_d + \sqrt{4v^2+\epsilon_d^2}\right) d_\sigma^\dagger - 2v b_\sigma^\dagger\right]|0\rangle$
  with energy $E_{N=1;2} = \frac{1}{2}\left(\epsilon_d + \sqrt{4v^2+\epsilon_d^2}\right)$.

The two-particle states can be classified by their total spin. There are three triplet-states given by

- $|N=2;S=1;S_z=+1\rangle = d_\uparrow^\dagger b_\uparrow^\dagger|0\rangle$
- $|N=2;S=1;S_z=0\rangle = \frac{1}{\sqrt{2}}\left[d_\uparrow^\dagger b_\downarrow^\dagger + d_\downarrow^\dagger b_\uparrow^\dagger\right]|0\rangle$
- $|N=2;S=1;S_z=-1\rangle = d_\downarrow^\dagger b_\downarrow^\dagger|0\rangle$

The energy of the triplet-states is $E_{N=2;S=1} = \epsilon_d$.
To construct the remaining singlet-states we use the base $\{d_\uparrow^\dagger d_\downarrow^\dagger|0\rangle, \frac{1}{\sqrt{2}}\left(d_\uparrow^\dagger b_\downarrow^\dagger - d_\downarrow^\dagger b_\uparrow^\dagger\right)|0\rangle, b_\uparrow^\dagger b_\downarrow^\dagger|0\rangle\}$.
In this base the Hamiltonian (B.15) is given by

$$\begin{bmatrix} U+2\epsilon_d & -\sqrt{2}v & 0 \\ -\sqrt{2}v & \epsilon_d & -\sqrt{2}v \\ 0 & -\sqrt{2}v & 0 \end{bmatrix} \tag{B.16}$$

The eigenvalues of this matrix have a complicated form and are not shown here. We concentrate on the particle-hole symmetric point, where $\epsilon_d = -U/2$. In this case the three singlet-states are given by (unnormalized)

- $|N=2;S=0;1\rangle = \left[8v\left(d_\uparrow^\dagger d_\downarrow^\dagger + b_\uparrow^\dagger b_\downarrow^\dagger\right) + \left(U+\sqrt{U^2+64v^2}\right)\left(d_\uparrow^\dagger b_\downarrow^\dagger - d_\downarrow^\dagger b_\uparrow^\dagger\right)\right]|0\rangle$
  with energy $E_{N=2;S=0;1} = \frac{1}{4}\left(-U-\sqrt{U^2+64v^2}\right)$
- $|N=2;S=0;2\rangle = \frac{1}{\sqrt{2}}\left[d_\uparrow^\dagger d_\downarrow^\dagger - b_\uparrow^\dagger b_\downarrow^\dagger\right]|0\rangle$ with energy $E_{N=2;S=0;2} = 0$.
- $|N=2;S=0;3\rangle = \left[8v\left(d_\uparrow^\dagger d_\downarrow^\dagger + b_\uparrow^\dagger b_\downarrow^\dagger\right) + \left(U-\sqrt{U^2+64v^2}\right)\left(d_\uparrow^\dagger b_\downarrow^\dagger - d_\downarrow^\dagger b_\uparrow^\dagger\right)\right]|0\rangle$
  with energy $E_{N=2;S=0;3} = \frac{1}{4}\left(-U+\sqrt{U^2+64v^2}\right)$

The three-particle states are given by (unnormalized)

- $|N=3;S=1/2;S_z=\sigma;1\rangle = \left[\left(U+\epsilon_d - \sqrt{4v^2+(U+\epsilon_d)^2}\right) d_\sigma^\dagger b_\uparrow^\dagger b_\downarrow^\dagger + 2v d_\uparrow^\dagger d_\downarrow^\dagger b_\sigma^\dagger\right]|0\rangle$
  with energy $E_{N=3;S=1/2;1} = \frac{1}{2}\left(U+3\epsilon_d - \sqrt{4v^2+(U+\epsilon_d)^2}\right)$.
- $|N=3;S=1/2;S_z=\sigma;2\rangle = \left[\left(U+\epsilon_d + \sqrt{4v^2+(U+\epsilon_d)^2}\right) d_\sigma^\dagger b_\uparrow^\dagger b_\downarrow^\dagger + 2v d_\uparrow^\dagger d_\downarrow^\dagger b_\sigma^\dagger\right]|0\rangle$
  with energy $E_{N=3;S=1/2;2} = \frac{1}{2}\left(U+3\epsilon_d + \sqrt{4v^2+(U+\epsilon_d)^2}\right)$.

Finally, the four-particle state is given by $|N=4,S=0\rangle = d^\dagger_\uparrow d^\dagger_\downarrow b^\dagger_\uparrow b^\dagger_\downarrow |0\rangle$ with energy $E_{N=4,S=0} = U + 2\epsilon_d$.
The one-partice Green's function on the dot site is given by [Lan98]

$$\mathcal{G}(i\omega) = \sum_{m=1}^{2} \left(\frac{a_m}{i\omega - \epsilon_m} + \frac{a_m}{i\omega + \epsilon_m} \right), \tag{B.17}$$

$$\epsilon_1 = \frac{1}{4}\left(\sqrt{U^2 + 64v^2} - \sqrt{U^2 + 16v^2} \right), \tag{B.18}$$

$$\epsilon_2 = \frac{1}{4}\left(\sqrt{U^2 + 64v^2} + \sqrt{U^2 + 16v^2} \right), \tag{B.19}$$

$$a_1 = \frac{1}{4}\left(1 - \frac{U^2 - 32v^2}{\sqrt{(U^2 + 64v^2)(U^2 + 16v^2)}} \right), \tag{B.20}$$

$$a_2 = \frac{1}{2} - a_1 \tag{B.21}$$

In the spectral density $A(\omega) = -\frac{1}{\pi}\mathrm{Im}\ \mathcal{G}(i\omega \to \omega + i0^+)$ one finds four delta-peaks

$$A(\omega) = \sum_{m=1}^{2} a_m \left[\delta(\omega + \epsilon_m) + \delta(\omega - \epsilon_m) \right] \tag{B.22}$$

From the noninteracting Green's function

$$\mathcal{G}_0(i\omega) = \frac{1}{2}\left(\frac{1}{i\omega - v} + \frac{1}{i\omega + v} \right) \tag{B.23}$$

follows the self-energy by the Dyson equation $\Sigma_{\mathrm{dot}}(i\omega) = \mathcal{G}_0^{-1}(i\omega) - \mathcal{G}^{-1}(i\omega)$

$$\Sigma_{\mathrm{dot}}(i\omega) = \frac{U^2}{8}\left(\frac{1}{i\omega - 3v} + \frac{1}{i\omega + 3v} \right) \tag{B.24}$$

B.3 Two-site Hubbard model

The two-site Hubbard model is described by the Hamiltonian

$$\hat{H} = \epsilon_d \sum_\sigma \sum_{i=1}^{2} \hat{n}_{i,\sigma} + U \sum_{i=1}^{2} \hat{n}_{i,\uparrow}\hat{n}_{i,\downarrow} - t \sum_\sigma \left(d^\dagger_{1,\sigma} d_{2,\sigma} + d^\dagger_{2,\sigma} d_{1,\sigma} \right) \tag{B.25}$$

Denoting the Vacuum-state by $|0\rangle$, the one-particle states are given by

- $|N=1; s_z=\sigma; 1\rangle = \frac{1}{\sqrt{2}}\left[d^\dagger_{1,\sigma} + d^\dagger_{2,\sigma} \right]|0\rangle$ with energy $E_{N=1;s_z=\sigma;1} = \epsilon_d - t$.
- $|N=1; s_z=\sigma; 2\rangle = \frac{1}{\sqrt{2}}\left[d^\dagger_{1,\sigma} - d^\dagger_{2,\sigma} \right]|0\rangle$ with energy $E_{N=1;s_z=\sigma;2} = \epsilon_d + t$.

The two-particle states can be classified by their total spin. There are three triplet-states given by

- $|N=2;S=1;S_z=+1\rangle = d^\dagger_{1,\uparrow}d^\dagger_{2,\uparrow}|0\rangle$
- $|N=2;S=1;S_z=0\rangle = \frac{1}{\sqrt{2}}\left[d^\dagger_{1,\uparrow}d^\dagger_{2,\downarrow}+d^\dagger_{1,\downarrow}d^\dagger_{2,\uparrow}\right]|0\rangle$
- $|N=2;S=1;S_z=-1\rangle = d^\dagger_{1,\downarrow}d^\dagger_{2,\downarrow}|0\rangle$

The energy of the triplet-states is $E_{N=2;S=1}=2\epsilon_d$.
To construct the remaining singlet-states we use the base
$\{\frac{1}{\sqrt{2}}\left(d^\dagger_{1,\uparrow}d^\dagger_{1,\downarrow}+d^\dagger_{2,\uparrow}d^\dagger_{2,\downarrow}\right)|0\rangle, \frac{1}{\sqrt{2}}\left(d^\dagger_{1,\uparrow}d^\dagger_{2,\downarrow}-d^\dagger_{1,\downarrow}d^\dagger_{2,\uparrow}\right)|0\rangle, \frac{1}{\sqrt{2}}\left(d^\dagger_{1,\uparrow}d^\dagger_{1,\downarrow}-d^\dagger_{2,\uparrow}d^\dagger_{2,\downarrow}\right)|0\rangle\}$.
In this base the Hamiltonian (B.25) is given by

$$\begin{bmatrix} 2\epsilon_d+U & -2t & 0 \\ -2t & 2\epsilon_d & 0 \\ 0 & 0 & 2\epsilon_d+U \end{bmatrix} \tag{B.26}$$

The three singlet-states are given by ($\gamma=\frac{\sqrt{U^2+16t^2}}{U}$)

- $|N=2;S=0;1\rangle =$
  $\frac{1}{\sqrt{16t^2+U^2(1+\gamma)^2}}\left[2\sqrt{2}t\left(d^\dagger_{1,\uparrow}d^\dagger_{2,\downarrow}-d^\dagger_{1,\downarrow}d^\dagger_{2,\uparrow}\right)-\frac{U}{\sqrt{2}}(1-\gamma)\left(d^\dagger_{1,\uparrow}d^\dagger_{1,\downarrow}+d^\dagger_{2,\uparrow}d^\dagger_{2,\downarrow}\right)\right]|0\rangle$
  with energy $E_{N=2;S=0;1}=2\epsilon_d+\frac{U}{2}(1-\gamma)$.
- $|N=2;S=0;2\rangle =$
  $\frac{1}{\sqrt{16t^2+U^2(1+\gamma)^2}}\left[2\sqrt{2}t\left(d^\dagger_{1,\uparrow}d^\dagger_{2,\downarrow}-d^\dagger_{1,\downarrow}d^\dagger_{2,\uparrow}\right)-\frac{U}{\sqrt{2}}(1+\gamma)\left(d^\dagger_{1,\uparrow}d^\dagger_{1,\downarrow}+d^\dagger_{2,\uparrow}d^\dagger_{2,\downarrow}\right)\right]|0\rangle$
  with energy $E_{N=2;S=0;2}=2\epsilon_d+\frac{U}{2}(1+\gamma)$.
- $|N=2;S=0;3\rangle = \frac{1}{\sqrt{2}}\left(d^\dagger_{1,\uparrow}d^\dagger_{1,\downarrow}-d^\dagger_{2,\uparrow}d^\dagger_{2,\downarrow}\right)|0\rangle$ with energy $E_{N=2;S=0;3}=2\epsilon_d+U$

The three-particle states are given by

- $|N=3;S=1/2;S_z=\sigma,1\rangle = \frac{1}{\sqrt{2}}\left[d^\dagger_{1,\uparrow}d^\dagger_{1,\downarrow}d^\dagger_{2,\sigma}+d^\dagger_{1,\sigma}d^\dagger_{2,\uparrow}d^\dagger_{2,\downarrow}\right]|0\rangle$
  with energy $E_{N=3;S=1/2;S_z=\sigma,1}=3\epsilon_d+U+t$.
- $|N=3;S=1/2;S_z=\sigma,2\rangle = \frac{1}{\sqrt{2}}\left[d^\dagger_{1,\uparrow}d^\dagger_{1,\downarrow}d^\dagger_{2,\sigma}-d^\dagger_{1,\sigma}d^\dagger_{2,\uparrow}d^\dagger_{2,\downarrow}\right]|0\rangle$
  with energy $E_{N=3;S=1/2;S_z=\sigma,2}=3\epsilon_d+U-t$.

Finally, the four-particle state is given by $|N=4;S=0\rangle = d^\dagger_{1,\uparrow}d^\dagger_{1,\downarrow}d^\dagger_{2,\uparrow}d^\dagger_{2,\downarrow}|0\rangle$ with energy $E_{N=4;S=0}=4\epsilon_d+2U$.

Appendix C

Symmetries of the two-particle vertex

C.1 Single-site vertices

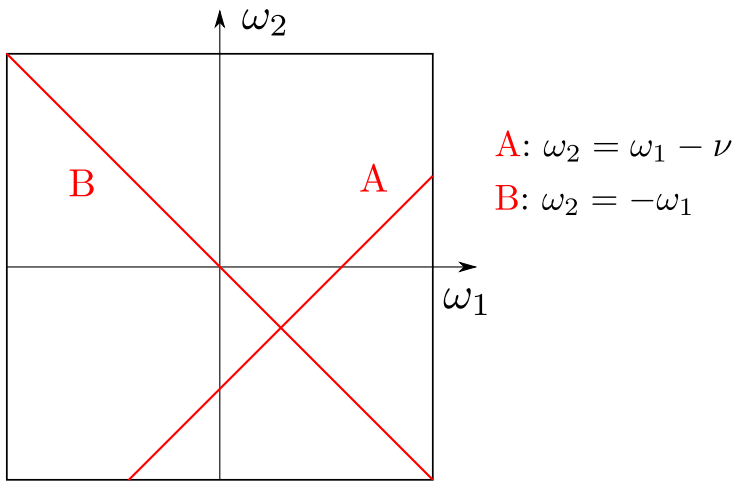

Figure C.1: Schematic plot of $\gamma_{d/m}\left(\alpha_1, i\omega_1; \alpha_2, i\omega_2 | \alpha_{1'}, i\omega_1 - i\nu; \alpha_{2'}, i\omega_2 + i\nu\right)$ with the symmetry axes A and B.

If we plot the local vertex $\gamma_{d/m}\left(i\omega_1; i\omega_2 | i\omega_1 - i\nu; i\omega_2 + i\nu\right)$ in the $\omega_1 - \omega_2$-plane, we have the symmetry axes $A:\ \omega_2 = \omega_1 - \nu$ and $B:\ \omega_2 = -\omega_1$ (cf. Fig. C.1). M_A and M_B are mirror operators at axis A and B respectively.

Mirror symmetry at axis A

By mirroring at axis A, the point (ω_1, ω_2) is mapped to the point $(\omega_2 + \nu, \omega_1 - \nu)$. For a time reversal invariant Hamiltonian the vertex $\gamma_{d/m}$ is symmetric with respect to this

transformation, which follows from

$$\begin{aligned}\gamma_{d/m}\left(i\omega_1; i\omega_2 | i\omega_1 - i\nu; i\omega_2 + i\nu\right) &\overset{M_A}{\rightarrow} \gamma_{d/m}\left(i\omega_2 + i\nu; i\omega_1 - i\nu | i\omega_2; i\omega_1\right) \\ &\overset{(2.45)}{=} \gamma_{d/m}\left(i\omega_2; i\omega_1 | i\omega_2 + i\nu; i\omega_1 - i\nu\right) \\ &= \gamma_{d/m}\left(i\omega_1; i\omega_2 | i\omega_1 - i\nu; i\omega_2 + i\nu\right). \end{aligned} \tag{C.1}$$

Mirror symmetry at axis B

Mirroring at axis B maps the point (ω_1, ω_2) to the point $(-\omega_2, -\omega_1)$. The transformation behaviour of $\gamma_{d/m}$ with respect to M_B is again related to time reversion symmetry.

$$\begin{aligned}\gamma_{d/m}\left(i\omega_1; i\omega_2 | i\omega_1 - i\nu; i\omega_2 + i\nu\right) &\overset{M_B}{\rightarrow} \gamma_{d/m}\left(-i\omega_2; -i\omega_1 | -i\omega_2 - i\nu; -i\omega_1 + i\nu\right) \\ &\overset{(2.44)}{=} \gamma_{d/m}\left(i\omega_2; i\omega_1 | i\omega_2 + i\nu; i\omega_1 - i\nu\right)^* \\ &= \gamma_{d/m}\left(i\omega_1; i\omega_2 | i\omega_1 - i\nu; i\omega_2 + i\nu\right)^*. \end{aligned} \tag{C.2}$$

In the particle-hole symmetric case one has additionally $\gamma_{d/m}\left(i\omega_1; i\omega_2 | i\omega_1 - i\nu; i\omega_2 + i\nu\right)^* = \gamma_{d/m}\left(i\omega_1; i\omega_2 | i\omega_1 - i\nu; i\omega_2 + i\nu\right)$ (cf. Eq. (2.59)) and the vertex is symmetric with respect to M_B.

C.2 Cluster vertices

For the cluster vertices the transformation behaviour is more complex. By the Fourier Transform $U_{\vec{K}_i, \vec{R}_j} = \frac{1}{\sqrt{2}} \exp\left[i\vec{K}_i\vec{R}_j\right]$ with $\vec{K}_1 = (0,0)$ and $\vec{K}_2 = (\pi, \pi)$ we transform the vertices to cluster-momentum space

$$\begin{aligned}&\gamma_{d/m}\left[\vec{Q}_1, i\omega_1; \vec{Q}_2, i\omega_2 | \vec{Q}_{1'}, i\omega_1 - i\nu; \vec{Q}_{2'}, i\omega_2 + i\nu\right] \\ =&\frac{1}{4} \sum_{\substack{\vec{R}_1, \vec{R}_2, \\ \vec{R}_{1'}, \vec{R}_{2'}}} \exp\left[i\vec{Q}_1\vec{R}_1 + i\vec{Q}_2\vec{R}_2 - i\vec{Q}_{1'}\vec{R}_{1'} - i\vec{Q}_{2'}\vec{R}_{2'}\right] \\ &\times \gamma_{d/m}\left[\vec{R}_1, i\omega_1; \vec{R}_2, i\omega_2 | \vec{R}_{1'}, i\omega_1 - i\nu; \vec{R}_{2'}, i\omega_2 + i\nu\right]. \end{aligned} \tag{C.3}$$

Here we have $\vec{Q}_{i^{(\prime)}} \in \{\vec{K}_1, \vec{K}_2\}$ and $\vec{R}_1$ and $\vec{R}_2$ are defined in Fig. 6.6.

If we assume time-reversion and particle-holy symmetry we have from Eq. (2.59)

$$\begin{aligned}
& \gamma_{d/m}\left[\vec{Q}_1, i\omega_1; \vec{Q}_2, i\omega_2 | \vec{Q}_{1'}, i\omega_1 - i\nu; \vec{Q}_{2'}, i\omega_2 + i\nu\right]^* \\
= \quad & \frac{1}{4} \sum_{\substack{\vec{R}_1, \vec{R}_2, \\ \vec{R}_{1'}, \vec{R}_{2'}}} \exp\left[-i\vec{Q}_1\vec{R}_1 - i\vec{Q}_2\vec{R}_2 + i\vec{Q}_{1'}\vec{R}_{1'} + i\vec{Q}_{2'}\vec{R}_{2'}\right] \\
& \times \gamma_{d/m}\left[\vec{R}_1, i\omega_1; \vec{R}_2, i\omega_2 | \vec{R}_{1'}, i\omega_1 - i\nu; \vec{R}_{2'}, i\omega_2 + i\nu\right]^* \\
\overset{(2.59)}{=} \quad & \frac{1}{4} \sum_{\substack{\vec{R}_1, \vec{R}_2, \\ \vec{R}_{1'}, \vec{R}_{2'}}} \exp\left[-i\vec{Q}_1\vec{R}_1 - i\vec{Q}_2\vec{R}_2 + i\vec{Q}_{1'}\vec{R}_{1'} + i\vec{Q}_{2'}\vec{R}_{2'}\right] \\
& \times \varsigma_{\vec{R}_1\vec{R}_2\vec{R}_{1'}\vec{R}_{2'}} \gamma_{d/m}\left[\vec{R}_1, i\omega_1; \vec{R}_2, i\omega_2 | \vec{R}_{1'}, i\omega_1 - i\nu; \vec{R}_{2'}, i\omega_2 + i\nu\right] \\
= \quad & \frac{1}{4} \sum_{\substack{\vec{R}_1, \vec{R}_2, \\ \vec{R}_{1'}, \vec{R}_{2'}}} \exp\left[-i\vec{\bar{Q}}_1\vec{R}_1 - i\vec{\bar{Q}}_2\vec{R}_2 + i\vec{\bar{Q}}_{1'}\vec{R}_{1'} + i\vec{\bar{Q}}_{2'}\vec{R}_{2'}\right] \\
& \times \gamma_{d/m}\left[\vec{R}_1, i\omega_1; \vec{R}_2, i\omega_2 | \vec{R}_{1'}, i\omega_1 - i\nu; \vec{R}_{2'}, i\omega_2 + i\nu\right] \\
= \quad & \gamma_{d/m}\left[\vec{\bar{Q}}_1, i\omega_1; \vec{\bar{Q}}_2, i\omega_2 | \vec{\bar{Q}}_{1'}, i\omega_1 - i\nu; \vec{\bar{Q}}_{2'}, i\omega_2 + i\nu\right]
\end{aligned} \tag{C.4}$$

with $\vec{\bar{K}}_1 = \vec{K}_2$ and $\vec{\bar{K}}_2 = \vec{K}_1$.

As already pointed out in chapter 6.3.2 the only nonnegative contributions are given by

$$\begin{aligned}
\gamma_{d/m}(\vec{K}_1, i\omega_1; \vec{K}_1, i\omega_2 | \vec{K}_1, i\omega_{1'}; \vec{K}_1, i\omega_{2'}) &\equiv \gamma^{1111}_{d/m}(i\omega_1; i\omega_2 | i\omega_{1'}; i\omega_{2'}), \\
\gamma_{d/m}(\vec{K}_1, i\omega_1; \vec{K}_2, i\omega_2 | \vec{K}_1, i\omega_{1'}; \vec{K}_2, i\omega_{2'}) &\equiv \gamma^{1212}_{d/m}(i\omega_1; i\omega_2 | i\omega_{1'}; i\omega_{2'}), \\
\gamma_{d/m}(\vec{K}_1, i\omega_1; \vec{K}_2, i\omega_2 | \vec{K}_2, i\omega_{1'}; \vec{K}_1, i\omega_{2'}) &\equiv \gamma^{1221}_{d/m}(i\omega_1; i\omega_2 | i\omega_{1'}; i\omega_{2'}), \\
\gamma_{d/m}(\vec{K}_1, i\omega_1; \vec{K}_1, i\omega_2 | \vec{K}_2, i\omega_{1'}; \vec{K}_2, i\omega_{2'}) &\equiv \gamma^{1122}_{d/m}(i\omega_1; i\omega_2 | i\omega_{1'}; i\omega_{2'})
\end{aligned}$$

and the same quantities with $\vec{K}_1 \leftrightarrow \vec{K}_2$ respectively. Due to Eq. (C.4) we can restrict the discussion to the former vertices. The transformation behaviour under M_A and M_B follows as:

Mirror symmetry at axis A

$$\begin{aligned}
\gamma^{1111}_{d/m}\left[i\omega_1; i\omega_2 | i\omega_1 - i\nu; i\omega_2 + i\nu\right] &\overset{M_A}{\to} \gamma^{1111}_{d/m}\left[i\omega_2 + i\nu; i\omega_1 - i\nu | i\omega_2; i\omega_1\right] \\
&\overset{(2.45)}{=} \gamma^{1111}_{d/m}\left[i\omega_2; i\omega_1 | i\omega_2 + i\nu; i\omega_1 - i\nu\right] \\
&= \gamma^{1111}_{d/m}\left[i\omega_1; i\omega_2 | i\omega_1 - i\nu; i\omega_2 + i\nu\right]
\end{aligned} \tag{C.5}$$

$$\begin{aligned}
\gamma^{1212}_{d/m}\left[i\omega_1; i\omega_2 | i\omega_1 - i\nu; i\omega_2 + i\nu\right] &\overset{M_A}{\to} \gamma^{1212}_{d/m}\left[i\omega_2 + i\nu; i\omega_1 - i\nu | i\omega_2; i\omega_1\right] \\
&\overset{(2.45)}{=} \gamma^{1212}_{d/m}\left[i\omega_2; i\omega_1 | i\omega_2 + i\nu; i\omega_1 - i\nu\right] \\
&= \gamma^{2121}_{d/m}\left[i\omega_1; i\omega_2 | i\omega_1 - i\nu; i\omega_2 + i\nu\right] \\
&\overset{(C.4)}{=} \gamma^{1212}_{d/m}\left[i\omega_1; i\omega_2 | i\omega_1 - i\nu; i\omega_2 + i\nu\right]^* \qquad \text{(C.6)} \\
\gamma^{1221}_{d/m}\left[i\omega_1; i\omega_2 | i\omega_1 - i\nu; i\omega_2 + i\nu\right] &\overset{M_A}{\to} \gamma^{1221}_{d/m}\left[i\omega_2 + i\nu; i\omega_1 - i\nu | i\omega_2; i\omega_1\right] \\
&\overset{(2.45)}{=} \gamma^{2112}_{d/m}\left[i\omega_2; i\omega_1 | i\omega_2 + i\nu; i\omega_1 - i\nu\right] \\
&= \gamma^{1221}_{d/m}\left[i\omega_1; i\omega_2 | i\omega_1 - i\nu; i\omega_2 + i\nu\right] \qquad \text{(C.7)} \\
\gamma^{1122}_{d/m}\left[i\omega_1; i\omega_2 | i\omega_1 - i\nu; i\omega_2 + i\nu\right] &\overset{M_A}{\to} \gamma^{1122}_{d/m}\left[i\omega_2 + i\nu; i\omega_1 - i\nu | i\omega_2; i\omega_1\right] \\
&\overset{(2.45)}{=} \gamma^{2211}_{d/m}\left[i\omega_2; i\omega_1 | i\omega_2 + i\nu; i\omega_1 - i\nu\right] \\
&= \gamma^{2211}_{d/m}\left[i\omega_1; i\omega_2 | i\omega_1 - i\nu; i\omega_2 + i\nu\right] \\
&\overset{(C.4)}{=} \gamma^{1122}_{d/m}\left[i\omega_1; i\omega_2 | i\omega_1 - i\nu; i\omega_2 + i\nu\right]^* \qquad \text{(C.8)}
\end{aligned}$$

Mirror symmetry at axis B

$$\begin{aligned}
\gamma^{1111}_{d/m}\left[i\omega_1; i\omega_2 | i\omega_1 - i\nu; i\omega_2 + i\nu\right] &\overset{M_B}{\to} \gamma^{1111}_{d/m}\left[-i\omega_2; -i\omega_1 | -i\omega_2 - i\nu; -i\omega_1 + i\nu\right] \\
&\overset{(2.44)}{=} \gamma^{1111}_{d/m}\left[i\omega_2; i\omega_1 | i\omega_2 + i\nu; i\omega_1 - i\nu\right]^* \\
&= \gamma^{1111}_{d/m}\left[i\omega_1; i\omega_2 | i\omega_1 - i\nu; i\omega_2 + i\nu\right]^* \qquad \text{(C.9)} \\
\gamma^{1212}_{d/m}\left[i\omega_1; i\omega_2 | i\omega_1 - i\nu; i\omega_2 + i\nu\right] &\overset{M_B}{\to} \gamma^{1212}_{d/m}\left[-i\omega_2; -i\omega_1 | -i\omega_2 - i\nu; -i\omega_1 + i\nu\right] \\
&\overset{(2.44)}{=} \gamma^{1212}_{d/m}\left[i\omega_2; i\omega_1 | i\omega_2 + i\nu; i\omega_1 - i\nu\right]^* \\
&= \gamma^{2121}_{d/m}\left[i\omega_1; i\omega_2 | i\omega_1 - i\nu; i\omega_2 + i\nu\right]^* \\
&\overset{(C.4)}{=} \gamma^{1212}_{d/m}\left[i\omega_1; i\omega_2 | i\omega_1 - i\nu; i\omega_2 + i\nu\right] \qquad \text{(C.10)} \\
\gamma^{1221}_{d/m}\left[i\omega_1; i\omega_2 | i\omega_1 - i\nu; i\omega_2 + i\nu\right] &\overset{M_B}{\to} \gamma^{1221}_{d/m}\left[-i\omega_2; -i\omega_1 | -i\omega_2 - i\nu; -i\omega_1 + i\nu\right] \\
&\overset{(2.44)}{=} \gamma^{1221}_{d/m}\left[i\omega_2; i\omega_1 | i\omega_2 + i\nu; i\omega_1 - i\nu\right]^* \\
&= \gamma^{2112}_{d/m}\left[i\omega_1; i\omega_2 | i\omega_1 - i\nu; i\omega_2 + i\nu\right]^* \\
&\overset{(C.4)}{=} \gamma^{1221}_{d/m}\left[i\omega_1; i\omega_2 | i\omega_1 - i\nu; i\omega_2 + i\nu\right] \qquad \text{(C.11)} \\
\gamma^{1122}_{d/m}\left[i\omega_1; i\omega_2 | i\omega_1 - i\nu; i\omega_2 + i\nu\right] &\overset{M_B}{\to} \gamma^{1122}_{d/m}\left[-i\omega_2; -i\omega_1 | -i\omega_2 - i\nu; -i\omega_1 + i\nu\right] \\
&\overset{(2.44)}{=} \gamma^{1122}_{d/m}\left[i\omega_2; i\omega_1 | i\omega_2 + i\nu; i\omega_1 - i\nu\right]^* \\
&= \gamma^{1122}_{d/m}\left[i\omega_1; i\omega_2 | i\omega_1 - i\nu; i\omega_2 + i\nu\right]^* \qquad \text{(C.12)}
\end{aligned}$$

For $\nu = 0$ the vertices $\gamma^{1221}_{d/m}\left[i\omega_1; i\omega_2 | i\omega_1; i\omega_2\right]$ and $\gamma^{1122}_{d/m}\left[i\omega_1; i\omega_2 | i\omega_1; i\omega_2\right]$ are purely real,

due to

$$\begin{aligned}
\gamma^{1221}_{d/m}\left[i\omega_1; i\omega_2 | i\omega_1; i\omega_2\right] &\overset{(2.45)}{=} \gamma^{2112}_{d/m}\left[i\omega_1; i\omega_2 | i\omega_1; i\omega_2\right] \\
&\overset{(C.4)}{=} \gamma^{1221}_{d/m}\left[i\omega_1; i\omega_2 | i\omega_1; i\omega_2\right]^* , \qquad \text{(C.13)} \\
\gamma^{1122}_{d/m}\left[i\omega_1; i\omega_2 | i\omega_1; i\omega_2\right] &\overset{(2.45)}{=} \gamma^{2211}_{d/m}\left[i\omega_1; i\omega_2 | i\omega_1; i\omega_2\right] \\
&\overset{(C.4)}{=} \gamma^{1122}_{d/m}\left[i\omega_1; i\omega_2 | i\omega_1; i\omega_2\right]^* . \qquad \text{(C.14)}
\end{aligned}$$

Appendix D

Hybridization flow for N-chain ladders

In the following we show that the hybridization flow formalism can be generalized to multi-impurity problems in the form of a semi-infinite N-chain ladder as shown in Fig. D.1 for the case $N = 2$. The derivation is completely analogue to the single impurity, presented in chapter 4, and we just present the important steps
The Hamiltonian of a N-chain ladder with a local interaction on the first rung is given by

$$\begin{aligned}\hat{H}_{\text{N-site-And}} =& U\sum_{\sigma}\sum_{j=1}^{N}\hat{n}_{d,j,\uparrow}\hat{n}_{d,j,\downarrow} - t_0^{\perp}\sum_{j=1}^{N-1}\sum_{\sigma}\left(d_{j,\sigma}^{\dagger}d_{j+1,\sigma} + H.c.\right) - t_0\sum_{\sigma}\sum_{j=1}^{N}\left(d_{j,\sigma}^{\dagger}b_{1,j,\sigma} + H.c.\right)\\ &-\sum_{i=1}^{\infty}\sum_{j=1}^{N}\sum_{\sigma}t_i\left(b_{i,j,\sigma}^{\dagger}b_{i+1,j,\sigma} + H.c.\right) - \sum_{i=1}^{\infty}\sum_{j=1}^{N-1}\sum_{\sigma}t_i^{\perp}\left(b_{i,j,\sigma}^{\dagger}b_{i,j+1,\sigma} + H.c.\right).\end{aligned} \tag{D.1}$$

As shown in Fig. D.1 the system is again divided into two parts: The "core" consists of the correlated rung and the first L bath rungs and the "bath" includes the remaining bath rungs with index $i > L$. We mulitiply the hopping between the core and bath by a factor Λ, i.e. $t_L \to \Lambda t_L$.
The fRG flow is implemented in an effective theory on the bath rung b_{L+1} which follows from the original theory (D.1) by integrating out the core and all bath rungs with index $i > 1$ in a functional integral representation. Up to the fourth order in the fields, the effective action is given by

$$\begin{aligned}S^{\text{eff}}\left[\bar{b}_{L+1}, b_{L+1}\right] =& -\frac{1}{\beta}\sum_{i\omega}\sum_{\sigma}\bar{b}_{L+1,\sigma}(i\omega)\hat{Q}_{\sigma}^{\text{eff},\Lambda}(i\omega)b_{L+1,\sigma}(i\omega)\\ &-\frac{(\Lambda t_L)^4}{4\beta^3}\sum_{\substack{i\omega_1,i\omega_2,\\ i\omega_{1'},i\omega_{2'}}}\sum_{\substack{i_1,i_2,\\ i_{1'},i_{2'}}}\sum_{\substack{\sigma_1,\sigma_2,\\ \sigma_{1'},\sigma_{2'}}}\bar{b}_{L+1,i_1,\sigma_1}(i\omega_1)\bar{b}_{L+1,i_2,\sigma_2}(i\omega_2)\\ &\times\mathcal{G}_{core}^{c,(2)}\left(i\omega_1, b_L, i_1, \sigma_1; i\omega_2, b_L, i_2, \sigma_2 | i\omega_{1'}, b_L, i_{1'}, \sigma_{1'}; i\omega_{2'}, b_L, i_{2'}, \sigma_{2'}\right)\\ &\times b_{L+1,i_{1'},\sigma_{1'}}(i\omega_{1'})b_{L+1,i_{2'},\sigma_{2'}}(i\omega_{2'})\delta_{\omega_1+\omega_2,\omega_{1'}+\omega_{2'}}\delta_{\sigma_1+\sigma_2,\sigma_{1'}+\sigma_{2'}}\end{aligned} \tag{D.2}$$

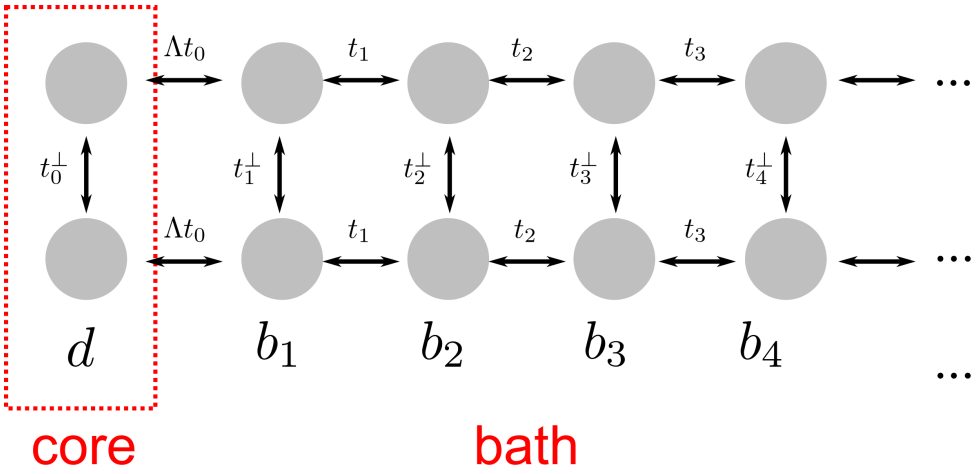

Figure D.1: Two-site Anderson model in the form of a semi-infinite two-chain ladder, corresponding to the Hamiltonian (D.1). The system is divided into two parts: The core consists of the correlated rung and the first L bath rungs (The figure shows the case $L = 0$) and the bath includes the remaining bath rungs.

with

$$\hat{Q}_\sigma^{\text{eff},\Lambda}(i\omega) = i\omega\mathbf{1} - \hat{t}_{L+1}^\perp - (\Lambda t_L)^2 \hat{\mathcal{G}}^{c,(1)}_{\text{core},\sigma}(i\omega, b_L, b_L) - t_{L+1}^2 \hat{g}_{b_{L+2},b_{L+3},\dots}(i\omega, b_{L+2}, b_{L+2}). \tag{D.3}$$

Here we used the abbreviation $\bar{b}_{L+1,\sigma} = \left(\bar{b}_{L+1,1,\sigma}, \bar{b}_{L+1,2,\sigma}, ..., \bar{b}_{L+1,N,\sigma}\right)$ for vectors in the b_{L+1}-rung subspace. Matrices in this space are denoted by a hat. $\mathcal{G}^{c,(n)}_{\text{core}}$ is the connected n-particle Green's function of the isolated core and $g_{b_{L+2},b_{L+3},\dots}$ the one-particle Green's function of the bath. $\hat{t}_{L+1}^\perp$ is the free hopping matrix on rung $L+1$.
As in the single impurity case one can derive fRG flow equations with respect to the parameter Λ, which are truncated by neglecting the flow of the three-particle vertex and all higher vertex functions. We are left with a coupled set of flow equations for the self-energy $\Sigma^\Lambda_{\text{eff}}$ and the two-particle vertex $\Gamma^\Lambda_{\text{eff}}$. The latter can be separated into two different spin channels like in Eq.(2.51) and we denote the direct part as V^Λ_{eff}. The flow equations are given by

$$\begin{aligned}\frac{d}{d\Lambda}\Sigma^\Lambda_{\text{eff}}(i\omega, i_1, i_{1'}) = &-\frac{1}{\beta}\sum_{i\omega'}\sum_{i_2,i_{2'}} S^\Lambda_{\text{eff}}(i\omega', i_{2'}, i_2) \\ &\times \left[2V^\Lambda_{\text{eff}}(i_1, i\omega; i_2, i\omega'|i_{1'}, i\omega; i_{2'}) \right. \\ &\left. - V^\Lambda_{\text{eff}}(i_1, i\omega; i_2, i\omega'|i_{2'}, i\omega'; i_{1'})\right],\end{aligned} \tag{D.4}$$

$$\begin{aligned}\frac{d}{d\Lambda}V^\Lambda_{\text{eff}}(i_1, i\omega_1; i_2, i\omega_2|i_{1'}, i\omega_{1'}; i_{2'}) = &\mathcal{T}^\Lambda_{\text{pp}}(i_1, i\omega_1; i_2, i\omega_2|i_{1'}, i\omega_{1'}; i_{2'}) \\ &+ \mathcal{T}^\Lambda_{\text{dph}}(i_1, i\omega_1; i_2, i\omega_2|i_{1'}, i\omega_{1'}; i_{2'}) \\ &+ \mathcal{T}^\Lambda_{\text{crph}}(i_1, i\omega_1; i_2, i\omega_2|i_{1'}, i\omega_{1'}; i_{2'})\end{aligned} \tag{D.5}$$

with

$$\begin{aligned}\mathcal{T}^{\Lambda}_{\mathrm{pp}}\left(i_1, i\omega_1; i_2, i\omega_2 | i_{1'}, i\omega_{1'}; i_{2'}\right) = \frac{1}{\beta}\sum_{i\omega_3}\sum_{\substack{i_3,i_4\\ i_{3'},i_{4'}}} & L^{\Lambda}\left(i\omega_3, i\omega_1 + i\omega_2 - i\omega_3, i_{3'}, i_3, i_{4'}, i_4\right) \\ & \times V^{\Lambda}_{\mathrm{eff}}\left(i_3, i\omega_3; i_4, i\omega_1 + i\omega_2 - i\omega_3 | i_{1'}, i\omega_{1'}; i_{2'}\right) \\ & \times V^{\Lambda}_{\mathrm{eff}}\left(i_1, i\omega_1; i_2, i\omega_2 | i_{3'}, i\omega_3; i_{4'}\right), \end{aligned} \tag{D.6}$$

$$\begin{aligned}\mathcal{T}^{\Lambda}_{\mathrm{dph}}\left(i_1, i\omega_1; i_2, i\omega_2 | i_{1'}, i\omega_{1'}; i_{2'}\right) = -\frac{1}{\beta}\sum_{i\omega_3}\sum_{\substack{i_3,i_4\\ i_{3'},i_{4'}}} & L^{\Lambda}\left(i\omega_3, i\omega_1 - i\omega_{1'} + i\omega_3, i_{3'}, i_3, i_{4'}, i_4\right) \\ & \times \big[2V^{\Lambda}_{\mathrm{eff}}\left(i_1, i\omega_1; i_3, i\omega_3 | i_{1'}, i\omega_{1'}; i_{4'}\right) \\ & \times V^{\Lambda}_{\mathrm{eff}}\left(i_4, i\omega_1 - i\omega_{1'} + i\omega_3; i_2, i\omega_2 | i_{3'}, i\omega_3; i_{2'}\right) \\ & - V^{\Lambda}_{\mathrm{eff}}\left(i_1, i\omega_1; i_3, i\omega_3 | i_{1'}, i\omega_{1'}; i_{4'}\right) \\ & \times V^{\Lambda}_{\mathrm{eff}}\left(i_2, i\omega_2; i_4, i\omega_1 - i\omega_{1'} + i\omega_3 | i_{3'}, i\omega_3; i_{2'}\right) \\ & - V^{\Lambda}_{\mathrm{eff}}\left(i_3, i\omega_3; i_1, i\omega_1 | i_{1'}, i\omega_{1'}; i_{4'}\right) \\ & \times V^{\Lambda}_{\mathrm{eff}}\left(i_4, i\omega_1 - i\omega_{1'} + i\omega_3; i_2, i\omega_2 | i_{3'}, i\omega_3; i_{2'}\right)\big], \end{aligned} \tag{D.7}$$

$$\begin{aligned}\mathcal{T}^{\Lambda}_{\mathrm{crph}}\left(i_1, i\omega_1; i_2, i\omega_2 | i_{1'}, i\omega_{1'}; i_{2'}\right) = \frac{1}{\beta}\sum_{i\omega_3}\sum_{\substack{i_3,i_4\\ i_{3'},i_{4'}}} & L^{\Lambda}\left(i\omega_3, i\omega_2 - i\omega_{1'} + i\omega_3, i_{3'}, i_3, i_{4'}, i_4\right) \\ & \times V^{\Lambda}_{\mathrm{eff}}\left(i_3, i\omega_3; i_2, i\omega_2 | i_{1'}, i\omega_{1'}; i_{4'}, i\omega_4\right) \\ & \times V^{\Lambda}_{\mathrm{eff}}\left(i_1, i\omega_1; i_4, i\omega_2 - i\omega_{1'} + i\omega_3 | i_{3'}, i\omega_3; i_{2'}\right) \end{aligned} \tag{D.8}$$

and the single-scale propagator

$$\hat{S}^{\Lambda}_{\mathrm{eff}}(i\omega) = \hat{\mathcal{G}}^{\Lambda}_{\mathrm{eff}}(i\omega)\frac{d}{d\Lambda}\left[\hat{Q}^{\mathrm{eff},\Lambda}(i\omega)\right]\hat{\mathcal{G}}^{\Lambda}_{\mathrm{eff}}(i\omega). \tag{D.9}$$

The function L^{Λ} is defined as

$$L^{\Lambda}\left(i\omega_1, i\omega_2, i_1, i_2, i_3, i_4\right) = \mathcal{G}^{\Lambda}_{\mathrm{eff}}\left(i\omega_1, i_1, i_2\right) S^{\Lambda}_{\mathrm{eff}}\left(i\omega_2, i_3, i_4\right) + S^{\Lambda}_{\mathrm{eff}}\left(i\omega_1, i_1, i_2\right) \mathcal{G}^{\Lambda}_{\mathrm{eff}}\left(i\omega_2, i_3, i_4\right) \tag{D.10}$$

with the Green's function

$$\left[\hat{\mathcal{G}}^{\Lambda}_{\mathrm{eff}}(i\omega)\right]^{-1} = \hat{Q}^{\mathrm{eff},\Lambda}(i\omega) - \hat{\Sigma}^{\Lambda}_{\mathrm{eff}}(i\omega). \tag{D.11}$$

In the flow equation for the vertex function (D.5) we use the Katanin-replacement [Kat04]

$$\hat{S}^{\Lambda}_{\mathrm{eff}} \to -\frac{d\hat{\mathcal{G}}^{\Lambda}_{\mathrm{eff}}}{d\Lambda} = \hat{S}^{\Lambda}_{\mathrm{eff}} - \hat{\mathcal{G}}^{\Lambda}_{\mathrm{eff}}\frac{d\hat{\Sigma}^{\Lambda}_{\mathrm{eff}}}{d\Lambda}. \tag{D.12}$$

The initial conditions for $\Lambda = 0$ are

$$\Sigma^{\Lambda=0}_{\mathrm{eff}}\left(i\omega, i_1, i_{1'}\right) = 0, \tag{D.13}$$

$$V^{\Lambda}_{\mathrm{eff}}\left(i_1, i\omega_1; i_2, i\omega_2 | i_{1'}, i\omega_{1'}; i_{2'}\right) = t_L^4 \mathcal{G}^{c,(2)}_{\mathrm{core}}\left(b_L, i_1, \uparrow, i\omega_1; b_L, i_2, \downarrow, i\omega_2 | b_L, i_{1'}, \uparrow, i\omega_{1'}; b_L, i_{2'}, \downarrow\right). \tag{D.14}$$

Bibliography

[AEKM08] S. Andergassen, T. Enss, C. Karrasch, and V. Meden. A gentle introduction to the functional renormalization group: The Kondo effect in quantum dots. pages 1–17, 2008.

[AFL83] N. Andrei, K. Furuya, and J. H. Lowenstein. Solution of the Kondo problem. *Rev. Mod. Phys.*, 55:331–402, Apr 1983.

[AM12] A. Avella and F. Mancini. *Strongly Correlated Systems: Theoretical Methods*. Springer Series in Solid-State Sciences. Springer, Berlin, 2012.

[AMS+10] S. Andergassen, V. Meden, H. Schoeller, Splettstoesser. J., and M. R. Wegewijs. Charge transport through single molecules, quantum dots and quantum wires. *Nanotechnology*, 21(27):272001, 2010.

[And61] P. W. Anderson. Localized magnetic states in metals. *Phys. Rev.*, 124(1):41–53, Oct 1961.

[And70] P. W. Anderson. A poor man's derivation of scaling laws for the Kondo problem. *Journal of Physics C: Solid State Physics*, 3(12):2436, 1970.

[And72] P. W. Anderson. More is different. *Science*, 177(4047):393–396, 1972.

[AS06] A. Altland and B. Simons. *Condensed Matter Field Theory*. Cambridge University press, 2006.

[ATMS09] F. Aryasetiawan, J. M. Tomczak, T. Miyake, and R. Sakuma. Downfolded self-energy of many-electron systems. *Phys. Rev. Lett.*, 102:176402, Apr 2009.

[Bax82] R.J. Baxter. *Exactly Solved Models in Statistical Mechanics*. Academic Press, 1982.

[BCP08] R. Bulla, T. A. Costi, and T. Pruschke. Numerical renormalization group method for quantum impurity systems. *Rev. Mod. Phys.*, 80:395–450, Apr 2008.

[BFCK09] L. Bartosch, H. Freire, J. J. R. Cardenas, and P. Kopietz. A functional renormalization group approach to the Anderson impurity model. *Journal of Physics: Condensed Matter*, 21(30):305602, 2009.

[BGM00] K. S. D. Beach, R. J. Gooding, and F. Marsiglio. Reliable padé analytical continuation method based on a high-accuracy symbolic computation algorithm. *Phys. Rev. B*, 61:5147–5157, Feb 2000.

[BHP98] R. Bulla, A.C. Hewson, and T. Pruschke. Numerical renormalization group calculations for the self-energy of the impurity Anderson model. *Journal of Physics: Condensed Matter*, 10(37):8365, 1998.

[BKH+07] K. Byczuk, M. Kollar, K. Held, Y.-F. Yang, I. A. Nekrasov, T. Pruschke, and D. Vollhardt. Kinks in the dispersion of strongly correlated electrons. *Nat. Phys.*, 3:1745–2473, 2007.

[Blu03] N. Blümer. *Metal-Insulator Transition and Optical Conductivity in High Dimensions*. Phd thesis, RWTH Aachen University, 2003.

[BR70] W. F. Brinkman and T. M. Rice. Application of Gutzwiller's variational method to the metal-insulator transition. *Phys. Rev. B*, 2:4302–4304, Nov 1970.

[Bul99] R. Bulla. Zero temperature metal-insulator transition in the infinite-dimensional Hubbard model. *Phys. Rev. Lett.*, 83:136–139, Jul 1999.

[CK94] M. Caffarel and W. Krauth. Exact diagonalization approach to correlated fermions in infinite dimensions: Mott transition and superconductivity. *Phys. Rev. Lett.*, 72:1545–1548, Mar 1994.

[dHdBvdB34] W.J. de Haas, J. de Boer, and G.J. van dën Berg. The electrical resistance of gold, copper and lead at low temperatures. *Physica*, 1(7-12):1115–1124, 1934.

[DLS78] F. J. Dyson, E. H. Lieb, and B. Simon. Phase transitions in quantum spin systems with isotropic and nonisotropic interactions. *Journal of Statistical Physics*, 18(4):335–383, 1978.

[Eco06] E. N. Economou. *Greens Functions in Quantum Physics*. Springer, 2006.

[FMNR01] W. M. C. Foulkes, L. Mitas, R. J. Needs, and G. Rajagopal. Quantum Monte Carlo simulations of solids. *Rev. Mod. Phys.*, 73:33–83, Jan 2001.

[Geb97] F. Gebhard. *The Mott Metal-Insulator Transition*. Springer, 1997.

[GGSM+97] D. Goldhaber-Gordon, H. Shtrikman, D. Mahalu, D. Abusch-Magder, U. Meirav, and M.A. Kastner. Kondo effect in a single-electron transistor. *Nature*, 391:156–159, 1997.

[GK92] A. Georges and G. Kotliar. Hubbard model in infinite dimensions. *Phys. Rev. B*, 45:6479–6483, Mar 1992.

[GKKR96] A. Georges, G. Kotliar, W. Krauth, and M. J. Rozenberg. Dynamical mean-field theory of strongly correlated fermion systems and the limit of infinite dimensions. *Rev. Mod. Phys.*, 68:13–125, Jan 1996.

[GML+11] E. Gull, A. J. Millis, A. I. Lichtenstein, A. N. Rubtsov, M. Troyer, and P. Werner. Continuous-time Monte carlo methods for quantum impurity models. *Rev. Mod. Phys.*, 83:349–404, May 2011.

[GPM07] R. Gezzi, T. Pruschke, and V. Meden. Functional renormalization group for nonequilibrium quantum many-body problems. *Phys. Rev. B*, 75:045324, Jan 2007.

[GS12] K. Giering and M. Salmhofer. Self-energy flows in the two-dimensional repulsive Hubbard model. *Phys. Rev. B*, 86:245122, Dec 2012.

[Gut63] M. C. Gutzwiller. Effect of correlation on the ferromagnetism of transition metals. *Phys. Rev. Lett.*, 10:159–162, Mar 1963.

[Gut65] M. C. Gutzwiller. Correlation of electrons in a narrow s band. *Phys. Rev.*, 137:A1726–A1735, Mar 1965.

[GV93] C. Gros and R. Valentí. Cluster expansion for the self-energy: A simple many-body method for interpreting the photoemission spectra of correlated Fermi systems. *Phys. Rev. B*, 48:418–425, Jul 1993.

[Hel07] K. Held. Electronic structure calculations using dynamical mean field theory. *Advances in Physics*, 56(6):829–926, 2007.

[Hew93] A.C. Hewson. *The Kondo Problem to Heavy Fermions*. Cambridge University Press, 1993.

[HJB+09] H. Hafermann, C. Jung, S. Brener, M. I. Katsnelson, A. N. Rubtsov, and A. I. Lichtenstein. Superperturbation solver for quantum impurity models. *EPL (Europhysics letter)*, 85(2):27007, 2009.

[HKT08] K. Held, A. A. Katanin, and A. Toschi. Dynamical Vertex Approximation. *Progress of Theoretical Physics Supplement*, 176:117–133, 2008.

[HMPS04] R. Hedden, V. Meden, T. Pruschke, and K. Schönhammer. A functional renormalization group approach to zero-dimensional interacting systems. *Journal of Physics: Condensed Matter*, 16(29):5279, 2004.

[Hoh67] P. C. Hohenberg. Existence of long-range order in one and two dimensions. *Phys. Rev.*, 158:383–386, Jun 1967.

[HPT13] K. Held, R. Peters, and A. Toschi. Poor man's understanding of kinks originating from strong electronic correlations. *Phys. Rev. Lett.*, 110:246402, Jun 2013.

[HRAE04] C. Honerkamp, D. Rohe, S. Andergassen, and T. Enss. Interaction flow method for many-fermion systems. *Phys. Rev. B*, 70:235115, Dec 2004.

[HS09] C. Husemann and M. Salmhofer. Efficient parametrization of the vertex function, Ω scheme, and the t, t' Hubbard model at van Hove filling. *Phys. Rev. B*, 79:195125, May 2009.

[Hub63] J. Hubbard. Electron correlations in narrow energy bands. *Proceedings of the Royal Society of London. Series A. Mathematical and Physical Sciences*, 276(1365):238–257, 1963.

[Hub64] J. Hubbard. Electron correlations in narrow energy bands. iii. An improved solution. *Proceedings of the Royal Society of London. Series A. Mathematical and Physical Sciences*, 281(1386):401–419, 1964.

[IRB+10] A. Isidori, D. Roosen, L. Bartosch, W. Hofstetter, and P. Kopietz. Spectral function of the Anderson impurity model at finite temperatures. *Phys. Rev. B*, 81:235120, Jun 2010.

[Jar92] M. Jarrell. Hubbard model in infinite dimensions: A quantum Monte Carlo study. *Phys. Rev. Lett.*, 69:168–171, Jul 1992.

[JMS07] S. G. Jakobs, V. Meden, and H. Schoeller. Nonequilibrium functional renormalization group for interacting quantum systems. *Phys. Rev. Lett.*, 99:150603, Oct 2007.

[Joe10] D. Joerg. On integrating out a correlated quantum dot. Diploma thesis, University of Heidelberg, Germany, 2010.

[JPS10] S. G. Jakobs, M. Pletyukhov, and H. Schoeller. Nonequilibrium functional renormalization group with frequency-dependent vertex function: A study of the single-impurity Anderson model. *Phys. Rev. B*, 81:195109, May 2010.

[Kan63] J. Kanamori. Electron correlation and ferromagnetism of transition metals. *Progress of Theoretical Physics*, 30(3):275–289, 1963.

[Kat04] A. A. Katanin. Fulfillment of Ward identities in the functional renormalization group approach. *Phys. Rev. B*, 70:115109, Sep 2004.

[KBC+10] P. Kopietz, L. Bartosch, L. Costa, A. Isidori, and A. Ferraz. Ward identities for the Anderson impurity model: derivation via functional methods and the exact renormalization group. *Journal of Physics A: Mathematical and Theoretical*, 43(38):385004, 2010.

[KBS10] P. Kopietz, L. Bartosch, and F. Schütz. *Introduction to the Functional Renormalization Group (Lecture Notes in Physics)*. Springer, 2010.

[KEM06] C. Karrasch, T. Enss, and V. Meden. Functional renormalization group approach to transport through correlated quantum dots. *Phys. Rev. B*, 73:235337, Jun 2006.

[KH13] Michael Kinza and Carsten Honerkamp. Two-particle correlations in a functional renormalization group scheme using a dynamical mean-field theory approach. *Phys. Rev. B*, 88:195136, Nov 2013.

[KHP+08] C. Karrasch, R. Hedden, R. Peters, T. Pruschke, K. Schönhammer, and V. Meden. A finite-frequency functional renormalization group approach to the single impurity Anderson model. *Journal of Physics: Condensed Matter*, 20(34):345205, 2008.

[KLS88] T. Kennedy, E. H. Lieb, and B. S. Shastry. Existence of Néel order in some spin-1/2 Heisenberg antiferromagnets. *Journal of Statistical Physics*, 53(5-6):1019–1030, 1988.

[KMS10] C. Karrasch, V. Meden, and K. Schönhammer. Finite-temperature linear conductance from the Matsubara Green's function without analytic continuation to the real axis. *Phys. Rev. B*, 82:125114, Sep 2010.

[KmWW80a] H. R. Krishna-murthy, J. W. Wilkins, and K. G. Wilson. Renormalization-group approach to the Anderson model of dilute magnetic alloys. i. Static properties for the symmetric case. *Phys. Rev. B*, 21:1003–1043, Feb 1980.

[KmWW80b] H. R. Krishna-murthy, J. W. Wilkins, and K. G. Wilson. Renormalization-group approach to the Anderson model of dilute magnetic alloys. ii. Static properties for the asymmetric case. *Phys. Rev. B*, 21:1044–1083, Feb 1980.

[KOBH13] M. Kinza, J. Ortloff, J. Bauer, and C. Honerkamp. Alternative functional renormalization group approach to the single impurity Anderson model. *Phys. Rev. B*, 87:035111, Jan 2013.

[KOH10] M. Kinza, J. Ortloff, and C. Honerkamp. Effective low-energy Hamiltonians for interacting nanostructures. *Phys. Rev. B*, 82:155430, Oct 2010.

[Kon64] J. Kondo. Resistance minimum in dilute magnetic alloys. *Progress of Theoretical Physics*, 32(1):37–49, 1964.

[KPBM10] C. Karrasch, M. Pletyukhov, L. Borda, and V. Meden. Functional renormalization group study of the interacting resonant level model in and out of equilibrium. *Phys. Rev. B*, 81:125122, Mar 2010.

[KSH+06] G. Kotliar, S. Y. Savrasov, K. Haule, V. S. Oudovenko, O. Parcollet, and C. A. Marianetti. Electronic structure calculations with dynamical mean-field theory. *Rev. Mod. Phys.*, 78:865–951, Aug 2006.

[KSPB01] G. Kotliar, S. Y. Savrasov, G. Pálsson, and G. Biroli. Cellular dynamical mean field approach to strongly correlated systems. *Phys. Rev. Lett.*, 87:186401, Oct 2001.

[KV04] G. Kotliar and D. Vollhardt. Strongly correlated materials: Insights from dynamical mean-field theory. *Physics Today*, 57(3):53–59, 2004.

[Lan50] C. Lanczos. An iteration method for the solution of the eigenvalue problem of linear differential and integral operators. *Journal of Research of the National Bureau of Standards*, 45:255–282, 1950.

[Lan66] D. C. Langreth. Friedel sum rule for Anderson's model of localized impurity states. *Phys. Rev.*, 150:516–518, Oct 1966.

[Lan98] E. Lange. Renormalized versus unrenormalized perturbation-theoretical approaches to the Mott transition. *Modern Physics Letters B*, 12(22):915–919, 1998.

[LHL+12] M. Liu, L. W. Harriger, H. Luo, M. Wang, R. A. Ewings, T. Guidi, H. Park, K. Haule, G. Kotliar, S. M. Hayden, and P. Dai. Nature of magnetic excitations in superconducting $\mathrm{bafe}_{1.9}\mathrm{ni}_{0.1}\mathrm{as}_2$. *Nat. Phys.*, 8:376–381, 2012.

[LI12] A. Liebsch and H. Ishida. Temperature and bath size in exact diagonalization dynamical mean field theory. *Journal of Physics: Condensed Matter*, 24(5):053201, 2012.

[LK00] A. I. Lichtenstein and M. I. Katsnelson. Antiferromagnetism and d-wave superconductivity in cuprates: A cluster dynamical mean-field theory. *Phys. Rev. B*, 62:R9283–R9286, Oct 2000.

[LNW06] P. A. Lee, N. Nagaosa, and X. Wen. Doping a Mott insulator: Physics of high-temperature superconductivity. *Rev. Mod. Phys.*, 78:17–85, Jan 2006.

[Lui12] D. J. Luitz. *Numerical methods and applications in many fermion systems.* Phd thesis, University of Würzburg, Am Hubland, 97074 Würzburg, 2012.

[LW68] E. H. Lieb and F. Y. Wu. Absence of Mott transition in an exact solution of the short-range, one-band Model in one dimension. *Phys. Rev. Lett.*, 20:1445–1448, Jun 1968.

[Med06] V. Meden. lecture notes on the functional renormalization group. 2006.

[Mes79] A. Messiah. *Quantenmechanik, Band 2.* de Gruyter, 1979.

[MH89a] E. Müller-Hartmann. Correlated fermions on a lattice in high dimensions. *Zeitschrift für Physik B Condensed Matter*, 74(4):507–512, 1989.

[MH89b] E. Müller-Hartmann. The Hubbard model at high dimensions: some exact results and weak coupling theory. *Zeitschrift für Physik B Condensed Matter*, 76(2):211–217, 1989.

[MJPH05] T. Maier, M. Jarrell, T. Pruschke, and M. H. Hettler. Quantum cluster theories. *Rev. Mod. Phys.*, 77:1027–1080, Oct 2005.

[Mot68] N. F. Mott. Metal-Insulator transition. *Rev. Mod. Phys.*, 40:677–683, Oct 1968.

[MSH+12] W. Metzner, M. Salmhofer, C. Honerkamp, V. Meden, and K. Schönhammer. Functional renormalization group approach to correlated fermion systems. *Rev. Mod. Phys.*, 84:299–352, Mar 2012.

[MV89] W. Metzner and D. Vollhardt. Correlated lattice fermions in d=∞ dimensions. *Phys. Rev. Lett.*, 62:324–327, Jan 1989.

[MW66] N. D. Mermin and H. Wagner. Absence of Ferromagnetism or Antiferromagnetism in one- or two-dimensional isotropic Heisenberg models. *Phys. Rev. Lett.*, 17:1133–1136, Nov 1966.

[MW92] Y. Meir and N. S. Wingreen. Landauer formula for the current through an interacting electron region. *Phys. Rev. Lett.*, 68:2512–2515, Apr 1992.

[NO88] J. W. Negele and H. Orland. *Quantum many-particle systems*. Addison-Wesley, 1988.

[Noz74] P. Noziéres. A 'fermi-liquid' description of the Kondo problem at low temperatures. *Journal of Low Temperature Physics*, 17(1-2):31–42, 1974.

[Ort] J. Ortloff. Phd thesis (unpublished), University of Würzburg.

[PHK11] H. Park, K. Haule, and G. Kotliar. Magnetic excitation spectra in $bafe_2as_2$: A two-particle approach within a combination of the density functional theory and the dynamical mean-field theory method. *Phys. Rev. Lett.*, 107:137007, Sep 2011.

[PJF95] T. Pruschke, M. Jarrell, and J.K. Freericks. Anomalous normal-state properties of high-t c superconductors: intrinsic properties of strongly correlated electron systems? *Advances in Physics*, 44(2):187–210, 1995.

[Pol84] J. Polchinski. Renormalization and effective lagrangians. *Nuclear Physics B*, 231(2):269 – 295, 1984.

[Pot01] M. Potthoff. Two-site dynamical mean-field theory. *Phys. Rev. B*, 64:165114, Oct 2001.

[RKL08] A. N. Rubtsov, M. I. Katsnelson, and A. I. Lichtenstein. Dual fermion approach to nonlocal correlations in the Hubbard model. *Phys. Rev. B*, 77:033101, Jan 2008.

[RKLG09] A. N. Rubtsov, M. I. Katsnelson, A. I. Lichtenstein, and A. Georges. Dual fermion approach to the two-dimensional Hubbard model: Antiferromagnetic fluctuations and Fermi arcs. *Phys. Rev. B*, 79:045133, Jan 2009.

[RmcD11a] A. Rançon and N. Dupuis. Nonperturbative renormalization group approach to strongly correlated lattice bosons. *Phys. Rev. B*, 84:174513, Nov 2011.

[RmcD11b] A. Rançon and N. Dupuis. Nonperturbative renormalization group approach to the Bose-Hubbard model. *Phys. Rev. B*, 83:172501, May 2011.

[RTH+13] G. Rohringer, A. Toschi, H. Hafermann, K. Held, V. I. Anisimov, and A. A. Katanin. One-particle irreducible functional approach: A route to diagrammatic extensions of the dynamical mean-field theory. *Phys. Rev. B*, 88:115112, Sep 2013.

[RTKH11] G. Rohringer, A. Toschi, A. Katanin, and K. Held. Critical properties of the half-filled Hubbard Model in three dimensions. *Phys. Rev. Lett.*, 107:256402, Dec 2011.

[RU09] C. Raas and G. S. Uhrig. Generic susceptibilities of the half-filled Hubbard model in infinite dimensions. *Phys. Rev. B*, 79:115136, Mar 2009.

[RVT12] G. Rohringer, A. Valli, and A. Toschi. Local electronic correlation at the two-particle level. *Phys. Rev. B*, 86:125114, Sep 2012.

[RZK92] M. J. Rozenberg, X. Y. Zhang, and G. Kotliar. Mott-Hubbard transition in infinite dimensions. *Phys. Rev. Lett.*, 69:1236–1239, Aug 1992.

[Saa11] K. Sääskilahti. Functional renormalization group study of quantum spin chains. Masters thesis, Aalto University, 2011.

[Sch05] U. Schollwöck. The density-matrix renormalization group. *Rev. Mod. Phys.*, 77:259–315, Apr 2005.

[SH01] M. Salmhofer and C. Honerkamp. Fermionic Renormalization Group Flows. *Progress of Theoretical Physics*, 105(1):1–35, 2001.

[SIK13] S. Streib, A. Isidori, and P. Kopietz. Solution of the Anderson impurity model via the functional renormalization group. *Phys. Rev. B*, 87:201107, May 2013.

[SJMD09] C. Slezak, M. Jarrell, Th. Maier, and J. Deisz. Multi-scale extensions to quantum cluster methods for strongly correlated electron systems. *Journal of Physics: Condensed Matter*, 21(43):435604, 2009.

[SK04] T. D. Stanescu and G. Kotliar. Strong coupling theory for interacting lattice models. *Phys. Rev. B*, 70:205112, Nov 2004.

[SPP02] D. Sénéchal, D. Perez, and D. Plouffe. Cluster perturbation theory for Hubbard models. *Phys. Rev. B*, 66:075129, Aug 2002.

[SRG+13] T. Schäfer, G. Rohringer, O. Gunnarsson, S. Ciuchi, G. Sangiovanni, and A. Toschi. Divergent precursors of the Mott-Hubbard transition at the two-particle level. *Phys. Rev. Lett.*, 110:246405, Jun 2013.

[Ste84] G. R. Stewart. Heavy-fermion systems. *Rev. Mod. Phys.*, 56:755–787, Oct 1984.

[SW66] J. R. Schrieffer and P. A. Wolff. Relation between the Anderson and Kondo Hamiltonians. *Phys. Rev.*, 149:491–492, Sep 1966.

[TAB+13] C. Taranto, S. Andergassen, J. Bauer, K. Held, A. Katanin, W. Metzner, G. Rohringer, and A. Toschi. From infinite to two dimensions through the functional renormalization group. *ArXiv e-prints*, 2013.

[TAH+12] A. Toschi, R. Arita, P. Hansmann, G. Sangiovanni, and K. Held. Quantum dynamical screening of the local magnetic moment in fe-based superconductors. *Phys. Rev. B*, 86:064411, Aug 2012.

[TCCH09] A. Toschi, M. Capone, C. Castellani, and K. Held. Kinks in the electronic specific heat. *Phys. Rev. Lett.*, 102:076402, Feb 2009.

[TKH07] A. Toschi, A. A. Katanin, and K. Held. Dynamical vertex approximation: A step beyond dynamical mean-field theory. *Phys. Rev. B*, 75:045118, Jan 2007.

[UH12] S. Uebelacker and C. Honerkamp. Self-energy feedback and frequency-dependent interactions in the functional renormalization group flow for the two-dimensional hubbard model. *Phys. Rev. B*, 86:235140, Dec 2012.

[VS77] H.J. Vidberg and J.W. Serene. Solving the Eliashberg equations by means of N-point Padé approximants. *Journal of Low Temperature Physics*, 29(3-4):179–192, 1977.

[Wet93] C. Wetterich. Exact evolution equation for the effective potential. *Physics Letters B*, 301(1):90–94, 1993.

[Wil71] K. G. Wilson. Renormalization group and critical phenomena. ii. Phase-space cell analysis of critical behavior. *Phys. Rev. B*, 4:3184–3205, Nov 1971.

[Wil75] K. G. Wilson. The renormalization group: Critical phenomena and the kondo problem. *Rev. Mod. Phys.*, 47:773–840, Oct 1975.

[WK74] K. G. Wilson and J. Kogut. The renormalization group and the ϵ expansion. *Physics Reports*, 12(2):75 – 199, 1974.

[WLXW13] W. Wang, Z. Li, Y. Xiang, and Q. Wang. Competing electronic orders on kagome lattices at van hove filling. *Phys. Rev. B*, 87:115135, Mar 2013.

[WM10] P. Werner and A. J. Millis. Dynamical screening in correlated electron materials. *Phys. Rev. Lett.*, 104:146401, Apr 2010.

[XWWL12] Y. Xiang, W. Wang, Q. Wang, and D. Lee. Topological superconducting phase in the vicinity of ferromagnetic phases. *Phys. Rev. B*, 86:024523, Jul 2012.